Continuously Variable Posture Selection in Robotic Milling for Increased Chatter Stability

by Bora GÖNÜL

Submitted to the Graduate School of Engineering and Natural Sciences

In partial fulfillment

of the requirements for the degree of

Master of Engineering

Sabancı University August 2020

Continuously Variable Posture Selection in Robotic Milling for Increased Chatter Stability

APPROVED BY:

Asst. Prof. Dr. Lütfi Taner TUNÇ .....
(Thesis Supervisor)

Prof. Dr. Erhan BUDAK .....

Asst. Prof. Dr. Orkun ÖZŞAHİN .....

DATE OF APPROVAL: 24/08/2020

©BORA GÖNÜL 2020

All rights reserved

Dedicated to my beloved grandmother...

ABSTRACT

Continuously Variable Posture Selection in Robotic Milling for Increased Chatter Stability

Bora Gönül

Manufacturing Engineering MSc. Thesis, 2020

Supervisor: Asst. Prof. Lütfi Taner Tunç

Keywords: Robot Dynamics, Milling Dynamics, Stable Cutting Conditions, Chatter Vibrations, Robotic Milling

The demand for the usage of industrial robots for milling applications has surged owing to their superiority in terms of the large working envelope, reconfigurability, and low capital investment. Albeit such advantages, utilization of industrial robots for milling applications is yet to be a wonderland, where there are major challenges such as low tool path contouring accuracy, less static and dynamic rigidity. The former may be bearable for milling operations requiring less accuracy, such as roughing cycles. However, lowered dynamic rigidity causes decreased chatter stability, which is a roadblock towards effective robotic milling applications as a result of high vibration marks, bad surface quality, tool breakage and damage to the entire system. The position and orientation of the robots have a significant impact on milling stability. Therefore, identification of improved stable conditions is important to achieve increased productivity and process quality. In this thesis, dynamic modeling of the robots is studied to predict the variation in the robot dynamics with robot posture. Simulation results are compared to experimental modal analysis results and possible error sources are discussed. Milling dynamics and stability analysis are further extended to propose an alternative approach to increase chatter stability limits by benefiting the redundant axis of the 6-axis industrial robot. Different configurations of the robot based on the utilization of the redundant axis result in different stability limits by maintaining the same position of the tool. Preferable configuration sequences are generated for the improved cutting conditions through stability simulations based on measured frequency response functions of the tooltip. A proper robot programming scheme is also proposed in order to enable industrial application of the proposed methodology. Furthermore, the advantages of the proposed approach are discussed in accordance with the simulation results.

ÖZET

Artırılmış Tırlama Titreşimleri Kararlılığı için Robotik Frezelemede Sürekli Değişken Duruş Seçimi

Bora Gönül

Üretim Mühendisliği, Yüksek Lisans Tezi, Ağustos 2020

Tez Danışmanı: Dr. Lütfi Taner Tunç

Anahtar Kelimeler: Robot Dinamiği, Frezeleme Dinamiği, Kararlı Kesme Koşulları, Tırlama Titreşimleri, Robotik Frezeleme

Frezeleme uygulamaları için endüstriyel robotların kullanımına olan talep, geniş çalışma alanı, yeniden yapılandırılabilirlik ve düşük sermaye yatırımı açısından üstünlükleri nedeniyle artmıştır. Bu tür avantajlara rağmen, frezeleme uygulamaları için endüstriyel robotların kullanımı, düşük takım yolu hassasiyeti, daha az statik ve dinamik rijitlik gibi büyük zorlukların olduğu bir harikalar diyarı değildir. İlki, kaba işleme döngüleri gibi daha az doğruluk gerektiren frezeleme işlemleri için uygun olabilir. Bununla birlikte, düşük dinamik rijitlik, yüksek titreşim işaretleri, kötü yüzey kalitesi, takım kırılması ve tüm sisteme verilen hasarın bir sonucu olarak etkili robotik frezeleme uygulamalarının önünde bir engel olan düşük tırlama stabilitesine neden olur. Robotların konumu ve duruşu frezeleme stabilitesi üzerinde önemli bir etkiye sahiptir. Bu nedenle, geliştirilmiş kararlı kesme koşullarının belirlenmesi, artan üretkenlik ve işlem kalitesi elde etmek için önemlidir. Bu tezde, robot duruşu ile robot dinamiğindeki değişimi tahmin etmek için robotların dinamik modellenmesi incelenmiştir. Simülasyon sonuçları deneysel modal analiz sonuçlarıyla karşılaştırılır ve olası hata kaynakları tartışılmıştır. Frezeleme dinamikleri ve stabilite analizi, 6 eksenli endüstriyel robotun yedek ekseninden yararlanarak tırlama stabilite sınırlarını artırmak için alternatif bir yaklaşım önermek üzere daha da genişletilmiştir. Yedek eksenin kullanımına dayalı farklı robot konfigürasyonları, robotun aynı pozisyonunu koruyarak farklı stabilite sınırlarıyla sonuçlanır. Takım ucu ipucunun ölçülen frekans yanıtı işlevlerine dayalı olarak stabilite simülasyonları aracılığıyla iyileştirilmiş kesme koşulları için tercih edilen konfigürasyon dizileri oluşturulur. Önerilen metodolojinin endüstriyel uygulamasını mümkün kılmak için uygun bir robot programlama şeması da önerilmiştir. Ayrıca, önerilen yaklaşımın avantajları simülasyon sonuçlarına göre tartışılmıştır.

ACKNOWLEDGEMENTS

In the first place, I would like to express my deepest appreciation to my thesis advisor, Assistant Prof. Dr. Lütfi Taner Tunç, for his patience, motivation, enthusiasm, and immense knowledge. I could not have imagined having a better advisor and mentor for my master study.

I would like to express my sincere gratitude to my committee member Professor Dr. Erhan Budak, for his motivational support, his precious comments and guiding attitude.

I would like to thank my committee member, Assistant Prof. Dr. Orkun Özşahin for his encouragements and valuable comments.

I wish to express my deepest gratitude to Ömer Altıntaş. I am profoundly grateful for his precious help and consultancy for my experimental work.

I would like to extend my sincere thanks to my colleagues and the robotic manufacturing team of KTMM for their support and time. Special thanks to my dear friends Ömer Faruk Sapmaz, Qasim Ali, Fatih Uzun, Esra Yüksel, Muhammed Hasan Arıkan, Fatih Eroğlu for all the enjoyable times we shared together. Finally, I must express my very profound gratitude to my parents Gül Pembe Gönül and Nedim Gönül for continuous encouragement throughout my life. This accomplishment would not have been possible without them. Thank you

TABLE OF CONTENTS

LIST OF FIGURES

LIST OF TABLES

LIST OF SYMBOLS AND ABBREVIATIONS

CNC : Computer numerical control

DOF : Degree of Freedom

TCP : Tool Center Point

FRF : Frequency response function

Gxx : FRF in X direction as a principal direction

Gyy : FRF in Y direction as a principal direction

Gf : FRF in feed direction

Gcf : FRF in cross-feed direction

a_{lim} : Stability limit

K_t : Tangential cutting force coefficient

Λ : Eigenvalue

Λ_R : Real part of the eigenvalue

N : Number of cutting teeth

MRR : Material Removal Rate

θ_i : Joint Angle (D-H parameter)

d_i : Link Offset (D-H parameter)

α_i : Link Twist (D-H parameter)

$C\theta_i$: Cosinus of the Joint Angle (D-H parameter)

$S\theta_i$: Sinus of the Joint Angle (D-H parameter)

β : Roll angle

α : Pitch angle

γ : Yaw angle

RNE : Recursive Newton Euler formulation

A_i - T_i : Homogeneous Transformation Matrix in the basis of link frames

ω : Angular velocity

$\dot{\omega}$: Angular acceleration

v : Linear velocity

$\dot{v}$: Linear acceleration

$\dot{v}_{com}$: Linear acceleration of the center of mass

r : Position vector for a point on the link

$r_{com_i}^{\ i}$: Position vector for center of mass w.r.t. link frame

R_i^{i-1} : Rotational part of the backward homogeneous transformation

R_{i-1}^{i} : Rotational part of the forward homogeneous transformation

g : Gravitational acceleration vector

F_{com} : Force induced by linear acceleration of the center of mass

$F_{i\,i-1}^{\ i-1}$: Inter-link forces

$N_{i\,i-1}^{\ i-1}$: Inter-link moments

N_{com} : Moment induced by inertia around center of mass

τ_i : Induced torque on joint i

$\mathcal{L}$: Lagrangian function

K : Kinetic energy of the system

U : Potential energy of the system

V_{comi} : Linear and angular velocity of the center of mass – Lagrangian Approach

I_i : Inertia matrix for link

J_i : Jacobian matrix for the links

J_{vi} : Sub-jacobian matrix related to partial change of the linear velocity of the links

$J_{\omega i}$: Sub-jacobian matrix related to partial change of angular velocity of the links

p_{comi} : Center of mass coordinates w.r.t. fixed base frame

M_{ij} : Mass matrix

V_i : Velocity coupling matrix - coriolis and centrifugal coefficients

G_i : Gravitational effect matrix

q_j : Joint variable (Joint angle)

$\dot{q}_j$: Joint variable (Joint velocity)

$\ddot{q}_j$: Joint variable (Joint acceleration)

J_i : Pseudo Inertia matrix – Lagrange -Euler based implementation

D_{ik} : Acceleration related terms in a matrix form for

H_i : Coriolis and centrifugal coefficients in a matrix form

c_i : Gravitational terms

CHAPTER 1: Introduction

1.1 Background of the study

Industrial robots have been used for repetitive monotonous industrial applications such as welding, painting, deburring, material handling, paper roll finishing, riveting as shown in Figure 1-1(a)-(b)-(c)-(d)-(e)-(f), respectively.

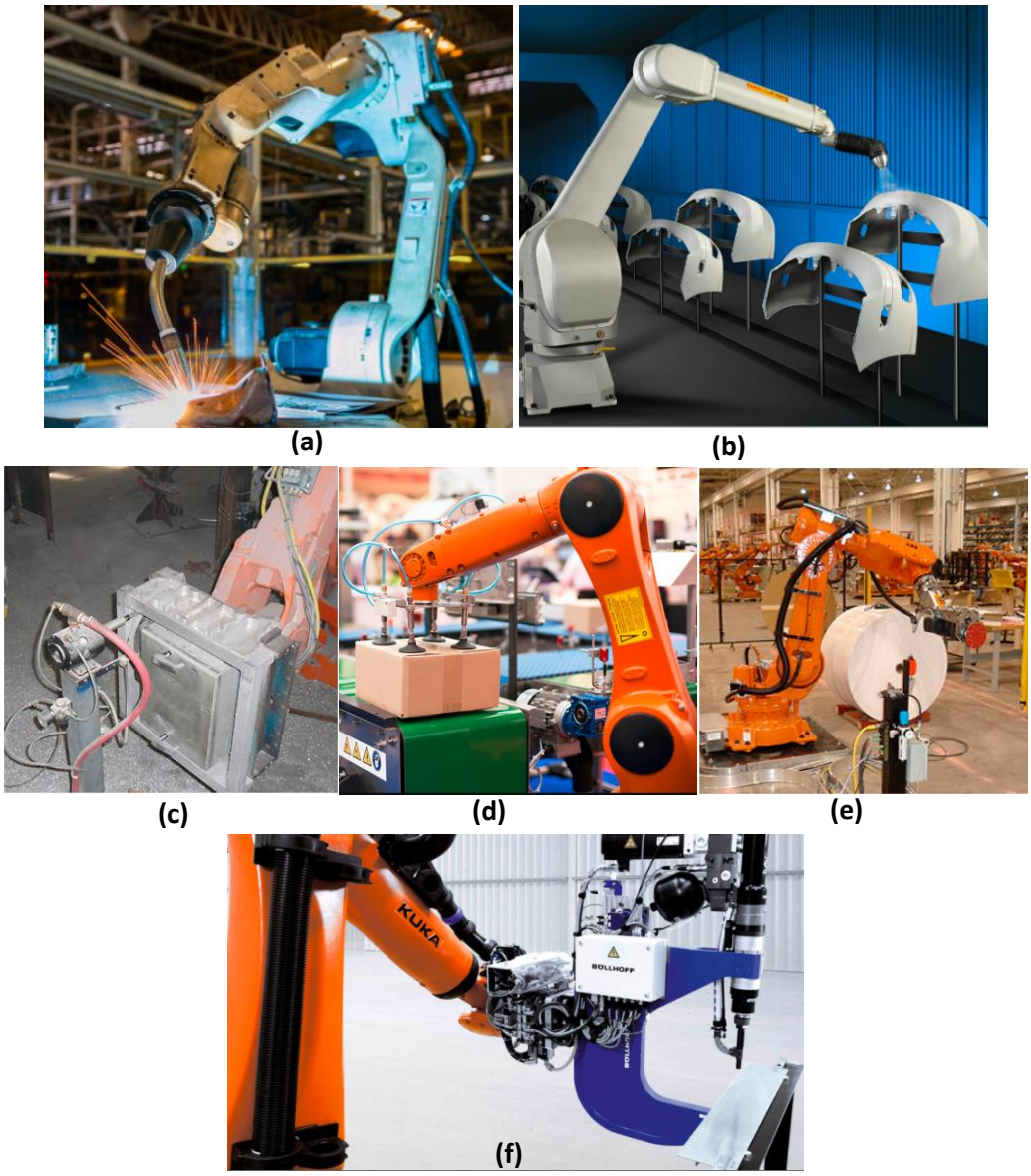

Figure 1-1:(a) welding robot,(b) painting robot,(c) deburring robot,(d) material handling robot,(e) paper roll finishing robot, (f) self-pierce riveting robot[57][58][59]

Monotonous tasks do not generate dynamic forces as in milling operation. Therefore, motion resistance and motion tendency to deviation are relatively low. Thus, stiffness and dynamic properties of the industrial robots have not been taking into account. However, the industry's interest in low-cost and reconfigurable production infrastructures has played an important role in robotic manufacturing due to significant superiorities that can be categorized as working envelope to footprint ratio, low capital investment, and re-programmability with respect to CNC machine tools. On the contrary, industrial robots have certain weaknesses that include low positioning accuracy, vibrations due to lack of stiffness which is stated as roughly 50 times less rigid compared to CNC machines, lack of reliable programming tool, and the flaws of articulated robots such as repeatability error that depends on reach distance. Recent research on robotic machining can be categorized into rapid prototyping, vibration/chattering analysis, path planning, and automatic robot programming areas. Generating various machining strategies such as special cut patterns and dual robot machining are emphasized to improve robot machining efficiency and accuracy, respectively. Developing an available rigidity map within a robot's working envelope is suggested to improve machining quality. Next, an optimized robot machining system configuration to obtain the best machining results without restricting the current industrial robot configurations is suggested. Additionally, various approaches proposed such as scaling down the robot arm to cope with the accuracy problems such as the error in the magnifying effect of the arm design and the low arm stiffness. Finally, a lack of research efforts about the development of an automatic machining line that includes isolated robot applications such as machining, deburring, grinding, or polishing are highlighted. [1][2][3][4]

Schneider et al.[5] analyzed the sources of errors in robotic machining such as environment-dependent errors, robot dependent errors, system errors, and process dependent errors, and categorizes them based on their amplitude and frequency. The authors indicated that machining using industrial robots is currently limited to applications with low geometrical accuracies and soft materials. The authors presented a modular approach and conducted experiments for error compensation to improve the accuracy of industrial robots in machining operations. The authors conducted machining experiments to analyze the effect of errors using a KR125 from KUKA. They found that the dominant frequencies in robot machining only depend on the mechanical properties of the robot. Next, the authors used the COMET approach that emphasizes a novel

modular and configurable error platform based on two compensation approaches: offline, predictive calculation of the robot positioning errors, and online, real-time measurement of the real robot TCP position. Their findings indicated that general cell setup and the selecting machining strategy significantly influence both geometric accuracy and surface quality. Furthermore, their position and frequency analysis identified the stiffest configuration of the robot and showed that compensation of compliance and backlash as the most effective.

He et al.[6] addressed the challenges in designing control system for industrial robots used in the machining process, particularly, fixed-gain controllers' issues regarding the stability and consistency in system performance, and complexity of robot controller due to the changes in the nonlinear relationship. To address the aforementioned problems, they proposed a novel adaptive PI control algorithm that uses exact linearization scheme to the nonlinear machining process. The results showed that self-tuning PI control is effective in force regulation during the robotic machining process. Moreover, the control performance and system stability are maintained during the machining process, though the cutting conditions have changed continuously. Vulliez et al.[7] addressed the problems in using conventional kinematic methods for feed rate for trajectory planning process in multi-axis machining. In multi-axis high-speed machining the feed rate is usually evaluated by a kinematic method as the maximum feed rate respecting the joint velocity, acceleration, and jerk limits. The authors proposed a new and efficient dynamic approach of the feed rate interpolation for trajectory planning process to address the problems of using conventional kinematic methods for feed rate. The model integrates the inertial, centrifugal and coriolis couplings, the gravity effect, and the friction forces, which are dynamic effects not included in the usual kinematic constraints (The dynamic effects have a strong influence on the feed rate calculation). The authors used a simulation approach to validate the model and compared the results of the simulation on two test paths and the feed rate profiles obtained by the usual kinematic method. The results indicated the efficiency of the proposed approach. Different types of methods are used for enabling and utilizing the industrial robots for machining applications and some of the relevant research activities are given. However, most of the scholars agreed on certain disadvantages especially relatively less stiff structure and varying dynamic parameters induce chatter vibrations which is one of the major constraints to the broad utilization of

industrial robots to machining applications, and detailed literature review is given in the next section.

1.2 Literature Review

Chatter is one of the major constraints in milling, leading to low productivity and quality. Thus, it remained a topic of interest for more than 50 years[8]. Chatter vibrations in robotic milling systems were first studied by Oki et al.[9]and Pan et al[10]. Findings indicated that low-frequency modes have significant importance on mode coupling chatter, where the milling operation's stiffness is higher than robot's structure stiffness. In robotic milling applications, alteration of the feed direction[11][12][13] or the robot configuration might be considered as alternative approach to accomplish expanded stability limits. Bisu et al. [14]investigated the dynamic behavior of a 6-axis industrial robot for machining operations with a high-speed spindle mounted. Their examination procedure comprises of three phases, targeting the self-excited chatter frequencies of the robot structure in various configurations while spindle is off ,on and without cutting. According to performed experiments, variety in the vibrations brought about by the robot structure, at various positions. Afterwards, Mejri et al.[15]evaluated the stability conditions for 6-axis industrial robot milling system with a mounted high-speed spindle in working envelope based on experimental findings to investigate the effect of different robot positions and related tool tip dynamics on the stability lobes by using frequency domain solution. The results indicated that robot position and feed direction have important influence on tool tip dynamics. Li et al. [16]examined the impact of tool path and position of the workpiece on stability in robotic milling system. They performed experimental work to obtain modal parameters in three different phases that can be sorted into constant, active without cutting operation and with cutting operation. The scholars observed the variation in robot's dynamic characteristics with respect to tool path patterns, workpiece position and milling modes such as up milling and down. Tunc et al. [13] analyzed the dynamics of the hexapod robotic platform, which is a parallel robot platform, based on impact hammer tests and analysis. Experimental findings and related stability simulations indicated that robot positions affect the tool tip dynamics in terms of stability boundaries and stable cutting limits. Besides, it was shown that due to the flexible structure of the hexapod robot, asymmetrical tool tip dynamics was observed. In such cases, changing the feed rate direction and robot configuration has a significant impact

on the stability of the milling operation and therefore, identification procedure performed to find out stability limits accompanying robot positions and configurations.

Bauer et al.[17] investigated the coupling between milling process and robot structure for model-based compensation to reduce the deviations along the tool path. First, authors modelled robot based on kinematic and dynamics properties and, milling forces. Second, they investigated the static stiffness properties and carried out experimental investigations on the robot's structure for modal parameters. Eigenfrequencies of KUKA KR210 robot are obtained where experimental findings indicated that the first three dominant frequencies variation observed for 8.4 Hz, 11.1 Hz, and 16.9 Hz, respectively. Finally, parameter identification procedure is followed and compensation strategies for deviation of the tool path is applied. The results shown that a certain reduction is achieved. Zhang et al.[18] shown that stability conditions of the milling operation rely upon robot position and configuration in terms of variation in stiffness, mass and damping parameters in the suitable working zone.

Guo et al.[19] described the problem as the relatively low stiffness of robot and suggested that low stiffness can seriously affect its positioning accuracy and its machining quality. They used posture optimization method to increase the stiffness of the robot in machining applications. First, they establish a strong mathematical model address stiffness of the robot. Based on analysis of the robot stiffness in a certain direction, the authors study overall stiffness of the robot and introduce a performance index to evaluate the stiffness of the robot with a particular posture. The performance index estimates the stiffness of the robot with a given posture after the relationship between the translational displacement of the robot and the effector and the force applied on it was determined. The results indicate that the application of the proposed method in the robotic drilling was effective to increase the stiffness of the robot and improve the machining quality. Furthermore, the experimental findings suggest that the deviation angle of the tool axis was reduced. Abele et al.[20] highlighted the challenges in robotic milling; in particular, high process loads' effects on the accuracy of the robot and the static path displacement. To address the aforementioned challenges, the authors proposed two different methods: analytical stiffness model and experimental stiffness model. The authors described the modeling of the robot structure and the identification of its parameters with the focus on the analysis of the system's stiffness and its behavior during the milling process. The findings indicated that the analytical method is sufficient enough to calculate the Cartesian compliance with the help of the known joint rotational compliance. According

to the findings, the disadvantage of the experimental method is the large experimental effort when analyzing a bigger workspace and the limited transferability to another workspace. With the information about the captured process forces and the compliance model, the tool path can be controlled; therefore, the accuracy of an industrial robot for machining application can be increased. Liu et al.[21] presented a vibration analysis for natural frequencies of robot. The different modes with accompanying frequencies for the robot having crack and without having crack are analyzed based on the finite element method. In order to investigate the effect of cracks on the structure of the robot, a finite element model is established by ANSYS where the model is designed with crack and without crack and the frequencies at three different modes are obtained. Finite element techniques of analysis and simulation of mechanical systems is used to build mathematical models and to analyze the static and dynamic behavior of the structural elements without of experimental work. The methods of domain discretization supported by the finite element method are popular due to its practicality and versatility which can also be used to find out the natural frequencies of the structure. It can be noticed that with the presence of crack, frequency of vibration increases compared to first mode, second mode and third mode of vibration, and it is concluded that significant variations are observed in mode shapes due to presence of crack.

Zhang et al.[22] emphasized the impacts of less rigid structure, which is stated as the main reason for the deflection of the end effector due to dynamic cutting forces during milling operations, of the industrial robots in high precision aerospace industry demands. Therefore, to find joint stiffness and optimize the posture of the robot, the authors established an enhanced stiffness model that contains a kinematic description of the robot and the jacobian model of the robot. The authors indicated that complementary stiffness can be neglected when applied forces are small compared to the payload of the robot. Hereafter, the authors convert the stiffness matrix to the compliance matrix and divided the compliance matrix into three different sub-matrices that sorted into translational, coupling, and rotational compliance. Milling model introduced and cutting moments are ignored due to the small radius of the cutting tool. Hence, the translational compliance part of the compliance matrix is taken into consideration in the determination of the performance index evaluation of the robot stiffness and compliance ellipsoid is transferred to the TCP (tool-center-point) via a transformation matrix. Thus, compliance coefficients and accompanying directions are characterized. In that manner, the

performance index (ks) for stiffness evaluation procedure is established and larger ks result in larger stiffness values for the different postures of the robot. Whereupon, to avoid singularity and violations of the joint rotations, the authors proposed another performance index, kf. Based on these performance criteria, the authors proposed an extensive optimization for posture identification. By using this optimization methodology, an optimized posture has been identified to reduce the translational deflection of the end effector of the robot. Hao et al.[23] conducted several experiments to verify whether the regenerative chatter theory is applicable to robotic high-speed milling due to largely shifting robot modes dependent on joint configuration and dynamic parameter variation. Thus, robotic milling experiments are divided into two sections. First, modal hammer tests are conducted to predict stability lobe diagrams. Second, experimental verification based on modal stability predictions is carried out. As a result of the high-speed milling experiments, regenerative chatter theory is tested for industrial robots and applicability of the theory is proven. Low-frequency band is investigated, and result is stated that even dynamic stiffness of Z-axis is lower compared to X-axis and Y axis, high speed milling is not affected the Z-axis vibration. Z-axis vibration can be induced when low-speed milling applied. Other considerations are specified as static stiffness, trajectory errors, forced vibration and motion coupling, respectively. Static stiffness of the robot is identified based on experiments with load and displacement. Stiffness is found greater in X direction and greater stiffness is expected to be result in good surface finish. However, based on findings, greater stability has no remarkable differences due to trajectory errors which varies around selected reference in Z-coordinates. The trajectory error left notable marks on surface finish. Furthermore, milling forces' excitation on the robot structure does not have an influential effect and motion coupling, which contains simultaneous working of the robot actuators, cause undesired deviations and oscillations around cartesian axes. Sui et al.[24] addressed the challenges in machining with industrial robots. Especially, the authors emphasize the importance of high level of vibrations during machining due to low stiffness of the industrial robots. The milling experiment was carried out for aeronautical aluminum alloy (7050-T7451) by using industrial robot (KUKA KR 210 R2700). Different process parameters and robot postures were used in order to evaluate vibration characteristics of industrial robot that exposed cutting forces during machining. Vibration signal was measured by using KD10005LA three acceleration transducers and these signals were acquired by B&K testing system. This system consists of data acquisition board, charge amplifier and signal analyzer software.

The authors stated that in the case of lower spindle speed and feed rate, vibration is minimum. Moreover, additional result is that in all the case start point of vibration acceleration is approximately same due to impact of tool and workpiece is same. According to vibration analysis and 3D surface topography results, optimum posture of robot is decided as Pose No 2. Lowest value of average surface roughness value is approximately 0.63 μm. As a result, down-milling should be applied in robotic machining due to unstable direction of cutting forces in up-milling. Different robot poses generate distinct surface roughness due to chatter in machining. Optimum surface quality is observed at pose 2. Authors stated that vibration signal reduction was observed at the cutting speed of 1000 rpm and the feed rate of 0.04 mm/s. Additionally, better surface quality has obtained at spindle speed of 800 rpm and feed rate of 0.05 mm/s, feed rate of 0.3 mm/s and cutting speed of 1200 rpm. Cordes et al. [25] investigated the effects of chatter mechanisms, which recognized as regenerative and mode coupling chatter, in robotic milling. To predict and identify the behavior in terms of stability, the robotic milling system's structural dynamic model, which includes the robot, spindle, tool holder, and tool, is introduced and a dynamic cutting force model is applied. Stability analysis is carried out via different methods such as zeroth-order approximation with cross-coupling, zeroth-order approximation with cross-coupling, and semi-discrete time-domain method with cross-coupling. Stability predictions are conducted regarding different modes of the structure of the robotic system and different materials; aluminum and titanium, respectively. Stability analysis indicated that stability limits immensely varies due to cross-coupling, which is not usual in more rigid machine tools, in low – frequency modes. In high-speed cutting tests of aluminum, findings point out that predictions and experimental results are consistent. Chatter was encountered due to tool and spindle modes which is predicted. In this region, chatter is dominated by the tool-spindle modes. However, in the low-frequency region or low-speed titanium cutting tests, incompatibilities were detected due to the flexible structure of the robot and the main reason for chatter in low-frequency modes range is identified as the robot's structure.

Wang et al.[26] investigated the stability characteristics and explored the chatter mechanism in robotic boring operation with a mounted pressure foot on its end-effector. Authors elaborated cutting force model by including the effect of cutting speed and using multi-dimensional approach, which divides the uncut chip thickness to the small elements such as triangles and parallelograms, for robotic boring operation. The effect of the

pressure foot on cutting forces and the system's stability has analyzed, and the contribution of the foot is summarized. Hereupon, based on cutting force model, chatter modeling has been established to predict stability limits. To demonstrate the predicted stability limits and to analyze the chatter mechanism, authors have carried out experiments. Dominant machining parameters, depth of cut and feed rate, on chatter, and effects of robot's stiffness highlighted. Experimental results showed good agreement with prediction results. Other effects of the instability discussed regarding experimental findings which indicated that chatter largely affects the surface finish of the machined part while forced vibration distorts the circularity of holes. Denkena et al.[27] addressed the challenges in the accuracy of robotic machining due to cutting forces that occur during milling operation and gravity load on the arms. Thus, the authors proposed a real-time compensation method to improve the accuracy of the process by using a spindle, that has the ability to sense forces and stiffness model of the robot which enables the calculation of deviations. By using communication between controller, and sensing unit and the stiffness model, authors created information as an output of the combined system for robot to adjust itself. To increase the sensitivity of the sensing devices (strain gauges), the finite element method is used and facilitated the determination of the mounting point and the positions on the side of the spindle. The orientation of the spindle is adjusted by taking force distribution into consideration. The calibration of the sensing unit has been accomplished by a three-axis dynamometer. Deviations are compensated up to 0.02 mm via the experimental validation of the proposed system.

1.3 Chatter Suppression-Attenuation and Delaying Techniques for Robotic Milling

Some scholars have proposed various techniques to prevent or suppress chatter during robotic milling operations. Özer et al.[28] studied the chatter phenomenon in robotic turning to delay the chatter start frequency by using novel semi-active control technique that contains process model (undulated chip thickness) and structural model of robotic arm that consists of 2 links developed using Finite Element Method. This technique suggested that chatter can be controlled by changing the stiffness. As a result of changing the stiffness of the arm two times or three times over a period of time, stable region is increased a certain extent and cutting performance is increased 2.5 times compared to uncontrolled case. These improvements applied as on-off control semi-active vibration suppressor without any hardware change. He et al.[30] highlighted the tendency to mode

coupling chatter vibrations in robotic milling applications due to lack of rigidity and irregular shape of the robot's structure. First, machining force analysis completed to show tangential cutting force coefficient is more dominant compared to radial force and stability criteria is formed based on cutting force analysis, 2 DOF dynamics of robotic milling, and robot kinematics to acquire stiffnesses in the plane. Second, process stiffness and the angle between the stiffness direction and the force direction are used with the modal analysis of the robot structure to evaluate stable zones in cutting operation. An optimization scheme has applied to find feed direction-based stability evaluation. Thus, eligible robot posture and stable cutting direction have been identified and a meaningful improvement has observed. Sun et al.[29] addressed the chatter issues in conventional robotic milling and proposed a novel method for chatter suppression. This technique is named as robotic rotary ultrasonic milling which enables the chatter attenuation due to reduction in the dynamic milling forces and reduction in the amplitude of the vibration. To investigate the effects and analyze the stability characteristics of the robotic rotary ultrasonic milling operation, authors developed a model that contains dynamic equations and analysis of motion with the dynamic chip thickness model, which includes Z-direction effects and directional displacements, to simulate dynamic milling forces and thus, stability analysis by using semi-discretization method. To verify the model and analyze the effects of rotary ultrasonic milling on chatter, authors conducted experiments. Experimental findings indicated that surfaces marks left by conventional system and novel method differs enough to prove that suppression by the novel method has been achieved. Rotary ultrasonic milling has been used as a preventive action for chatter. Thus, certain improvement in the stability lobes is observed.

Mousavi et al.[31] addressed the challenges in machining with anthropomorphic robotic manipulators. According to the research, productivity in robotic machining processes is limited due to the low rigidity of robot structure and vibration instability in machining (chatter). To address the challenges mentioned above, Mousavi et al.[31] proposed a multi-body dynamic model of a serial robot is elaborated using beam elements which can easily be integrated into the machining trajectory planning. They suggested to use MSA (Matrix structural analysis) instead of FEM (finite element method), since using FEM of the real robot body geometries is ineffective for the dynamic modeling and simulations of a machining trajectory. Mousavi et al.[31] developed a mathematical model and numerical example to predict the dynamic behavior of robotic manipulator in a machining

operation. The mathematical model enabled stability limits to be determined along machining trajectories. Stability limits predict the robot configuration for which machining operations were at a maximum stable margin. Mousavi et al.[32] suggested to use a beam element model by using matrix structural analysis for the reduction of computation cost. Authors stated that simplified but accurate model should be acquired to predict chatter along the tool path. To make this model more precise, two step calibration procedure has been followed which consists necessary adjustments of geometric, material and damping parameters. In this calibration procedure, to find accurate model parameters, experiments are conducted. By the help of calibration procedure, dynamic behavior of the robot predicted that is demonstrated by matched numeric frequency response function and experimental frequency response function. Based on robot's dynamic behavior and regenerative chatter theory, stable working zones and therefore maximum allowable cutting depths along the tool path are identified. Mousavi et al.[33] proposed a methodology to improve the stability limits of the robotic machining by using a single degree and two degrees of functional redundancy. Based on the regenerative stability theory and numerical model of the robot, by MSA (matrix structural method analysis) that contains 3D beam elements and these elements constitutes the robot model, stability borders of the machining operation have been determined. They attached a frame to the tooltip, which brings about a single degree of functional redundancy, to demonstrate the variation in the dynamic behavior of the robot by using redundancies of the axes instead of changing cutting parameters. Just only changing the single degree of functional redundancy that can be described as a rotation of the robot structure while maintaining the same position and the orientation of the tool axis, improvement in stability conditions are observed. Furthermore, additional improvement has been observed by adding another functional redundancy that comes from the rotary table in which the workpiece is mounted. Stability limits increased significantly by using two degrees of functional redundancy under identical cutting conditions. Furthermore, Mousavi et al.[34] validated the proposed methodology by conducting machining tests with respect to stability simulation results along a tool path. In the first configuration scheme, the 5 mm depth of cut is determined to be in the stable zone as a result of stability simulation using a single degree of redundancy. However, in the second configuration scheme, reachable depth of cut is found 8 mm by using two degrees of functional redundancy. To demonstrate the impact of the robot configuration and the rotary table, which introduces the two degrees of redundancy, on the stability, 5

mm and 8 mm cutting depths are used in the first configuration and second configuration schemes. According to the results, the prediction from the theoretical stability limit diagram was consistent with the observations obtained from experimental cutting results. Thus, the applicability of the functional redundancy to increase the stability limits of the machining operations is demonstrated.

Gienke et al.[35] investigated the intriguing mechanism of mode coupling chatter phenomenon, which is stated as most influential chatter type in robotic milling applications, to predict stable cutting conditions and avoiding chatter occurrence situations. Authors proposed a combined modelling system as a software tool to predict chatter without any experimental work. First, they established kinematic model of the robot by using D-H notation that contains tool side attached to the end effector of the robot and then, Jacobian analysis elaborated due to targeting small displacements. Work-piece side accepted as rigid and focused on robot-tool structure. In detailed robot-tool structure, authors identified stiffness of the joints experimentally. Additionally, CAD data provided by the manufacturer of the robot, is accepted for identification of the mass properties (such as center of mass, mass and inertias) of the robot. Resulting cutting force representation has been carried out by using non-linear model and to identify the components of the model least square methods are used. Before developing appropriate chatter methodology, agreement between the modeled and measured eigenfrequencies checked. Then, authors stated that good agreement has been observed. After that, chatter prediction procedure with the help of diagonalization of the mass and stiffness matrix, and necessary transformation due to decoupled coordinates dimensions. Thus, important criteria determined to create backbone of the proposed software. Based on the developed software, which shows chatter occurrence based on selected machining parameters, robot configurations, work-piece locations and orientations with milling modes (up milling or down milling) and tool geometry avoidance can be ensured by changing parameters. Experiments demonstrated the usefulness of the tool and possible actions to take prevent chatter. Yuan et al.[36] proposed a chatter suppression technique by using semi-active magnetorheological elastomers absorber while targeting specific range of frequencies. To analyze chatter behavior in different working conditions and varying natural frequency values with respect to different configurations, authors developed a model that contains robot's mass(inertia) matrix, stiffness matrix (which is identified experimentally), based on kinematics. Cartesian stiffness and cartesian mass matrix obtained by employing

jacobian. Damping effect of the structure has neglected due to insignificant effect on the improvement of the stability limits for mode coupling chatter mechanism. Thus, by solving the characteristic equation of motion, first three base frequencies, which are dominant for the mode coupling, are identified and simulation results located between 6 Hz and 20 Hz. Target frequencies that required for the design of the absorber, are acquired by model. Operation mode of the absorber is selected as shear mode due to mode coupling chatter formation plane is accepted as horizontal plane. First experiments are conducted to evaluate performance of the absorber. By changing current, natural frequency values of the absorber obtained and relation between the applied current and the accompanying value of the natural frequency is obtained. Later, secondary experiments are carried out to evaluate performance of the absorber without control and with proposed control scheme on robotic milling application. In without control case, experimental findings indicated that even chatter frequency and the natural frequency of the absorber slightly differs, chatter attenuation has observed. Additionally, if chatter frequency and natural frequency of the absorber matches, absorber shows excellent performance to suppress chatter. In semi-active control case, experimental findings demonstrated that chatter suppression has been accomplished or great amount of reduction has achieved. Furthermore, surface quality is improved.

Cen et al.[37] proposed a method to avoid mode coupling chatter, which is accepted as the main reason for the chatter for low-speed milling in robotic machining, by using the angle between the average cutting force vector and stiffness direction of the robot. Instead of changing workpiece orientation or feed direction, alteration of the maximum principle stiffness put forward to minimize angle that is between the maximum principal stiffness of the robot and the force direction. The stiffness model of the robot has been built through the kinematic Jacobian of the robot based on the CCT (conservative congruence transformation) matrix which enables to take milling forces into the account. The mechanistic approach is used to model milling forces. Radial, axial, and feed direction of the force were able to add to the model by the help of the transformation of the stiffness matrix of the robot. Cutting stiffnesses are determined with respect to small deviations in x and y directions. By diagonalizing the matrix with similarity transformation, the stability criterion has been deduced. This criterion allows to decide whether the cutting operation is stable by comparing eigenvalues and angle. This criterion is created the backbone of the adjustments of the machining parameters regarding whether eigenvalues

real negative numbers. Based on the result of the criterion, feed rate adjustments have been carried out. Different experiments are carried out to identify the stiffness of the robot and to verify the proposed methodology. A known magnitude of force has applied to the end effector and measured via laser to find deflections and related stiffness values. To verify the method, different feed rates selected to observe the chatter characteristics and to minimize the angle by modifying feed rates. An immense reduction has been observed in average cutting forces while improvement observed in surface roughness. Additionally, simulation results showed the preferable configurations of the robot to optimize the angle instead of feed rate adjustments. Cen et al. [38] proposed a novel online chatter detection and suppression system, which contains hardware such as a PVDF sensor and dynamometer, supported by software that contains chatter detection algorithm and a feedback scheme. First, authors developed mode coupling chatter model to determine cutting conditions and angle that corresponds to chatter and represents the angle between maximum principal stiffness of the robot and average cutting force vector. In this manner, the aforementioned angle and stiffnesses are calculated along a divided toolpath. Thus, length of the divisions controlled by using this angle based on selected feed rate and if the maximum allowable change in the angle exceeds the limits of the robot's payload or abruptly decreases the feed rate, divisions of the tool path makes itself smaller and calculations start over to find appropriate feed rate along the tool path. Authors tested the proposed system, via experiments with feedback and without feedback, to observe the behavior of the system in real-life applications due to uncertainties in the model and the false alarm issues in the hardware during chatter detection. Experimental findings indicated that the proposed system greatly attenuated and suppressed the chatter.

Tunc et al.[12]proposed a new methodology to avoid chatter with respect to different tool path patterns regarding position dependency and asymmetrical tool tip dynamics. To perform modal hammer impact tests, different locations are selected on the workpiece. After conducting hammer tests, FRF results oriented from global coordinate frames to feed and cross-feed directions. A huge difference between the FRF of the different positions has observed and it is stated that increment in FRF results doubled even tripled where the robot moved from the predetermined first position to the last position in terms of amplitude. Stability simulations carried out to demonstrate the effect of feed rate direction and positional correlation in order to evaluate chatter characteristics. Based on simulation results, stability lobes are plotted in each position regarding the radial depth

of cut. To determine the feed rate direction, absolute stability limits, and index for absolute stability are calculated in order to find optimum direction selection during machining. Experiments are performed to verify the optimum selection of the direction and a meaningful improvement in absolute stability is observed where the maximum stability improvement is doubled.

1.4 Research Gap & Objectives of the Thesis

As mentioned in the given literature review, several approaches are presented by scholars to suppress or avoid chatter vibrations and, improve the stability characteristics of industrial robots for robotic milling applications. These approaches can be sorted into stiffness properties of industrial robots, finite element modeling of industrial robots, posture optimization techniques to adjust directional stiffness parameters, single or two degrees of functional redundancy utilization for increased stability limits, feed rate direction selection for improved stability and increased cutting depths, modeling of industrial robots for the prediction of chatter and online chatter suppression strategies. However, the utilization of industrial robots for machining applications requires further investigations in terms of vibration and accuracy. Therefore, preventing chatter is still an important topic for robotic milling applications. Objectives of this thesis are oriented to analyze the dynamic behavior of the robot's structure based on different robot postures and effects of the different postures on the tool tip dynamics, and enabling the prediction of the natural frequencies of the robot by modeling robot dynamics in a simulation environment. In order to achieve these objectives, the subsequent steps are followed:

1. Robot dynamics are modeled based on robot kinematics.
2. Representative natural frequency identification is accomplished and compared with experimental modal analysis results.
3. Tool paths and related G-codes are generated.
4. Tool paths are partitioned with respect to the predetermined locations on the workpiece for use of impact hammer test.
5. FRFs of tool tip are obtained regarding positions and configurations.
6. Stability lobe diagrams are generated.
7. Maximum stability conditions are identified for each location with respect to the configuration variation.
8. Maximum allowable cutting depths are obtained.
9. Configuration sequence is generated regarding improved stability conditions.

1.5 Organization of the Thesis

This thesis organized as follows: In Chapter 1, related literature search is given regarding the objectives of the thesis. This is followed by the robot kinematics according to the rules of Denavit-Hartenberg[39] is explained. Different modeling strategies for robot dynamics based on robot kinematics are explained with their differences and prediction of natural frequencies is presented in Chapter 2. In Chapter 3, the positional and configurational dependency as a result of obtained tool tip FRFs and programming methodology with the selection of the modal hammer test locations is explained. Based on experimental modal test results, stability limits are acquired, and different cases are formed to explore stable cutting condition variation under different constraints such as rotation of redundant axis, constant spindle speed, and variable spindle speed. In addition, comparisons between the cases are elaborated in Chapter 4. Conclusions, contributions and future work are presented in Chapter 5.

CHAPTER 2: Robot Kinematics and Dynamics

The robot kinematics is fundamental for defining position and orientation of the end effector in conjunction with motion analysis of the joints while the modeling of the dynamics of the robots is vital for the investigating of the dynamic behavior of the robots. In this chapter, modeling of robot kinematics and dynamics procedures and systematic implementations are analyzed thoroughly. The robot kinematics is briefly given, and implementation of D-H convention is accomplished. The kinematics model of the KUKA KR240 R2900 is built. Next, methods for dynamic modeling derivations are presented for different algorithms and computation times are compared by using symbolic MATLAB© Toolbox. The Lagrange-Euler implementation for the robot is applied to identify acceleration related terms. Then, approximate stiffness matrix is taken from remarkable journal paper and mass, inertia and center of mass coordinates are extracted from CAD data. Next, natural frequency identification procedure is elaborated.

2.1 Robot Kinematics

Kinematics is a study that consists analytical expression of motion of mechanical systems. Force, torque, mass, center of mass, inertia and this kind of dynamic and physical phenomenon are not involved in this subject. Principally, geometric properties and related motion with mathematical expressions are composed the main area of the kinematic studies. In industrial robotics, robots consist of links associated with one another by rotational joints or translational joints. In this manner, the kinematic investigation can be conducted in two different ways, forward and inverse kinematics. In forward kinematics approach, end effector position and orientation are described as a kinematic chain transformation from joint space to cartesian space. In inverse kinematics, the chain can be solved to identify joint configurations, which can be varied due to reachability of the robot to the same position and orientation with respect to different joint configurations, in joint space when the end effector position is known. Forward kinematics is relatively straightforward to solve compared to inverse kinematics which may need to solve highly non-linear equations and singularity problems.

2.1.1 Denavit-Hartenberg Method and implementation for KUKA KR 240 R 2900 industrial robot

In this section, a well-known methodology is implemented for KUKA KR 240 robot to perform forward kinematics and obtain the position and orientation of the end effector.

The forward kinematics is defined for expression of mathematical relation between adjacent joints, links and description of the end-effector in terms of position and orientation. First, 2 DOF planar robot is analyzed and then, coordinate transformation for the 6-axis KUKA KR 240 industrial robot's frame assignment and homogenous transformations are performed. According to D-H method[39], methodologic homogenous transformation convention is given in the equation (1) and (2).

$$\mathrm{A_i} = \mathrm{Rotation_{z,\theta i}}\ \mathrm{Translation_{z,di}}\ \mathrm{Translation_{x,ai}}\ \mathrm{Rotation_{x,ai}} \tag{1}$$

$$= \begin{bmatrix} C\theta_i & -S\theta_i & 0 & 0 \\ S\theta_i & C\theta_i & 0 & 0 \\ 0 & 0 & 1 & 0 \\ 0 & 0 & 0 & 1 \end{bmatrix} \begin{bmatrix} 1 & 0 & 0 & 0 \\ 0 & 1 & 0 & 0 \\ 0 & 0 & 1 & d_i \\ 0 & 0 & 0 & 1 \end{bmatrix} \begin{bmatrix} 1 & 1 & 0 & a_i \\ 0 & 1 & 0 & 0 \\ 0 & 0 & 1 & 0 \\ 0 & 0 & 0 & 1 \end{bmatrix} \begin{bmatrix} 1 & 0 & 0 & 0 \\ 0 & C\alpha_i & -S\alpha_i & 0 \\ 0 & S\alpha_i & C\alpha_i & 0 \\ 0 & 0 & 0 & 1 \end{bmatrix} \tag{2}$$

Where, θ_i is joint angle, a_i is link length, d_i is the link offset, and α_i is the link twist. The only variable in matrix A is joint angle and other parameters are constant. In the case of prismatic joint, the variable is d_i. Besides creating the arbitrary homogeneous transformation matrix for 3 positions and 3 orientations with 6 parameters, D-H method require 4 parameters to establish the transformation matrix. To implement D-H method, D-H rules should be followed. Rules are the x_1 axis should be perpendicular to the axis z_0, and the x_1 axis should be intersecting the axis axis z_0. In the physical manner, a_i is the distance between the previous z axis and the next one, α_i is the angle between the previous z axis and the next z axis with respect to the normal plane to x axis assigned to the next link, θ_i is the angle between previous x axis and the next one with respect to plane to previous z axis. d_i is the distance between intersection point of the previous axis and next one along previous z axis. To satisfy D-H rules, frame assignment should be started from the base frame, which is defined with the subscript of the axis as "0", to the last frame which is described as n for n-DOF industrial robot. The z axis should be aligned with an actuation axis. This definition of the z axis should be followed until the end effector of the industrial robot.

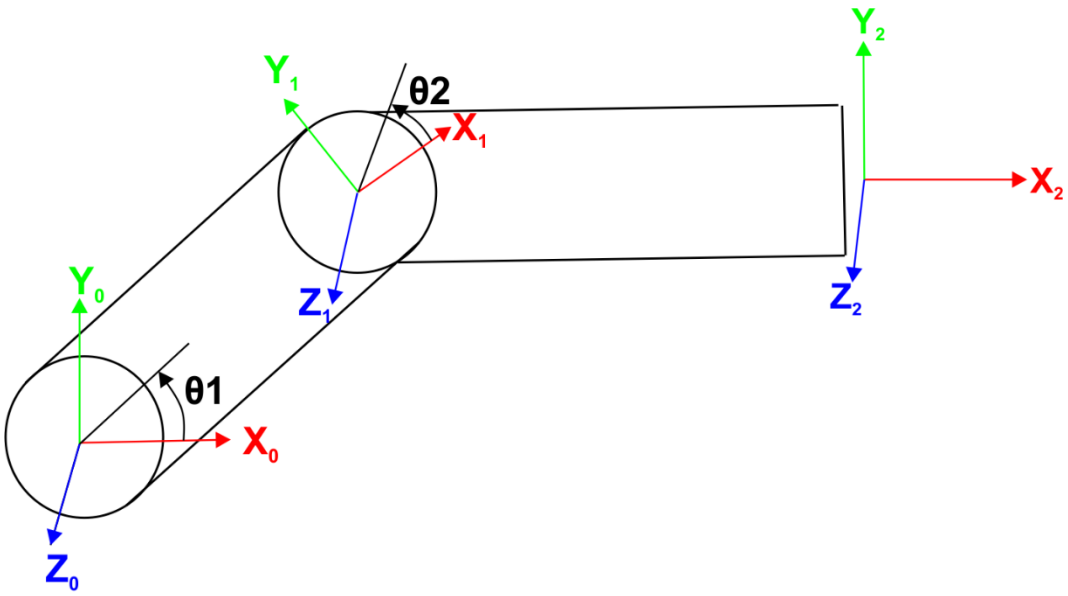

Figure 2-1: 2 DOF planar robot D-H frame assignment and convention

In Figure 2-1, 2 DOF planar robot is illustrated and frames are assigned. Z axes are pointing the out of the page which is accepted as the actuation axis. In this manner, D-H parameters are given in the below.

# link	α_i	a_i	d_i	θ_i
1	α_1	a_1	d_1	θ_1
2	α_2	a_2	d_2	θ_2

Table 2-1: D-H parameters for 2 DOF planar robot

After giving the D-H parameters, homogeneous transformation matrices are established from starting base to the end frame and related matrices are given in the following equation (4) and (5).

$$T_1^0 = \mathrm{A}_1 = \begin{bmatrix} C\theta_1 & -S\theta_1 & 0 & a_1C\theta_1 \\ S\theta_1 & C\theta_1 & 0 & a_1S\theta_1 \\ 0 & 0 & 1 & 0 \\ 0 & 0 & 0 & 1 \end{bmatrix} \tag{2}$$

$$T_2^1 = \mathrm{A}_2 = \begin{bmatrix} C\theta_2 & -S\theta_2 & 0 & a_2C\theta_2 \\ S\theta_2 & C\theta_2 & 0 & a_2S\theta_2 \\ 0 & 0 & 1 & 0 \\ 0 & 0 & 0 & 1 \end{bmatrix} \tag{3}$$

Then, transformation should be multiplied to reach last frame. In this manner, last frame position and orientation are described with respect to base frame. This transformation

multiplication is completed and written as $T_2^0 = A_1 A_2$ in terms of $T_1^0 = A_1$ and $T_2^1 = A_2$ and shown in the equation (6).

$$T_2^0 = \mathrm{A_1 A_2} = \begin{bmatrix} C\theta_1 C\theta_2 & -S\theta_1 S\theta_2 & 0 & a_1 C\theta_1 + a_2 C\theta_2 \\ S\theta_1 S\theta_2 & C\theta_1 C\theta_2 & 0 & a_1 S\theta_1 + a_2 S\theta_2 \\ 0 & 0 & 1 & 0 \\ 0 & 0 & 0 & 1 \end{bmatrix} \tag{4}$$

After 2 DOF manipulator example regarding D-H notation, implementation of the D-H rules is performed for the KUKA KR 240 R2900. In order to mathematically represent the position and orientation of the end-effector, base frame is attached as $X_0Y_0Z_0$. Aforementioned rules are applied to obtain the position and orientation of the end effector and other links for KUKA KR240 R2900. For this purpose, D-H parameters are given in Table 2-2 according to technical specifications given by manufacturer which is shown in Figure 2-2.

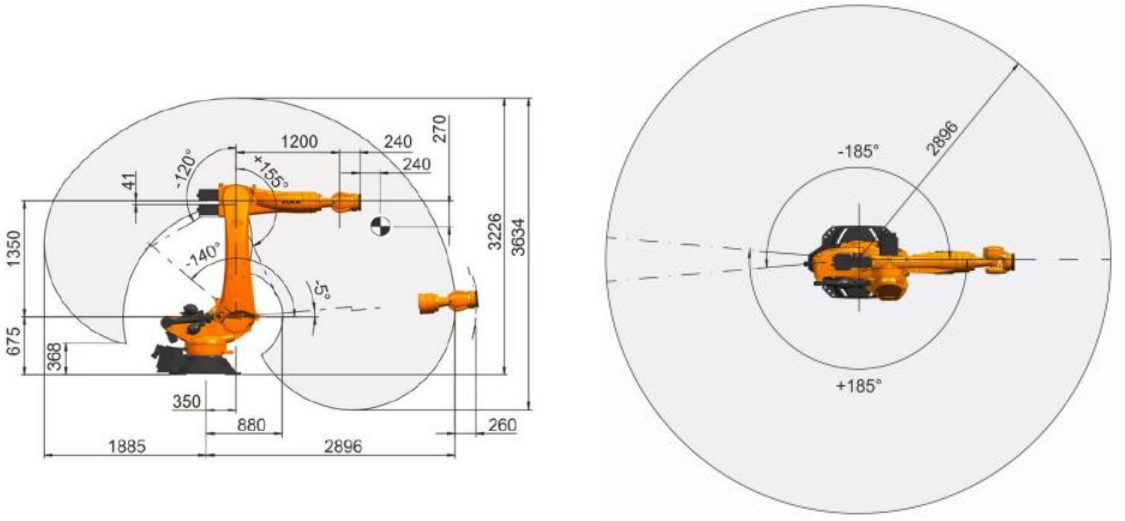

Figure 2-2: Geometric properties of KUKA KR 240 R2900 from the tech specs

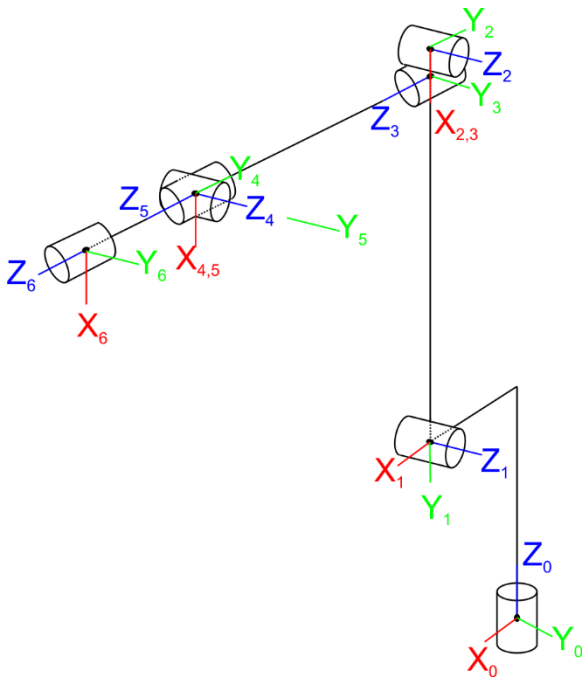

Figure 2-3: Kinematic representation of the KUKA KR240 R2900 / D-H Frames

i	**θ(°)**	**d(mm)**	**A(mm)**	**α (°)**
1	θ1	d1=675	A1=350	α1=-90
2	θ2+90	d2=0	A2=1350	α2=0
3	θ3	d3=0	A3=41	α3=90
4	θ4	d4=1200	A4=0	α4=-90
5	θ5	d5=0	A5=0	α5=90
6	θ6	d6=240	A6=0	α6=0

Table 2-2: Denavit-Hartenberg parameters for KUKA KR240 R2900

After assigning frames and giving kinematic parameters regarding D-H method[39], homogeneous transformation matrices are established in order to find end effector position and orientation. Additionally, all transformations are investigated one by one from equation (5) to (10).

$$T_1^0 = A_1 = \begin{bmatrix} C\theta_1 & 0 & -S\theta_1 & 0.35 * C\theta_1 \\ S\theta_1 & 0 & C\theta_1 & 0.35 * S\theta_1 \\ 0 & -1 & 0 & 0.675 \\ 0 & 0 & 0 & 1 \end{bmatrix} \quad (5)$$

$$T_2^1 = A_2 = \begin{bmatrix} C\theta_2 & -S\theta_1 & 0 & 1.35 * C\theta_2 \\ S\theta_2 & C\theta_2 & 0 & 1.35 * S\theta_2 \\ 0 & 0 & 1 & 0 \\ 0 & 0 & 0 & 1 \end{bmatrix} \quad (6)$$

$$T_3^2 = A_3 = \begin{bmatrix} C\theta_3 & 0 & S\theta_3 & 0.041 * C\theta_3 \\ S\theta_3 & 0 & -C\theta_3 & 0.041 * S\theta_3 \\ 0 & 1 & 0 & 0 \\ 0 & 0 & 0 & 1 \end{bmatrix} \quad (7)$$

$$T_4^3 = A_4 = \begin{bmatrix} C\theta_4 & 0 & -S\theta_4 & 0 \\ S\theta_4 & 0 & C\theta_4 & 0 \\ 0 & -1 & 0 & 1.2 \\ 0 & 0 & 0 & 1 \end{bmatrix} \quad (8)$$

$$T_5^4 = A_5 = \begin{bmatrix} C\theta_5 & 0 & S\theta_5 & 0 \\ S\theta_5 & 0 & -C\theta_5 & 0 \\ 0 & 1 & 0 & 0 \\ 0 & 0 & 0 & 1 \end{bmatrix} \quad (9)$$

$$T_6^5 = A_6 = \begin{bmatrix} C\theta_6 & -S\theta_6 & 0 & 0 \\ S\theta_6 & C\theta_6 & 0 & 0 \\ 0 & 1 & 1 & 0.24 \\ 0 & 0 & 0 & 1 \end{bmatrix} \quad (10)$$

All transformations are given to represent links in mathematical sense. Then, mathematical expression of the end effector's position and orientation with other links are given in terms of homogeneous transformations. These transformations written in the equations (13)-(18) for each frame with respect to base frame in world coordinates. Final transformation for the end-effector represented in the last equation which is given in equation (18).

$$T_1^0 = \mathrm{A}_1 \quad (11)$$

$$T_2^0 = T_1^0 * T_2^1 = \mathrm{A}_1.\mathrm{A}_2 \quad (12)$$

$$T_3^0 = T_1^0 * T_2^1 * T_3^2 = \mathrm{A}_1.\mathrm{A}_2.\mathrm{A}_3 \quad (13)$$

$$T_4^0 = T_1^0 * T_2^1 * T_3^2 * T_4^3 = \mathrm{A}_1.\mathrm{A}_2.\mathrm{A}_3.\mathrm{A}_4 \quad (14)$$

$$T_5^0 = T_1^0 * T_2^1 * T_3^2 * T_4^3 * T_5^4 = \mathrm{A}_1.\mathrm{A}_2.\mathrm{A}_3.\mathrm{A}_4.\mathrm{A}_5 \quad (15)$$

$$T_6^0 = T_1^0 * T_2^1 * T_3^2 * T_4^3 * T_5^4 * T_6^5 = \mathrm{A}_1.\mathrm{A}_2.\mathrm{A}_3.\mathrm{A}_4.\mathrm{A}_5.\mathrm{A}_6 \quad (16)$$

By using the same strategy, frame descriptions with respect to the other frames can be derived by using aforementioned relations. For instance, 4th link's frame can be described with respect to 1st link's frame in the given equation (17).

$$T_4^1 = T_2^1 * T_3^2 * T_4^3 = \mathrm{A}_2.\mathrm{A}_3.\mathrm{A}_4 \quad (17)$$

In this manner, all transformations can be adjusted to other frames which is useful for the dynamics due to dynamics study requires the kinematic relations between frames and center of mass. Furthermore, end-effector's position and orientation are given with 4x4 homogeneous transformation matrix in equation (18) in terms of rotation and translation.

$$T_6^0 = \begin{bmatrix} r_{11} & r_{12} & r_{13} & d_x \\ r_{21} & r_{22} & r_{23} & d_y \\ r_{31} & r_{32} & r_{33} & d_z \\ 0 & 0 & 0 & 1 \end{bmatrix} \tag{18}$$

Where, position is described by $[d_x, d_y, d_z]^T$ which refers the first three row of the last column. The first 3 rows and 3 columns construct the rotation matrix which is $[r_{11}, r_{12}, r_{13};\ r_{21}, r_{22}, r_{23}; r_{31}, r_{32}, r_{33}]^T$. Then, this rotation can be written in terms of roll, pitch and yaw (XYZ). The following equations are used to determine angles. (equation (19)-(21))

$$\beta = atan2\left(-r_{31}, \sqrt{r_{11}^2 + r_{21}^2}\right) \tag{19}$$

$$\alpha = atan2\left(\frac{r_{21}}{\cos(\beta)}, \frac{r_{11}}{\cos(\beta)}\right) \tag{20}$$

$$\gamma = atan2\left(\frac{r_{32}}{\cos(\beta)}, \frac{r_{33}}{\cos(\beta)}\right) \tag{21}$$

If $\beta = \mp 90$, denominator part of the equations (19)-(21) would be zero. In these cases, equation (22) and (23) should be used.

If $\beta = +90$;

$$\alpha = 0\ and\ \gamma = atan2(r_{12}, r_{22}) \tag{22}$$

If $\beta = -90$;

$$\alpha = 0\ and\ \gamma = -atan2(r_{12}, r_{22}) \tag{23}$$

In this section, forward kinematics is solved with implementation of the D-H method[39] for 2 DOF planar robot and 6 DOF industrial robot which is KUKA KR240 R2900. Then, mathematical relations are explained in terms of homogeneous transformations with respect to base and other link frames. Next and the last one is the roll, pitch and yaw angles identification explanation from the rotation matrix. Then, this sub-section is followed by the robot dynamics section.

2.2 Robot Dynamics

After investigating kinematics and assigning the coordinate frames regarding the D-H convention, the dynamic behavior of the serial manipulators can be analyzed. Besides the geometric analysis of the motion, dynamic properties affect the performance of industrial robots. For that purpose, dynamical equations of the serial manipulators should be derived. Dynamical problems are categorized into two different sub-categories: Forward Dynamics and Inverse Dynamics. Purpose of the forward dynamics approach is understanding the response of the manipulator's arm with respect to applied forces and torques on joints. According to given joint torques, motion of the robot can be computed as a function of time. On the other hand, inverse dynamics approach can be used to find torques or forces that exerted on joints for planned trajectory of robot[42][43]. Hollerbach [47] addressed the computation cost and complexity of the inverse dynamic formulations for real-time torque calculations and proposed a recursive Lagrangian approach with 3x3 matrix multiplication to reduce the computation cost for all dynamics related terms such as inertia related matrix, coriolis, and centrifugal terms. $O(n^4)$ derivations reduced to the $O(n^2)$ and computation time complexity was demonstrated as linearly dependent on the joint numbers. Bejczy and Paul[49] developed a symbolic equation procedure for n-DOF robotic manipulator dynamics to control the motion of arms without losing accuracy. Luh et al.[48] proposed a computational scheme for the dynamics of the manipulators by using Newton-Euler equations. Proposed computations are linearly dependent on the number of links contradicting to Lagrange-Euler computations for manipulators. Computation time was obtained as 0.0335 seconds and 0.0045 seconds by using FORTRAN© and the assembly programming language, respectively, regarding the theoretically exact model of equation of motion. Walker and Orin[50] proposed four different methodologies to compute joint accelerations based on established successive kinematic equations by using inverse dynamics to solve forward dynamics. In the first methodology, a vector is created to comprise centrifugal and coriolis accelerations, gravity, and the external forces and moments. This technique has left the inertia matrix on the one side of the equation and on the other side difference of the torque vector and the vector that contains the aforementioned effects has been left. Then, the inertia matrix and related joint accelerations are calculated by setting accelerations and velocities zero. In the second method, the bottom elements of the diagonal of the inertia matrix has calculated. In the third methodology, the top elements of the diagonal calculated. In the fourth method and the last one, joint accelerations are found by iterative procedure and convergence to the

correct solution. The third method was the most effective and fastest one among the other alternatives. The third methodology was used the composite system of the center of mass of the robot bodies which is later named as a composite rigid body algorithm by Featherstone [51][52]. Orin et al.[53] analyzed open chain kinematics and utilized the Newton-Euler approaches with modifications by simplification in the notation and reduction in the computation complexity to solve inverse dynamics problem with computing all forces and moments explicitly. Hexapod robotic vehicle was used to perform experiments and good agreement between the experiments and theoretical results was observed. Simulating motion of serial manipulator allows the using effective control approaches and trajectory planning techniques without physical experiments. Thus, it has significant importance on the cost and effort minimization. Additionally, vibration and related problems can be minimized or prevented by identification of the dynamics. Then, robot dynamics are categorized and explained. Later on, inverse dynamics approaches for industrial robots and identification of the natural frequencies are explained.

2.2.1 Recursive Newton-Euler Approach

Each body of the serial manipulator should be extracted from the entire robot structure and analyzed one by one. This dynamical analysis leads to appear force of constraint between adjacent links. These forces restrict object to follow motion constraints. Additional operations are required to remove these forces of constraint. All the joint reaction forces can be found by using Newton-Euler equations. These reaction forces are required for designing stages such as sizing manipulator links, bearings and actuators. Recursive Newton-Euler formulation algorithm comprises two different stage: Forward computation and Backward Computation, respectively. In Forward computation section, angular velocity, angular acceleration, linear velocity and linear acceleration are computed in a recursive manner. In backward computation section, forces and torques are computed for each link with inter-link forces and torques. All computations are utilized with respect to revolute joints. General recursive Newton-Euler methodology and constraint forces are presented and shown in Figure 2-4. [42][43][44]

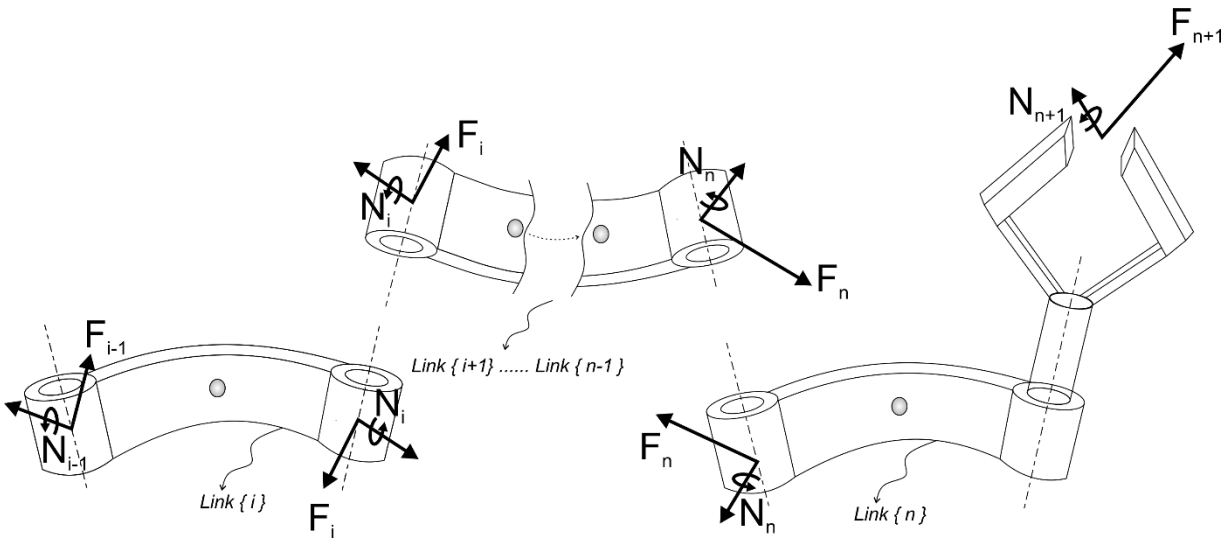

Figure 2-4: Recursive Newton- Euler methodology and inter-link forces

In Figure 2-4, Forces and torques of constraints appear due to removing adjacent links from the main assembly of the industrial robot. These constraints are eliminated in the formulation structure. This elimination procedure adds extra mathematical calculations. However, this formulation is still faster compared to Lagrange-Euler formulation for robot dynamics. Removed link and its physical and geometrical properties are presented in Figure 2-5.

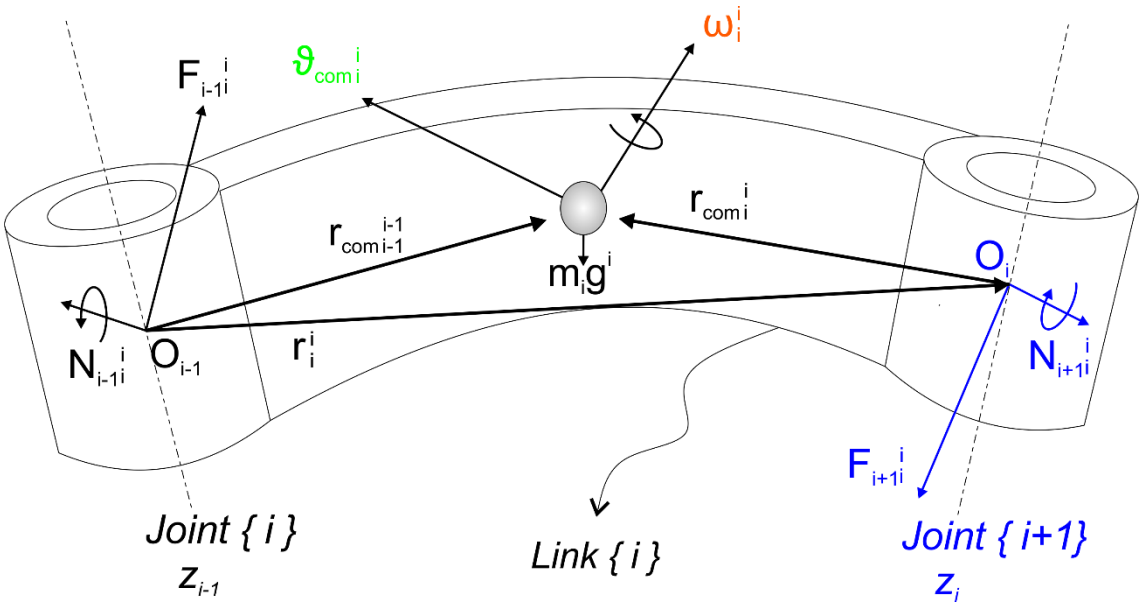

Figure 2-5: Physical and Geometric relations for one extracted link

Where joints and actuation axes are defined in terms of z axis by using subscripts, z_{i-1} is the axis which is assigned to the joint i and z_i is the actuation axis of the joint $i + 1$. A

representative center of mass is located, and gravitational force is represented by $m_i g_i$. Angular velocity is symbolized as ω_i^i and later on, $\dot{\omega}_i^i$ is used for angular acceleration. ${\vartheta_{com_i}}^i$ is used for linear velocity of the center of mass and ${\dot{\vartheta}_{com_i}}^i$ is used for the linear acceleration of the center of mass. r_i^i is used for position vector of the link i with respect to previous link's frame. Then, ${r_{com_i}}^i$ is defined to determine the location of center of mass with respect to joint i where $r_{com_{i-1}}^{i-1}$ defines the relation between joint $i-1$ and center of mass. After establishing necessary geometric relations, force and torques on the joints are calculated by using Recursive Newton-Euler equations which consist two stages, forward recursive propagation and backward recursive propagation, respectively. Calculation steps are explained in section 2.2.1.1 and 2.2.1.2.

2.2.1.1 Part I: Forward recursive equations

In forward computation section, velocity and acceleration propagation can be obtained and backward computation represents the computation of forces and torques in a recursive manner. First, computations start with initial condition that base link has no angular velocity, angular acceleration, linear velocity or linear acceleration. This mathematical relation is given in the equation (24).

Initial condition;

$$v_0 = \dot{v}_0 = \omega_0 = \dot{\omega}_0 = 0 \tag{24}$$

Next, angular velocity and accelerations are propagated in a recursive manner and written in the equation (25) with respect to the previous link frame regarding revolute joints.

$$\begin{aligned} \omega_i^i &= R_i^{i-1}\left(\omega_{i-1}^{i-1} + z_{i-1}^{i-1}\dot{\theta}_i\right) \\ \dot{\omega}_i^i &= R_i^{i-1}\left(\dot{\omega}_{i-1}^{i-1} + z_{i-1}^{i-1}\,\ddot{\theta}_i + \omega_{i-1}^{i-1} \times z_{i-1}^{i-1}\,\dot{\theta}_i\right) \end{aligned} \tag{25}$$

Then, linear velocity and accelerations are propagated by recursive equations and presented in equation (26) in terms of previous link's frame, respectively.

$$\begin{aligned} v_i^i &= R_i^{i-1}\left(v_{i-1}^{i-1} + \omega_i^i \times r_i^i\right) \\ \dot{v}_i^i &= R_i^{i-1}\left(\dot{v}_{i-1}^{i-1} + \dot{\omega}_i^i \times r_i^i + \omega_i^i \times (\omega_i^i \times r_i^i\right) \end{aligned} \tag{26}$$

Linear acceleration of the center of mass can be expressed in terms of linear acceleration propagation which is written in equation (27).

$$\dot{v}_{com_i}{}^{i} = \dot{v}_i^i + \dot{\omega}_i^i \times r_{com_i}{}^{i} + \omega_i^i \times (\omega_i^i \times r_{com_i}{}^{i}) \tag{27}$$

In general, an arbitrary point on the link can be described by position vectors. To compute the acceleration of the center of mass, the location of the mass should be known, and it can be expressed in terms of position vector which contains the position information about the center of mass with respect to link parameters that correspond to link twists and offsets. In such a manner, the position vector is given in equation (28).

$$r_i^i = \begin{bmatrix} a_i \\ d_i S\alpha_i \\ d_i C\alpha_i \end{bmatrix} \tag{28}$$

Then, gravitational acceleration is expressed in terms of previous link's frame and it is written in equation (29).

$$g^i = R_i^{i-1}\ g^{i-1} \tag{29}$$

2.2.1.2 Part II: Backward recursive equations

After the gravitational acceleration computation for each link, the forward propagations of the velocity and the accelerations are completed in a recursive manner. This is followed by backward propagation of forces and torques starting from the end effector and ending at the base link. First, moments and forces exerted by the inertia and linear acceleration of the center of mass on the location of center of mass are calculated by using equation (30).

$$\begin{aligned} F_{com_i}{}^{i} &= -m_i\ \dot{v}_{com_i}{}^{i} \\ N_{com_i}{}^{i} &= -I_i^i\ \dot{\omega}_i^i - \omega_i^i \times (I_i^i\ \omega_i^i) \end{aligned} \tag{30}$$

Where, I_i^i is inertia parameters expressed in the link frame with respect to center of mass. Then, force and moment balance equations can be written around center of mass of the current link which is defined by superscript and subscript i . These equations are given in the equation (31) as a recursive form.

$$\begin{aligned} F_{i-1_i}{}^{i} &= F_{i+1_i}{}^{i} - m_i g^i - F_{com_i}{}^{i} \\ N_{i-1_i}{}^{i} &= N_{i+1_i}{}^{i} + \left(r_i^i + r_{com_i}{}^{i}\right) \times F_{i-1_i}{}^{i} - r_{com_i}{}^{i} \times F_{i+1_i}{}^{i} - N_{com_i}{}^{i} \end{aligned} \tag{31}$$

Then, equation (32) is used for the transformation of torques from current link frame to the previous link frame.

$$F_{i}{}_{i-1}^{i-1} = R_i^{i-1} F_{i-1}{}_{i}^{i}$$
$$N_{i}{}_{i-1}^{i-1} = R_i^{i-1} N_{i-1}{}_{i}^{i} \tag{32}$$

Next, torques for joints are obtainable by using projection of inter-link forces with respect to accompanying joint axes. To obtain joint torques, equation (33) is used.

$$F_{i}{}_{i-1}^{i-1} = \left[F_{i-1}{}_{i}^{i}\right]^T z_{i-1}^{i-1}$$
$$\tau_i = N_{i}{}_{i-1}^{i-1} = \left[N_{i-1}{}_{i}^{i}\right]^T z_{i-1}^{i-1} \tag{33}$$

As a result of forward and backward recursive equations, angular and linear velocities with the projection of the velocity and acceleration for the center of mass, forces and torques by using force and torque balance equations, are found. The algorithm performs recursively in two categories:

- By using known initial conditions, angular velocities, accelerations and linear velocities, accelerations are computed.
- By using known applied forces and torques on end effector -terminal conditions, torques and forces on the joints are computed.

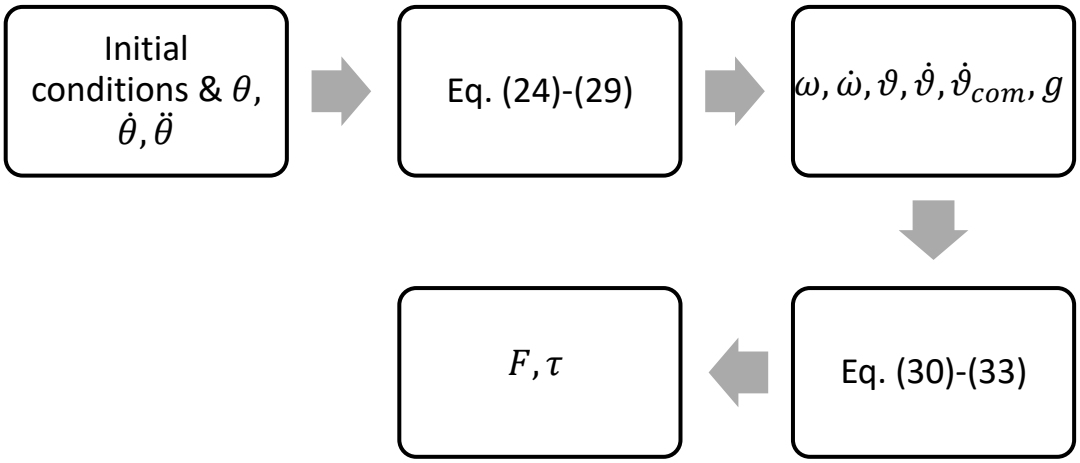

Figure 2-6:Computational mechanism of the Recursive Newton-Euler formulation

In Figure 2-6, calculation steps are schematized. Initial conditions are given as joint position, velocity, acceleration and, base link's angular and linear velocities, accelerations accepted as zero. Next, forward computation is conducted to find related angular, linear velocities and accelerations for the links regarding center of mass. Then, backward

computation is performed to find torques and forces on joints. When the computer simulation of the inverse dynamics of the industrial robot is completed analytically by Newton-Euler formulation, simulation is performed for various scenarios to identify joint torques of serial manipulators. Then, Lagrange equations of motion are derived and analyzed for robot mechanisms in the section 2.2.2. Computations are carried out for 2-D planar serial arm based on given cubic and quintic trajectories. Results are given in section 2.2.3.

2.2.2 Lagrangian Approach

Another formulation is Lagrange equations of motion among mostly used dynamical formulations. The main advantage of the Lagrangian approach is analyzing the serial manipulator as a whole structure without extracting bodies. Therefore, forces of constraint do not appear in the formulation structure. Lagrange formulation can be derived from kinetic (K) and potential (U) energy and their difference in a mechanical system by differentiating energy-related terms with respect to variables of the system and time.[42][43][44]

Lagrangian Function is written as a difference between the kinetic energy and potential energy of the system. This equation is given in equation (34).

$$\mathcal{L} = K - U \tag{34}$$

Lagrange's equation of motion can be formulated in terms of Lagrangian function as given in the equation (35);

$$\frac{d}{dt}\left(\frac{\partial \mathcal{L}}{\partial \dot{q}_i}\right) - \frac{\partial \mathcal{L}_i}{\partial q_i} = Q_i \qquad for\ i = 1,2, \dots \dots \dots n \tag{35}$$

Kinetic energy of link of the serial arm can be written in terms of translational and rotational part of the kinetic energy as stated in equation (36);

$$K_i = \frac{1}{2} V_{comi}^T m_i V_{comi} + \frac{1}{2} \omega_i^T I_i \omega_i \tag{36}$$

Then, inertia of the links is written with respect to link frame in equation (37).

$$I_i = R_i^0 I_i^i (R_i^0)^T \tag{37}$$

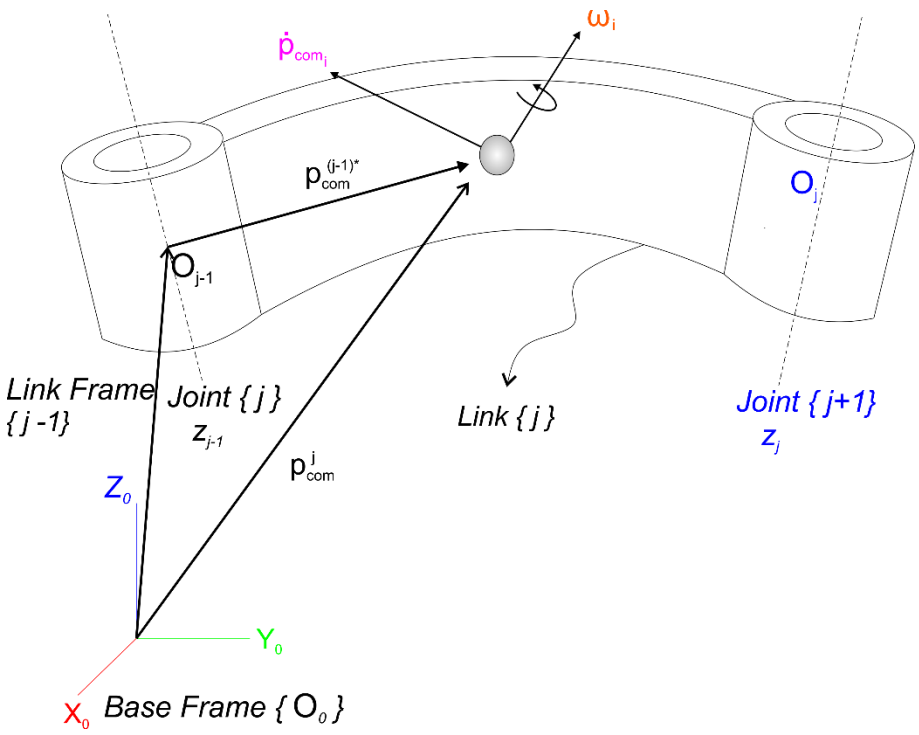

Figure 2-7: Representation of link j by geometrical and physical relations for Lagrangian approach

Necessary vectors are expressed in the link frames with respect to base frame for velocity of links and center of masses in equation (38) and shown in Figure 2-7.

$$\dot{p}_{comi} = \begin{bmatrix} V_{comi} \\ \omega_i \end{bmatrix} \; and \; J_i = \begin{bmatrix} J_{vi} \\ J_{\omega i} \end{bmatrix} \tag{38}$$

Where J_{vi} and $J_{\omega i}$ are sub-jacobian matrices of the link in terms of translation and rotation of the link, and columns of the sub-matrix jacobians can be symbolically represented as J_{vi}^{j} and $J_{\omega i}^{j}$ with the help of superscripts. In physical manner, J_{vi}^{j} and $J_{\omega i}^{j}$ represent partial rate of change of the velocity of the center of mass and the angular velocity of link i with respect to the j-th joint motion. $\dot{p}_{comi}$ consists the linear velocity and angular velocity of the center of mass. For $j \leq i$, equation (39) is obtained based on instantaneous screw motion theory.

$$\begin{aligned} J_{v_i}^{j} &= z_{j-1} \times p_{comi}^{(j-1)*} \\ J_{\omega_i}^{j} &= z_{j-1} \end{aligned} \tag{39}$$

Where $p_{comi}^{(j-1)*}$ is defined as a position vector which started from the origin of the $j-1$. z_{j-1} and $p_{comi}^{(j-1)*}$ are dependent on joint angles. For that reason, link jacobian sub-matrices

are configuration dependent and these matrices can be combined in an augmented matrix as described in the equation (40);

$$J_{vi} = \left[J_{vi}^{1}, J_{vi}^{2}, J_{vi}^{3}, \dots\dots\dots\dots\dots\dots, J_{vi}^{i}, 0,0,0,0,0,0\right]$$
$$J_{\omega i} = \left[J_{\omega i}^{1}, J_{\omega i}^{2}, J_{\omega i}^{3}, \dots\dots\dots\dots\dots\dots, J_{\omega i}^{i}, 0,0,0,0,0,0\right] \quad (40)$$

Then, to obtain the kinetic energy of the system, all motion related parameters are summed, and total kinetic energy is given in equation (41) in terms of linear and angular velocity with jacobian representation.

$$K = \frac{1}{2}\sum_{i=1}^{n}\left(V_{comi}^{T} m_i V_{comi} + \frac{1}{2}\omega_i^{T} I_i \omega_i\right)$$

$$= \frac{1}{2}\sum_{i=1}^{n}\left[\left(J_{vi}.\dot{q}\right)^{T} m_i \left(J_{vi}.\dot{q}\right) + \left(J_{\omega i}.\dot{q}\right)^{T} I_i \left(J_{\omega i}.\dot{q}\right)\right] \quad (41)$$

$$= \frac{1}{2}\dot{q}^{T}\left[\sum_{i=1}^{n}\left({J_{vi}}^{T} m_i J_{vi} + {J_{\omega i}}^{T} I_i J_{\omega i}\right)\right]\dot{q}$$

After the derivation of kinetic energy, $n \times n$ manipulator inertia matrix can be expressed in equation (42) ;

$$M = \sum_{i=1}^{n}\left({J_{vi}}^{T} m_i J_{vi} + {J_{\omega i}}^{T} I_i J_{\omega i}\right) \quad (42)$$

By using this convention, kinetic energy of a robot mechanism can be explained in terms of the manipulator mass matrix and the joint velocity vector. This representation is given in the equation (43).

$$K = \frac{1}{2}\dot{q}^{T} M \dot{q} \quad (43)$$

After deriving kinetic energy, total amount of the stored potential energy of the links is described regarding geometrical definitions under gravitational acceleration. This formulation is given in the equation (44).

$$U = \sum_{i=1}^{n} m_i \, g^{T} p_{comi} \quad (44)$$

Where p_{comi} is the center of mass with respect to fixed based frame and g^T is the vector that represents gravitational acceleration. After providing necessary information and formulation about the foundation of the kinetic and potential energy, Lagrangian function can be used to obtain compact expression to express robot dynamics. This compact form is given in the equation (45).

$$L = \frac{1}{2}\dot{q}^T M \dot{q} + \sum_{i=1}^{n} m_i \, g^T p_{comi} \tag{45}$$

Next, Lagrangian function is differentiated with respect to q_i , $\dot{q}_i$ and t to formulate the equations of motion. To facilitate the derivation, the term of kinetic energy can be expanded into scalars summation where $M_{i,j}$ represents the (i,j) element of the manipulator mass matrix M. Thus, the equation that expressed in (45) can be turned into the form which is stated in equation (46).

$$L = \frac{1}{2}\sum_{i=1}^{n}\sum_{j=1}^{n} M_{ij}.\dot{q}_i.\dot{q}_j + \sum_{i=1}^{n} m_i \, g^T p_{comi} \tag{46}$$

Since it is known that the potential energy does not depend on joint velocity as a system's variable, by taking the partial derivative of equation (46) with respect to system's variable as a joint velocity, equation (47) is obtained.

$$\frac{\partial L}{\partial \dot{q}_i} = \sum_{j=1}^{n} M_{ij} \, . \dot{q}_j \tag{47}$$

After this derivation, derivatives are taken with respect to time and this formulation is yielded in equation (48).

$$\begin{aligned} \frac{d}{dt}\left(\frac{\partial L}{\partial \dot{q}_i}\right) &= \sum_{j=1}^{n} M_{ij} \, . \ddot{q}_j + \sum_{j=1}^{n}\left(\frac{dM_{ij}}{dt}\right).\dot{q}_j \\ &= \sum_{j=1}^{n} M_{ij} \, . \ddot{q}_j + \sum_{j=1}^{n}\sum_{k=1}^{n}\left(\frac{\partial M_{ij}}{\partial q_k}\right).\dot{q}_k.\dot{q}_j \end{aligned} \tag{48}$$

Then, by taking the partial derivative of compact expression of Lagrangian function with respect to system's variable as a joint position, p_{comi} is converted into the i-th column vector of the link jacobian submatrix J_{vj}.Thus, equation (49) is written in the differentiated form of system variables.

$$\frac{\partial L}{\partial q_i} = \frac{1}{2}\sum_{j=1}^{n}\sum_{k=1}^{n}\frac{\partial M_{jk}}{\partial q_i}.\dot{q}_j.\dot{q}_k + \sum_{j=1}^{n} m_j\, g^T J_{v_j}^{i} \tag{49}$$

After several mathematical manipulations and substitutions, dynamical equations of motion are obtained and written in terms of joint torques in equation (50).

$$\sum_{j=1}^{n} M_{ij}\,.\ddot{q}_j + V_i + G_i = \tau_i \tag{50}$$

Where V_i is named as velocity coupling vector which is defined by equation (51) and gravitational force vector is expressed in equation (51) as G_i.

$$V_i = \sum_{j=1}^{n}\sum_{k=1}^{n}\left(\frac{\partial M_{ij}}{\partial q_k} - \frac{1}{2}\frac{\partial M_{jk}}{\partial q_i}\right).\dot{q}_j.\dot{q}_k$$
$$G_i = -\sum_{j=1}^{n} m_j\, g^T J_{v_j}^{i} \tag{51}$$

The first term in dynamical equation refers the inertia torques the second term represents the coriolis and centrifugal coefficients and the third term gives the gravitational effects. Then, dynamic equations can be written in matrix form as in equation (52).

$$M\ddot{q} + V + G = \tau$$
$$V = [V_1, V_2, \dots\dots\dots\dots, V_n]^T$$
$$G = [G_1, G_2, \dots\dots\dots\dots, G_n]^T \tag{52}$$
$$\tau = [\tau_1, \tau_2, \dots\dots\dots\dots, \tau_n]^T$$

The joint velocity squared terms are identified with the centrifugal forces, and the different joint velocity products are identified with the coriolis forces. The manipulator inertia matrix is symmetric and positive definite and therefore, it is invertible. The off-diagonal terms represent the acceleration coupling effect between joints. Coulomb and viscous frictions are not taking into account and simplified form of the equations of motion for robot dynamics are given in Recursive Newton-Euler and Lagrangian formulations with derivations. However, 6 DOF 3D serial manipulator's dynamics is expressed by using the mathematically manipulated version of the Lagrangian approach which is presented by Fu et al.[46] in section 2.2.4.

2.2.3 Comparative study on computation times for Recursive Newton-Euler formulation and Lagrangian approach based on cubic and quintic trajectories by using MATLAB© symbolic toolbox

In this section, an illustration is given in Figure 2-8 for 2 DOF robot mechanism which has rectangular cross-section in order to calculate robot dynamics based on Recursive Newton-Euler and Lagrangian approach.

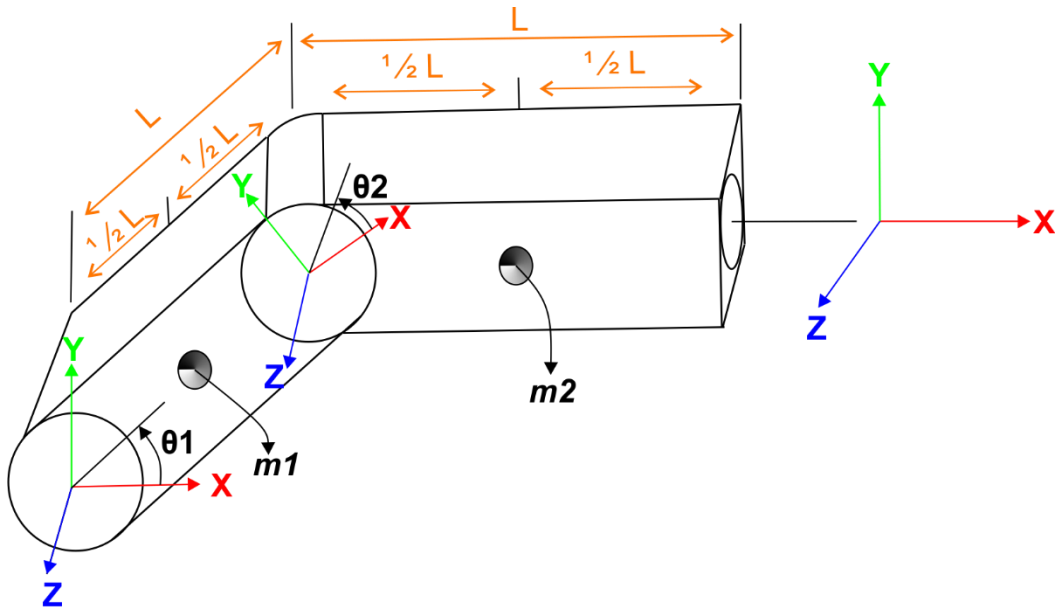

Figure 2-8: Simplified 2 DOF robot structure representation

Structure of the links is assumed as homogenous and center of mass is located in the middle of the links. This is represented by absolute length as L and location of the center of mass is defined as $L/2$ in terms of the absolute length measured from the origin of the related frame. Absolute length of the links is accepted as 1m and mass of the links is defined as 100 kg. $r_{com_i}^{i}$ is written as $a1/2$ which corresponds to $L/2$ in terms of the ratio of the absolute length, and r_i^i is written as $a1$ due to planar mechanism properties for Recursive Newton-Euler formulation. p_{comi} is written for the first link as vector that contains center of mass as a $[a1 * \cos(\theta_1)/2;\ a1 * \sin(\theta_1)/2;\ 0]$ with respect to the base frame and position vector is written as a vector measured from the first frame to the second one as a $[a2 * \cos(\theta_1 + \theta_2)/2;\ a2 * \sin(\theta_1 + \theta_2)/2;\ 0]$. This position vector is $[a1 * \cos(\theta_1))/2 + a2 * \cos(\theta_1 + \theta_2)/2;\ a1 * \sin(\theta_1)/2 + a2 * \sin(\theta_1 + \theta_2)/2;\ 0]$ with respect to the base frame for Lagrangian approach. According to defined lengths, geometric relations and kinematic expressions are derived based on equation (5) and (6).

Then, symbolic representation of inertia properties is given in the matrix form in equation (53).

$$I = \begin{bmatrix} Ixx & -Ixy & -Ixz \\ -Ixy & Iyy & -Iyz \\ -Ixz & -Iyz & Izz \end{bmatrix} \tag{53}$$

Then, inertia matrix is established for the link which has rectangular cross section and symbolic expression of the inertia matrix is given in the equation (54).

$$I_i = \begin{bmatrix} 0 & 0 & 0 \\ 0 & {m_i * L^2}/{12} & 0 \\ 0 & 0 & {m_i * L^2}/{12} \end{bmatrix} \tag{54}$$

The established inertia matrix can be used for Recursive Newton-Euler formulation or Lagrangian approach. Then, torque values are found with for 2 DOF robotic mechanisms by using Recursive Newton-Euler formulations and Lagrangian approach based on single cubic, multiple cubic, single quintic and multiple quintic polynomials, respectively (see Appendix B). Numeric results are shown in Figure 2-9 with computation time.

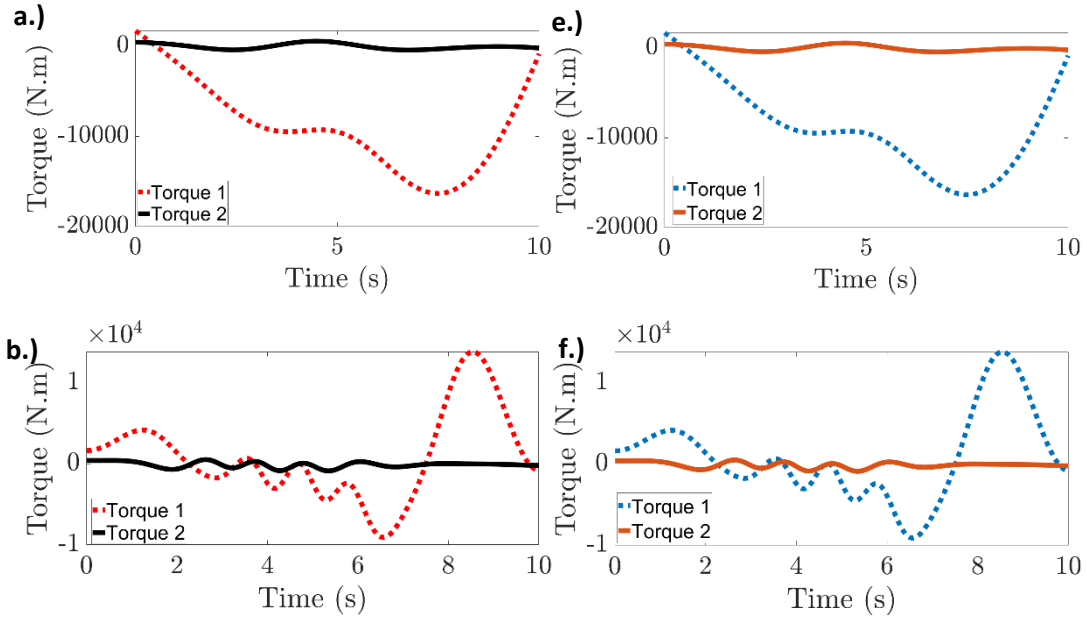

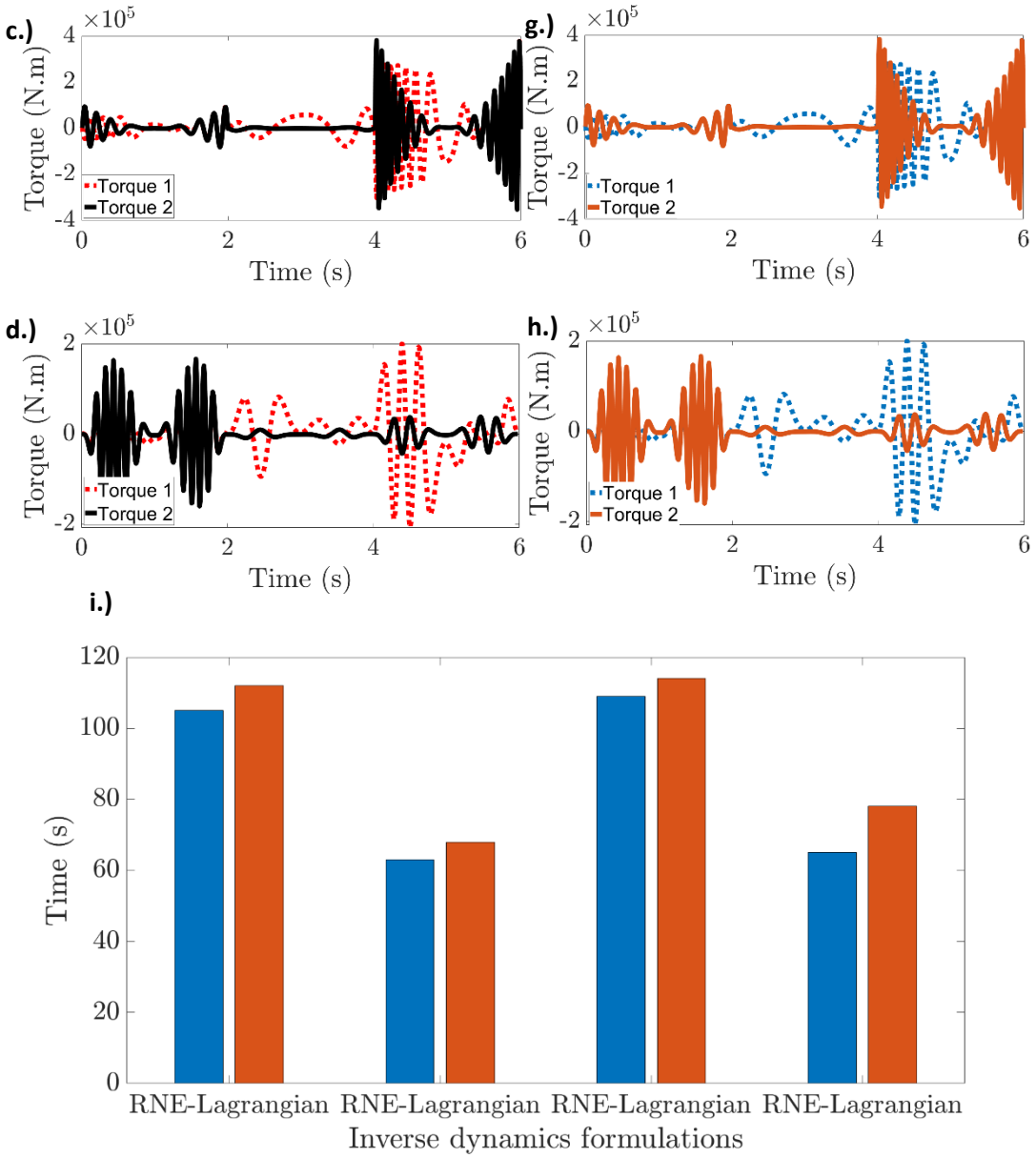

Figure 2-9: Representative torque values for 2 DOF planar robot mechanisms based on predefined (a) single cubic, (b) single quintic, (c) multiple cubic and (d) multiple quintic trajectories with Lagrangian formulation (e) single cubic, (f) single quintic, (g) multiple cubic and (h) multiple quintic trajectories with Lagrangian approach and, (i) computation time comparison

In Figure 2-9 (a)-(b)-(c)-(d), torque values are calculated by using the Lagrangian approach formulation with MATLAB© Symbolic Toolbox. Torque values on joints are calculated by using RNE formulation with MATLAB© Symbolic Toolbox in Figure 2-9 (e)-(f)-(g)-(h). The computation time differences are represented in Figure 2-9 (i). These computations are important to validate each other. Different equation structures are given the same results based on the same trajectories and these results are shown in Figure 2-9

(a)-(b)-(c)-(d), (e)-(f)-(g)-(h) as comparative cases. Computation times are close to each other for both formulations due to symbolic representation and numeric substitution of the symbolic expressions. However, minor differences are still observable between RNE and the Lagrangian approach. The computation cost of the RNE and Lagrangian approach are 105 seconds and 112 seconds for the single cubic trajectory for 10 seconds time interval, respectively. The computation cost of the RNE and Lagrangian approach are 63 seconds and 68 seconds for the multiple cubic trajectory in 6 seconds time interval, respectively. 109 seconds and 114 seconds are found as the computational time for the single quintic trajectory for 10 seconds time interval for RNE and Lagrangian approach, respectively. In the last trajectory, which is multiple quintic trajectory, computational times are found as 65 seconds and 78 seconds. In general, due to the complex structure of the Lagrangian approach compared to RNE, the computation cost is higher. However, in these simulations' differences are negligible due to symbolic derivations and numeric substitutions.

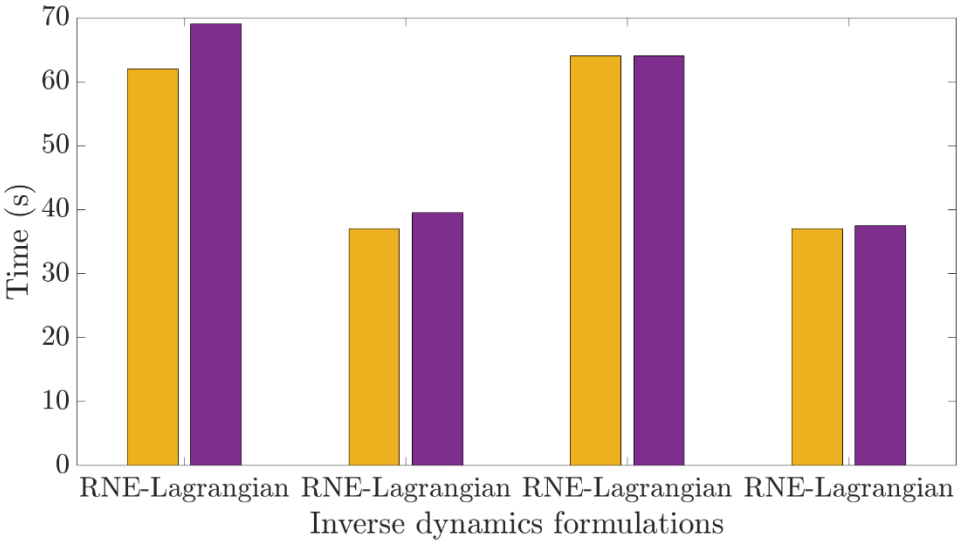

Figure 2-10: Computation time for parallelized algorithm

By parallelizing the loops for substitutions of numeric values into equations, computation time is reduced as shown in Figure 2-10. In such a manner, the computation time of the RNE and Lagrangian approach are 62 seconds and 69 seconds for the single cubic trajectory for 10 seconds time interval, respectively. The computation cost of the RNE and Lagrangian approach are 37 seconds and 39.5 seconds for the multiple cubic trajectory in 6 seconds time interval, respectively. The same computation time, 64 seconds, is obtained for the single quintic trajectory in 10 seconds time interval for RNE

and Lagrangian approach, respectively. In the last trajectory, which is multiple quintic trajectory, computational times are found as 37 seconds and 37.5 seconds. 2 MATLAB© workers are used to speed up the computation time by executing loops for numeric substitutions. Computation times of normal and parallel algorithms are shown in Figure 2-11.

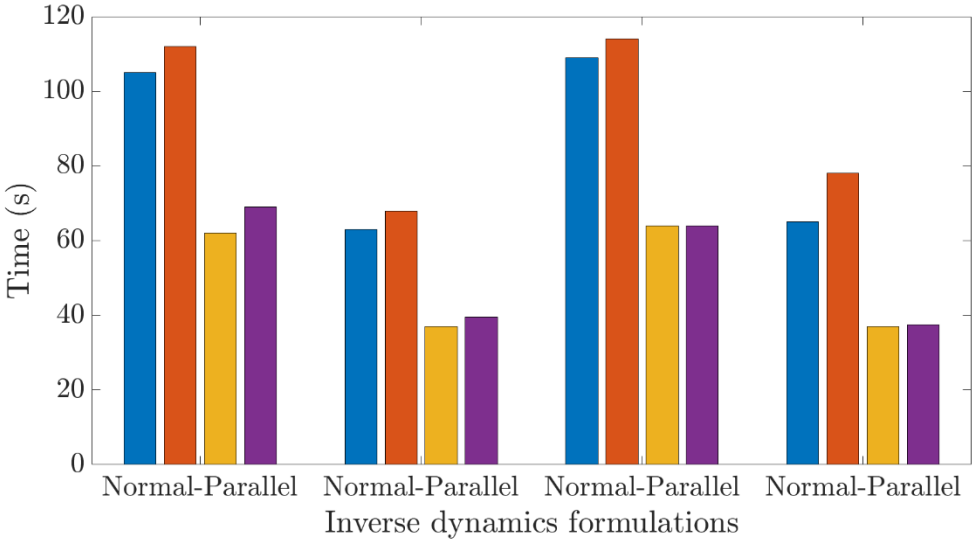

Figure 2-11: Comparison on normal and parallel computing algorithms

RNE computation time is reduced from 105 seconds to 62 seconds. This reduction is around 40.9% for single cubic trajectory. 41.2%, 41.2% and 43.4% reductions are observed for multiple cubic, quintic and multiple quintic trajectories with RNE computation, respectively. 38.4%, 41.9%,43.8% and 42.3% reductions are observed for single cubic, multiple cubic, single quintic and multiple quintic trajectories with Lagrangian computation, respectively. Average reduction is around 41.63%. Thus, significant improvement in the computation time is obtained which corresponds to near half of the computation time without parallel workers. Computation times are relatively high although 2 DOF planar manipulators dynamic models with symbolic derivations and numeric substitutions are used. Therefore, faster approximation algorithm is implemented based on Lagrange-Euler formulation in the next section.

2.2.4 Lagrange-Euler formulation regarding serial manipulator kinematics and implementation of the formulation for KUKA KR 240 R 2900 industrial robot

In this section, another mathematically manipulated version of the Lagrange-Euler approach is used to model 3-D 6 DOF serial manipulators dynamics. Here, D-H

transformation matrices[39] are used to velocity related terms for the points on the link. Velocity related term finding procedure is illustrated in the Transformation matrices are established by using D-H convention with respect to base frame and other links' frames. Then, the derivation of the transformation matrix has been taken for the velocity related terms which is given in the equation (55) as a partial derivative with respect to related joint variable for revolute joints.[46]

$$\frac{\partial T_i}{\partial \theta_i} = \frac{\partial}{\partial \theta_i}\begin{bmatrix} C\theta_i & -S\theta_i C\alpha_i & -S\theta_i S\alpha_i & a_i C\theta_i \\ S\theta_i & C\theta_i C\alpha_i & -C\theta_i S\alpha_i & a_i S\theta_i \\ 0 & S\alpha_i & C\alpha_i & d_i \\ 0 & 0 & 0 & 1 \end{bmatrix} = \begin{bmatrix} -S\theta_i & -C\theta_i C\alpha_i & -C\theta_i S\alpha_i & -a_i S\theta_i \\ C\theta_i & -S\theta_i C\alpha_i & S\theta_i S\alpha_i & a_i C\theta_i \\ 0 & 0 & 0 & 0 \\ 0 & 0 & 0 & 0 \end{bmatrix} \tag{55}$$

After taking the derivative, this matrix can be written as a multiplication of the coefficient matrix which is given as Q_i and transformation matrix. This representation is given in the equation (56).

$$Q_i . T_i = \begin{bmatrix} 0 & -1 & 0 & 0 \\ 1 & 0 & 0 & 0 \\ 0 & 0 & 0 & 0 \\ 0 & 0 & 0 & 0 \end{bmatrix} \times \begin{bmatrix} C\theta_i & -S\theta_i C\alpha_i & -S\theta_i S\alpha_i & a_i C\theta_i \\ S\theta_i & C\theta_i C\alpha_i & -C\theta_i S\alpha_i & a_i S\theta_i \\ 0 & S\alpha_i & C\alpha_i & d_i \\ 0 & 0 & 0 & 1 \end{bmatrix} \tag{56}$$

Or it can be written as a symbolic version of the calculation. This symbolic version is given in the equation (57).

$$\frac{\partial T_i}{\partial \theta_i} = Q_i . T_i \triangleq U_{ij} \tag{57}$$

An arbitrary point on the links can be written as a multiplication of the transformation matrix and the vector that contains coordinate information for the point. This multiplication is used for potential energy change in terms of location variation of the center of mass which is defined with respect to link's frame and it is obtainable regarding to base frame. This phenomenon is given in the equation (58).

$$r_0^i = T_0^i . r_i^i \tag{58}$$

Dynamic equations of the 3-D 6 DOF serial manipulators are complicated and exceptionally hard to utilize. Therefore, simplifications are applied and the significance of a particular term and its contribution to the overall structure can be decided by

simulating the terms related to how large its effect. Additionally, the significance of the coriolis and centrifugal terms can be decided under the influence of velocity-related terms. Pseudo-inertia tensor should be denoted as given in equation (59).

$$J_i = \begin{bmatrix} \frac{-Ixx + Iyy + Izz}{2} & Ixy & Ixz & m_i\bar{x}_i \\ Ixy & \frac{Ixx - Iyy + Izz}{2} & Iyz & m_i\bar{y}_i \\ Ixz & Iyz & \frac{Ixx + Iyy - Izz}{2} & m_i\bar{z}_i \\ m_i\bar{x}_i & m_i\bar{y}_i & m_i\bar{z}_i & m_i \end{bmatrix} \quad (59)$$

Where Ixx, Ixy and Ixz are moments of inertia and Ixy, Ixz, and Iyz are products of the inertia matrix. $\bar{x}_i$, $\bar{y}_i$and $\bar{z}_i$ terms correspond to center of mass in related link's frame, and m_i is the mass of the link. Later on, Lagrange function is utilized in terms of inertia tensor with U_{ij} notation. This description is written in the equation (60).[46]

$$\mathcal{L} = \sum_{i=1}^{n}\sum_{j=1}^{i}\sum_{k=1}^{i} T_r(U_{ij}\, J_i U_{ik}^T)\dot{q}_i\dot{q}_k + \sum_{i=1}^{n} m_i g(T_i r_i) \quad (60)$$

Then, dynamic equations are summarized and written in a compact form which is given in the equation (61).

$$\tau_i = \sum_{k=1}^{n} D_{ik}\ddot{q}_k + \sum_{j=1}^{n}\sum_{k=1}^{n} h_{ijk}\dot{q}_j\dot{q}_k + C_i \quad (61)$$

Where D_{ik} and h_{ijk} represent the acceleration-related coefficients' matrix elements and elements of the coriolis and centrifugal terms matrix. C_i is the expression for the gravity terms. Then, all the equations can be written in a form of matrix which is given in the equation (62).

$$\tau = D(q)\ddot{q} + h(q,\dot{q}) + C(q) \quad (62)$$

First, all elements of the joint-space inertia matrix are calculated by using the equation (63).

$$D_{ik} = \sum_{j=\max(i,k)}^{n} Tr(\, U_{jk}\, J_i U_{ji}^T) \quad (63)$$

Here, D matrix is written in terms of combination of the elements and these expressions are given in the equation (64).

$$D = \begin{bmatrix} D_{11} & D_{12} & D_{31} & D_{41} & D_{51} & D_{61} \\ D_{12} & D_{22} & D_{32} & D_{42} & D_{52} & D_{62} \\ D_{13} & D_{23} & D_{33} & D_{43} & D_{53} & D_{63} \\ D_{14} & D_{24} & D_{34} & D_{44} & D_{54} & D_{64} \\ D_{15} & D_{25} & D_{35} & D_{45} & D_{55} & D_{65} \\ D_{16} & D_{26} & D_{36} & D_{46} & D_{56} & D_{66} \end{bmatrix}$$

$$D_{11} = Tr(U_{11}J_1U_{11}^T) + Tr(U_{21}J_2U_{21}^T) + Tr(U_{31}J_3U_{31}^T) + Tr(U_{41}J_4U_{41}^T) + Tr(U_{51}J_5U_{51}^T) + Tr(U_{61}J_6U_{61}^T)$$

$$D_{12} = D_{21} = Tr(U_{22}J_2U_{21}^T) + Tr(U_{32}J_3U_{31}^T) + Tr(U_{42}J_4U_{41}^T) + Tr(U_{52}J_5U_{51}^T) + Tr(U_{62}J_6U_{61}^T)$$

$$D_{13} = D_{31} = Tr(U_{33}J_3U_{31}^T) + Tr(U_{42}J_4U_{41}^T) + Tr(U_{53}J_5U_{51}^T) + Tr(U_{63}J_6U_{61}^T)$$

$$D_{14} = D_{41} = Tr(U_{44}J_4U_{41}^T) + Tr(U_{54}J_5U_{51}^T) + Tr(U_{64}J_6U_{61}^T)$$

$$D_{15} = D_{51} = Tr(U_{55}J_5U_{51}^T) + Tr(U_{65}J_6U_{61}^T)$$

$$D_{16} = D_{61} = Tr(U_{66}J_6U_{61}^T) \quad (64)$$

$$D_{22} = Tr(U_{22}J_2U_{22}^T) + Tr(U_{32}J_3U_{32}^T) + Tr(U_{42}J_4U_{42}^T) + Tr(U_{52}J_5U_{52}^T) + Tr(U_{62}J_6U_{62}^T)$$

$$D_{23} = D_{32} = Tr(U_{33}J_3U_{32}^T) + Tr(U_{43}J_4U_{42}^T) + Tr(U_{53}J_5U_{52}^T) + Tr(U_{63}J_6U_{62}^T)$$

$$D_{24} = D_{42} = Tr(U_{44}J_4U_{42}^T) + Tr(U_{54}J_5U_{52}^T) + Tr(U_{64}J_6U_{62}^T)$$

$$D_{25} = D_{52} = Tr(U_{55}J_5U_{52}^T) + Tr(U_{65}J_6U_{62}^T)$$

$$D_{26} = D_{62} = Tr(U_{66}J_6U_{62}^T)$$

$$D_{33} = Tr(U_{33}J_3U_{33}^T) + Tr(U_{43}J_4U_{43}^T) + Tr(U_{53}J_5U_{53}^T) + Tr(U_{63}J_6U_{63}^T)$$

$$D_{34} = D_{43} = Tr(U_{44}J_4U_{43}^T) + Tr(U_{54}J_5U_{53}^T) + Tr(U_{64}J_6U_{63}^T)$$

$$D_{35} = D_{53} = Tr(U_{55}J_5U_{53}^T) + Tr(U_{65}J_5U_{63}^T)$$

$$D_{36} = D_{63} = Tr(U_{66}J_6U_{63}^T)$$

$$D_{44} = Tr(U_{44}J_4U_{44}^T) + Tr(U_{54}J_5U_{54}^T) + Tr(U_{64}J_6U_{64}^T)$$

$$D_{45} = D_{54} = Tr(U_{55}J_5U_{54}^T) + Tr(U_{65}J_6U_{64}^T)$$

$$D_{46} = D_{64} = Tr(U_{66}J_6U_{64}^T)$$

$$D_{55} = Tr(U_{55}J_5U_{55}^T) + Tr(U_{65}J_6U_{65}^T)$$

$$D_{56} = D_{65} = Tr(U_{66}J_6U_{65}^T)$$

$$D_{66} = Tr(U_{66}J_6U_{66}^T)$$

After deriving all elements of the acceleration related terms from the expression in equation (64), acceleration related terms' matrix is completed. It is important to highlight that acceleration related terms' matrix is derived in joint space. Then, matrix is defined to find coriolis and centrifugal effects due to relative joint motions. All elements of the coriolis matrix are defined with respect to first joint which contains the influence of the velocity regarding first link. 6×6 matrix is defined and derivations are explained in the following for general formulation is represented by equation (65).

$$H_i = \begin{bmatrix} h_{i11} & h_{i12} & h_{i13} & h_{i14} & h_{i15} & h_{i16} \\ h_{i12} & h_{i22} & h_{i23} & h_{i24} & h_{i25} & h_{i26} \\ h_{i13} & h_{i23} & h_{i33} & h_{i34} & h_{i35} & h_{i36} \\ h_{i14} & h_{i24} & h_{i34} & h_{i44} & h_{i45} & h_{i46} \\ h_{i15} & h_{i25} & h_{i35} & h_{i45} & h_{i55} & h_{i56} \\ h_{i16} & h_{i26} & h_{i36} & h_{i46} & h_{i56} & h_{i66} \end{bmatrix} \tag{65}$$

Then, representative derivation is completed for the first link and the matrix form of the first link is expressed by using the matrix in equation (66).

$$H_1 = \begin{bmatrix} h_{111} & h_{112} & h_{113} & h_{114} & h_{115} & h_{116} \\ h_{112} & h_{122} & h_{123} & h_{124} & h_{125} & h_{126} \\ h_{113} & h_{123} & h_{133} & h_{134} & h_{135} & h_{136} \\ h_{114} & h_{124} & h_{134} & h_{144} & h_{145} & h_{146} \\ h_{115} & h_{125} & h_{135} & h_{145} & h_{155} & h_{156} \\ h_{116} & h_{126} & h_{136} & h_{146} & h_{156} & h_{166} \end{bmatrix} \tag{66}$$

For mass matrix, pseudo-inertia tensor and U_{ij} notation, which defines the effect of joint j on the link i. However, to be able to calculate the elements of the coriolis and centrifugal matrix, the third equation category, which describes the torques and velocity related terms induced by other subsequent joints, is needed. For that purpose, U_{ijk} notation is used, and necessary description is given in the equation (67). [46]

$$\frac{\partial U_{ij}}{\partial \theta_k} \triangleq U_{ijk} = \begin{cases} T_0^{j-1} Q_j T_{j-1}^{k-1} Q_k T_{k-1}^{i} & i \geq k \geq j \\ T_0^{k-1} Q_k T_{k-1}^{j-1} Q_j T_{j-1}^{i} & i \geq j \geq k \\ 0 & i < j \; or \; i < k \end{cases} \tag{67}$$

Where U_{ij} is the notation for the differentiation of the transformation matrix in terms of symbolic representation and multiplication of the transformation matrices, and necessary derivations are expressed for U_{ijk} (see Appendix C). After finding the U_{ijk}, h_i and h_{ikm} are written in the equation (68).

$$\begin{aligned} h_i &= \sum_{k=1}^{n} \sum_{m=1}^{n} h_{ikm} \dot{q}_k \dot{q}_m \qquad\qquad i = 1,2, \dots\dots\dots\dots, n \\ h_{ikm} &= \sum_{j=\max(i,k,m)}^{n} Tr\left(U_{jkm} \, J_j \, U_{ji}^T\right) \qquad\qquad i,k,m = 1,2, \dots\dots\dots\dots, n \end{aligned} \tag{68}$$

Derivation of the h_{111} is explained by using equation (68). Necessary derivation procedure is given in the equation (69).

$$\begin{aligned} h_{111} &= Tr\,(U_{111} J_1 U_{11}^T) + Tr(U_{211} J_2 U_{21}^T) + Tr(U_{311} J_3 U_{31}^T) + \\ &Tr(U_{411} J_4 U_{41}^T) + Tr(U_{511} J_5 U_{51}^T) + Tr(U_{611} J_6 U_{61}^T) \\ h_{112} &= Tr\,(U_{212} J_2 U_{21}^T) + Tr(U_{312} J_3 U_{31}^T) + Tr(U_{412} J_4 U_{41}^T) + \\ &Tr(U_{512} J_5 U_{51}^T) + Tr(U_{612} J_6 U_{61}^T) \\ h_{113} &= Tr\,(U_{313} J_3 U_{31}^T) + Tr(U_{413} J_4 U_{41}^T) + Tr(U_{513} J_5 U_{51}^T) + \\ &Tr(U_{613} J_6 U_{61}^T) \\ h_{114} &= Tr\,(U_{414} J_4 U_{41}^T) + Tr(U_{514} J_5 U_{51}^T) + Tr(U_{614} J_6 U_{61}^T) \\ h_{115} &= Tr\,(U_{515} J_5 U_{51}^T) + Tr(U_{615} J_6 U_{61}^T) \\ h_{116} &= Tr\,(U_{616} J_6 U_{61}^T) \end{aligned} \tag{69}$$

By using the equation (69), first row and column of the coriolis and centrifugal terms matrix are established and shown in equation (70) as a blue painted part of the matrix.

$$H_1 = \begin{bmatrix} h_{111} & h_{112} & h_{113} & h_{114} & h_{115} & h_{116} \\ h_{112} & h_{122} & h_{123} & h_{124} & h_{125} & h_{126} \\ h_{113} & h_{123} & h_{133} & h_{134} & h_{135} & h_{136} \\ h_{114} & h_{124} & h_{134} & h_{144} & h_{145} & h_{146} \\ h_{115} & h_{125} & h_{135} & h_{145} & h_{155} & h_{156} \\ h_{116} & h_{126} & h_{136} & h_{146} & h_{156} & h_{166} \end{bmatrix} \tag{70}$$

Then, derivations are completed by starting h_{i22} as given in the equation (71).

$$\begin{aligned} h_{122} &= Tr\left(U_{222}\, J_2 U_{21}^T\right) + Tr(U_{322}\, J_3 U_{31}^T) + Tr(U_{422}\, J_4 U_{41}^T) + \\ &Tr(U_{522}\, J_5 U_{51}^T) + Tr(U_{622}\, J_6 U_{61}^T) \\ h_{123} &= Tr\left(U_{323}\, J_3 U_{31}^T\right) + Tr(U_{423}\, J_4 U_{41}^T) + Tr(U_{523}\, J_5 U_{51}^T) + \\ &Tr(U_{623}\, J_6 U_{61}^T) \\ h_{124} &= Tr\left(U_{424}\, J_4 U_{41}^T\right) + Tr(U_{524}\, J_5 U_{51}^T) + Tr(U_{624}\, J_6 U_{61}^T) \\ h_{125} &= Tr\left(U_{525}\, J_5 U_{51}^T\right) + Tr(U_{625}\, J_6 U_{61}^T) \\ h_{126} &= Tr\left(U_{626}\, J_6 U_{61}^T\right) \end{aligned} \tag{71}$$

By using the equation (71), second row and column of the Coriolis and centrifugal terms matrix are established and shown in equation (72).

$$H_1 = \begin{bmatrix} h_{111} & h_{112} & h_{113} & h_{114} & h_{115} & h_{116} \\ h_{112} & h_{122} & h_{123} & h_{124} & h_{125} & h_{126} \\ h_{113} & h_{123} & h_{133} & h_{134} & h_{135} & h_{136} \\ h_{114} & h_{124} & h_{134} & h_{144} & h_{145} & h_{146} \\ h_{115} & h_{125} & h_{135} & h_{145} & h_{155} & h_{156} \\ h_{116} & h_{126} & h_{136} & h_{146} & h_{156} & h_{166} \end{bmatrix} \tag{72}$$

Obtained row and columns are indicated with a red paint. Then, third row and column are created in equation (73).

$$\begin{aligned} h_{133} &= Tr\left(U_{333}\, J_3 U_{31}^T\right) + Tr(U_{433}\, J_4 U_{41}^T) + Tr(U_{533}\, J_5 U_{51}^T) + \\ &Tr(U_{633}\, J_6 U_{61}^T) \\ h_{134} &= Tr\left(U_{434}\, J_4 U_{41}^T\right) + Tr(U_{534}\, J_5 U_{51}^T) + Tr(U_{634}\, J_6 U_{61}^T) \\ h_{135} &= Tr\left(U_{535}\, J_5 U_{51}^T\right) + Tr(U_{635}\, J_6 U_{61}^T) \\ h_{136} &= Tr\left(U_{636}\, J_6 U_{61}^T\right) \end{aligned} \tag{73}$$

As a result of the third row and column generation, green painted elements are obtained and shown in equation (74) in a matrix form.

$$H_1 = \begin{bmatrix} h_{111} & h_{112} & h_{113} & h_{114} & h_{115} & h_{116} \\ h_{112} & h_{122} & h_{123} & h_{124} & h_{125} & h_{126} \\ h_{113} & h_{123} & h_{133} & h_{134} & h_{135} & h_{136} \\ h_{114} & h_{124} & h_{134} & h_{144} & h_{145} & h_{146} \\ h_{115} & h_{125} & h_{135} & h_{145} & h_{155} & h_{156} \\ h_{116} & h_{126} & h_{136} & h_{146} & h_{156} & h_{166} \end{bmatrix} \quad (74)$$

Obtained row and columns for third h_{i33} are given in the equation (74) as a green painted area. Then, fourth row and column are generated for h_{i44} and given in the equation (75).

$$\begin{aligned} h_{144} &= Tr\,(U_{444}\,J_4 U_{41}^T) + Tr(U_{544}\,J_5 U_{51}^T) + Tr(U_{644}\,J_6 U_{61}^T) \\ h_{145} &= Tr\,(U_{545}\,J_5 U_{51}^T) + Tr(U_{645}\,J_6 U_{61}^T) \\ h_{146} &= Tr\,(U_{646}\,J_6 U_{61}^T) \end{aligned} \quad (75)$$

After obtained the row and columns for the part of the h_{i44}, matrix establishment is progressed through the last rows and columns part of the h_{i55} and h_{i66}.

$$H_1 = \begin{bmatrix} h_{111} & h_{112} & h_{113} & h_{114} & h_{115} & h_{116} \\ h_{112} & h_{122} & h_{123} & h_{124} & h_{125} & h_{126} \\ h_{113} & h_{123} & h_{133} & h_{134} & h_{135} & h_{136} \\ h_{114} & h_{124} & h_{134} & h_{144} & h_{145} & h_{146} \\ h_{115} & h_{125} & h_{135} & h_{145} & h_{155} & h_{156} \\ h_{116} & h_{126} & h_{136} & h_{146} & h_{156} & h_{166} \end{bmatrix} \quad (76)$$

Elements of the h_{i44} are painted to orange for identification of the sequential progress of the equation (75). Then, fifth row and column elements' equations are derived and shown in equation (77) for h_{i55}.

$$\begin{aligned} h_{155} &= Tr\,(U_{555}\,J_5 U_{51}^T) + Tr(U_{655}\,J_6 U_{61}^T) \\ h_{156} &= Tr(U_{656}\,J_6 U_{61}^T) \end{aligned} \quad (77)$$

After obtaining the rows and columns for h_{i55}, it is painted to purple for its matrix representation in equation (78).

$$H_1 = \begin{bmatrix} h_{111} & h_{112} & h_{113} & h_{114} & h_{115} & h_{116} \\ h_{112} & h_{122} & h_{123} & h_{124} & h_{125} & h_{126} \\ h_{113} & h_{123} & h_{133} & h_{134} & h_{135} & h_{136} \\ h_{114} & h_{124} & h_{134} & h_{144} & h_{145} & h_{146} \\ h_{115} & h_{125} & h_{135} & h_{145} & h_{155} & h_{156} \\ h_{116} & h_{126} & h_{136} & h_{146} & h_{156} & h_{166} \end{bmatrix} \quad (78)$$

Finally, equations for the first link is completed with the last element of the matrix which is given as h_{i66} in a general form and h_{166} for the equation utilization of the first link. Necessary equation block is given in the equation (79).

$$h_{166} = Tr\,(U_{666}\,J_6 U_{61}^T) \tag{79}$$

Then, matrix establishment is achieved for the first link in terms of coriolis and centrifugal terms. This matrix representation is given in the equation (80) as a gray painted element.

$$H_1 = \begin{bmatrix} h_{111} & h_{112} & h_{113} & h_{114} & h_{115} & h_{116} \\ h_{112} & h_{122} & h_{123} & h_{124} & h_{125} & h_{126} \\ h_{113} & h_{123} & h_{133} & h_{134} & h_{135} & h_{136} \\ h_{114} & h_{124} & h_{134} & h_{144} & h_{145} & h_{146} \\ h_{115} & h_{125} & h_{135} & h_{145} & h_{155} & h_{156} \\ h_{116} & h_{126} & h_{136} & h_{146} & h_{156} & h_{166} \end{bmatrix} \tag{80}$$

After obtaining all elements for the first link, same procedure is applied for all the links. It is followed by the joint velocities which are given in the form of the matrix as shown in equation (81) as a 6×1 matrix.

$$\dot{\theta}(t) = \left[\dot{\theta}_1(t), \dot{\theta}_2(t), \dot{\theta}_3(t), \dot{\theta}_4(t), \dot{\theta}_5(t), \dot{\theta}_6(t)\right] \tag{81}$$

After giving joint velocities, coriolis and centrifugal matrix is obtained in the equation (82).

$$h_i = \dot{\theta}^T H_i \dot{\theta}$$

$$h(\theta, \dot{\theta}) = \begin{bmatrix} h_1 \\ h_2 \\ h_3 \\ h_4 \\ h_5 \\ h_6 \end{bmatrix} = \begin{bmatrix} \dot{\theta}^T H_1 \dot{\theta} \\ \dot{\theta}^T H_2 \dot{\theta} \\ \dot{\theta}^T H_3 \dot{\theta} \\ \dot{\theta}^T H_4 \dot{\theta} \\ \dot{\theta}^T H_5 \dot{\theta} \\ \dot{\theta}^T H_6 \dot{\theta} \end{bmatrix} \tag{82}$$

As a result of the equation (82), multi-dimensional matrix should be created to express coriolis and centrifugal terms for all links. This phenomenon creates $6 \times 6 \times 6$ matrix in the form of multi-dimension. Third and finally, gravitational terms are established in the form of the 6×1 vector. Followed procedure and necessary equations are given in the equation (83) as a last part of the dynamics of the industrial robot which has 6 axes.

$$c_1 = -\left(m_1 g U_{11} \bar{r}_1^1 + m_2 g U_{21} \bar{r}_2^2 + m_3 g U_{31} \bar{r}_3^3 + m_4 g U_{41} \bar{r}_4^4 + m_5 g U_{51} \bar{r}_5^5 + m_6 g U_{61} \bar{r}_6^6\right)$$

$$c_2 = -\left(m_2 g U_{22} \bar{r}_2^2 + m_3 g U_{32} \bar{r}_3^3 + m_4 g U_{42} \bar{r}_4^4 + m_5 g U_{52} \bar{r}_5^5 + m_6 g U_{62} \bar{r}_6^6\right)$$

$$c_3 = -\left(m_3 g U_{33} \bar{r}_3^3 + m_4 g U_{43} \bar{r}_4^4 + m_5 g U_{53} \bar{r}_5^5 + m_6 g U_{63} \bar{r}_6^6\right) \quad (83)$$

$$c_4 = -\left(m_4 g U_{44} \bar{r}_4^4 + m_5 g U_{54} \bar{r}_5^5 + m_6 g U_{64} \bar{r}_6^6\right)$$

$$c_5 = -\left(m_5 g U_{55} \bar{r}_5^5 + m_6 g U_{65} \bar{r}_6^6\right)$$

$$c_6 = -\left(m_6 g U_{66} \bar{r}_6^6\right)$$

$$c(\theta) = [c_1, c_2, c_3, c_4, c_5, c_6]^T$$

After obtaining the equations for the mass, coriolis and centrifugal terms and gravitational terms, all terms are replaced into equation (62). These terms can be explained as a function of inertia parameters and joint variables. Physical interpretation of these dynamic terms is given in the following list.

- c_i is the gravitational load terms due to mass of the links dependent on the joint configuration.
- D_{ik} is related to acceleration of the joints and related torques where the driving torques affect joint i for D_{ii} and, D_{ik} is related to induced torque on the joint i due to the motion of joint k.
- h_{ikm} is related to joint velocity and $k$and m indices are related to subsequent joint velocities which affect the joint i in terms of torque formation due to velocity term effects. However, in case of $k = m$, torque is obtained as a result of centrifugal forces. In other case, $k \neq m$, Coriolis effect creates torque on joint i.

Equations of motion are expressed as a non-linear second order ordinary differential equations. These equations explain effects of inertia, centrifugal, coriolis and gravitational terms on the links. Torque values depend on effects of these terms based on joint position, velocity and acceleration.

2.2.4.1 Robot dynamics in cartesian space and identification procedure for natural frequencies / Linearized robot dynamics

Robot dynamics' equations are derived and investigated in joint space. However, identification of the natural frequencies requires cartesian space dynamics. Therefore, dynamic terms in the joint space are converted into cartesian space. To achieve this conversation, jacobian of the robot structure is used and end-effector dynamics in cartesian space are obtained. Acceleration related terms' matrix is converted from joint space to cartesian space with the equation (84).

$$\widetilde{D} = (J^{-1})^T D(q) J^{-1} \tag{84}$$

Then, general characteristic equation of the motion is written in the equation (85) to start identification of the natural frequencies of the robot structure. For that purpose, identification procedure is explained through equations and then representative case is given with respect to variation of the joint positions. The characteristic equation of motion is given in the equation (85).

$$[\boldsymbol{M}]\{\ddot{\boldsymbol{x}}\} + [\boldsymbol{C}]\{\dot{\boldsymbol{x}}\} + [\boldsymbol{K}]\{\boldsymbol{x}\} = \{\boldsymbol{F}\} \tag{85}$$

In equation (85), [M], [C], and [K] matrices are defined as mass, damping, and stiffness matrix as 6x6 matrices. {F} is the vector that contains applied forces where {x} is defined as position and orientation vector. For the sake of simplification, and damping has the pure effect to increase stability, important parts of the characteristic equation of motion are mass matrix and stiffness matrix. In such a manner, equation (85) is written by canceling out the damping effect and it is converted into equation (86).

$$[\boldsymbol{D}]\{\ddot{\boldsymbol{x}}\} + [\boldsymbol{K}]\{\boldsymbol{x}\} = \{\boldsymbol{F}\} \tag{86}$$

Salisbury et al.[54] proposed a basic joint stiffness matrix. This matrix depends on jacobian and joint stiffness matrix which is given in the equation (87).

$$K_\theta = JKJ^T \tag{87}$$

Klimchik et al.[56] proposed partial pose measurement data to identify joint stiffness values based on measured translational movements without orientation part of the pose. Theissen et al.[55] used partial pose measurement to identify joint stiffness with identified quantities (Δx and M) and linear-least square optimization approach used with respect to objective function that is defined in the equation (88).

$$\left\| K_{\theta j}^{-1} M_{ij} - \Delta_{x,ij} \right\|_2^2 \tag{88}$$

Where M_{ij} matrix correlates the differential motions in cartesian space regarding variation in joint angles with torque around principal axes. Dumas et al.[3] proposed a systematic methodology to identify joint stiffnesses for KUKA KR240-2 industrial robot and stiffness matrix is given in the equation (89).

$$K_\theta = \begin{bmatrix} 3.8*10^6 & 0 & 0 & 0 & 0 & 0 \\ 0 & 6.6*10^6 & 0 & 0 & 0 & 0 \\ 0 & 0 & 3.9*10^6 & 0 & 0 & 0 \\ 0 & 0 & 0 & 5.6*10^5 & 0 & 0 \\ 0 & 0 & 0 & 0 & 6.6*10^5 & 0 \\ 0 & 0 & 0 & 0 & 0 & 4.7*10^5 \end{bmatrix} \tag{89}$$

Then, joint stiffness in joint space converted into cartesian space by using jacobian, which is found by perturbation methodology, in the equation (90).

$$\boldsymbol{K = \left[J(q)^T K_q^{-1} J(q) \right]^{-1}} \tag{90}$$

After obtaining stiffness matrix in cartesian space, base frequencies are obtainable with respect to jacobian and mass matrix in cartesian space. The characteristic equation is written in terms of homogeneous solution without any external force. This representation is given in the equation (91).

$$\boldsymbol{\det([K] - [D]\lambda^2) = 0} \tag{91}$$

By equating the result of the determinant to zero, angular frequency is obtained. These frequencies are highly dependent on the joint configuration. Furthermore, natural frequencies are obtained as given in the equation (92).

$$f = \frac{\lambda}{2\pi} \tag{92}$$

The model enables to predict six dominant frequencies when joint configuration of the robot is known. The robot's kinematic and dynamic models are simulated in the MATLAB©. This representation is given in the Figure 2-12.

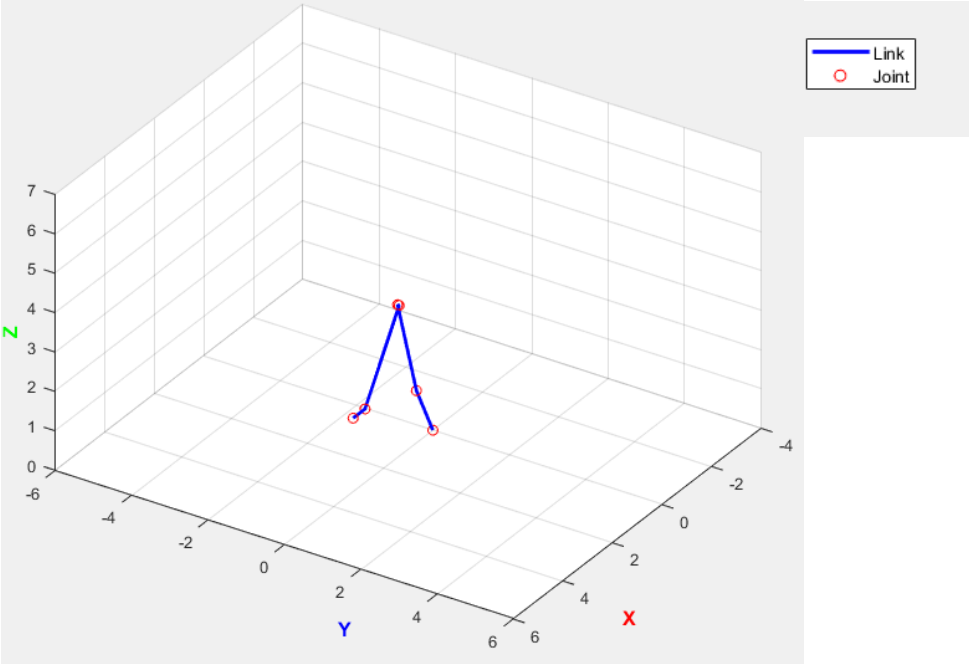

Figure 2-12: KUKA KR 240 R2900 representation

Joints are represented by red circles and links are represented by blue lines. This representation is used for better understanding of variation in the dynamic properties when it is simulated for given trajectory based on kinematics. Allowable joint positions are taken from manufacturer specifications and limitations are given in the Table 2-3.

A1	+- 185°
A2	-140°/-5°
A3	-120°/155°
A4	+- 350°
A5	+-122.5°
A6	+-350°

Table 2-3: Motion constraints for the axes of KUKA KR 240 R2900

T shape trajectory is used to measure robot's strucutural vibration characteristics. 11 points are determined for FRF measurements. According to determined points on the robot structure, FRFs are measured with respect to 5 different postures. Related joint positions are given in the Table 2-4. Experimental study on FRF measurement is given in the Appendix D.

A1	-1.0750°	-1.2155°	-1.3948°	-1.6345°	-1.9728°
A2	-30.9331°	-43.9551°	-54.27°	-63.58°	-72.70°
A3	47.65°	73.50°	93.23°	110.15°	125.40°
A4	-4°	-2.5°	-2.2°	-2.3°	-2.5°
A5	-16.78°	-29.57°	-38.98°	-46.59°	-52.73°
A6	3.9452°	2.2803°	1.8195°	1.6345°	1.9728°

Table 2-4: Joint positions regarding experimental FRF positions (see Appendix D)

The actual movement of the robot was simulated in MATLAB© based on related joint configurations. Simulations in MATLAB© and NX© are given for the pose 1 and pose 2 in the Figure 2-13 (a)- (b) and (c)-(d), respectively.

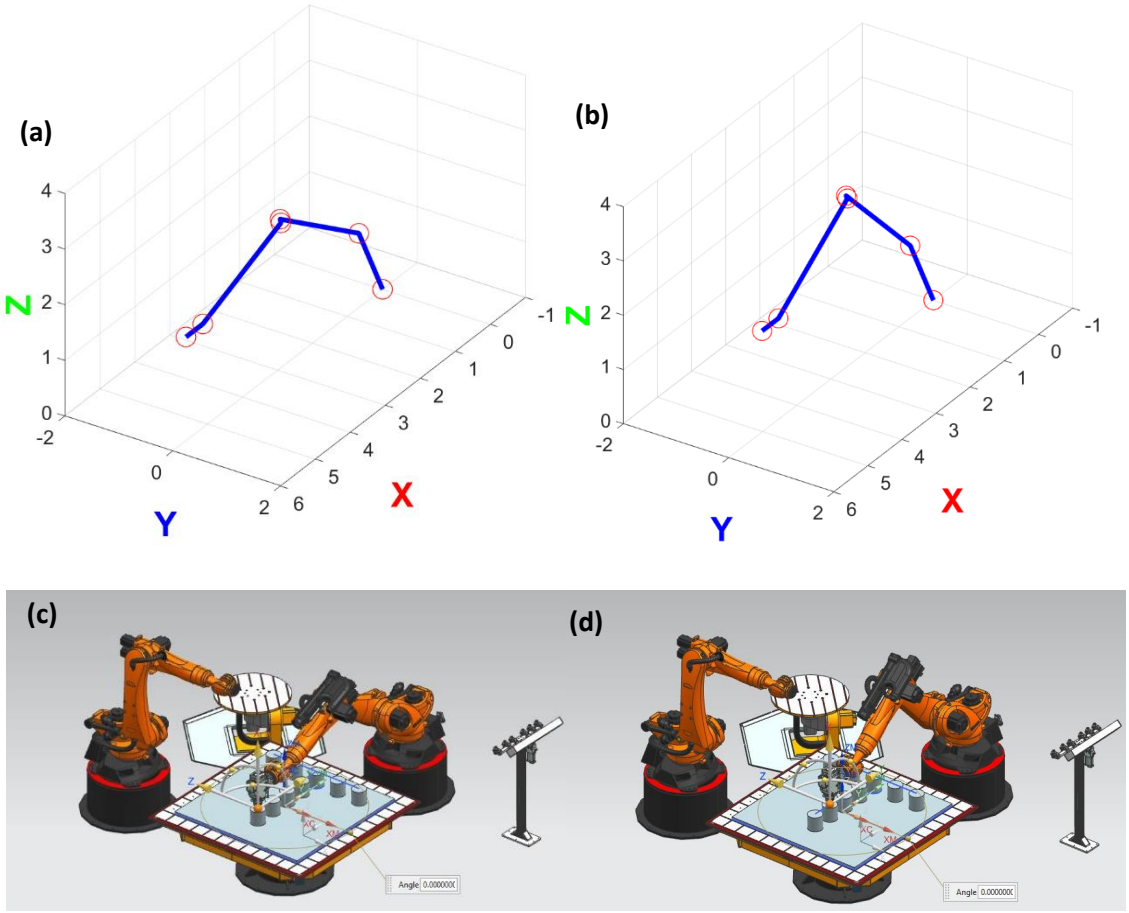

Figure 2-13: MATLAB© and NX© simulations for different postures of the robot (a)pose 1-MATLAB© (b) pose 1-NX© (c) pose 2-MATLAB© (d) pose 2-NX©

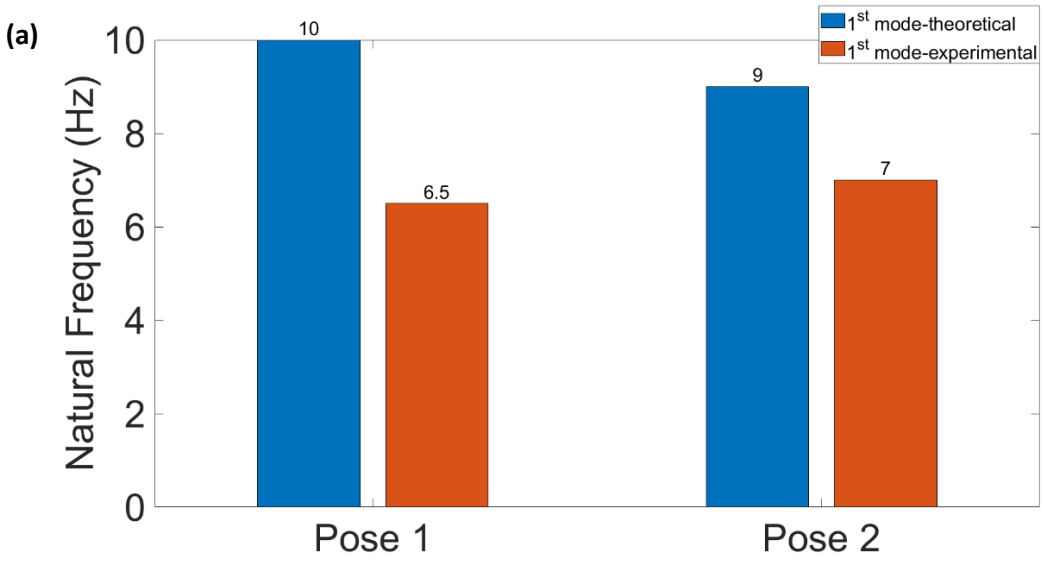

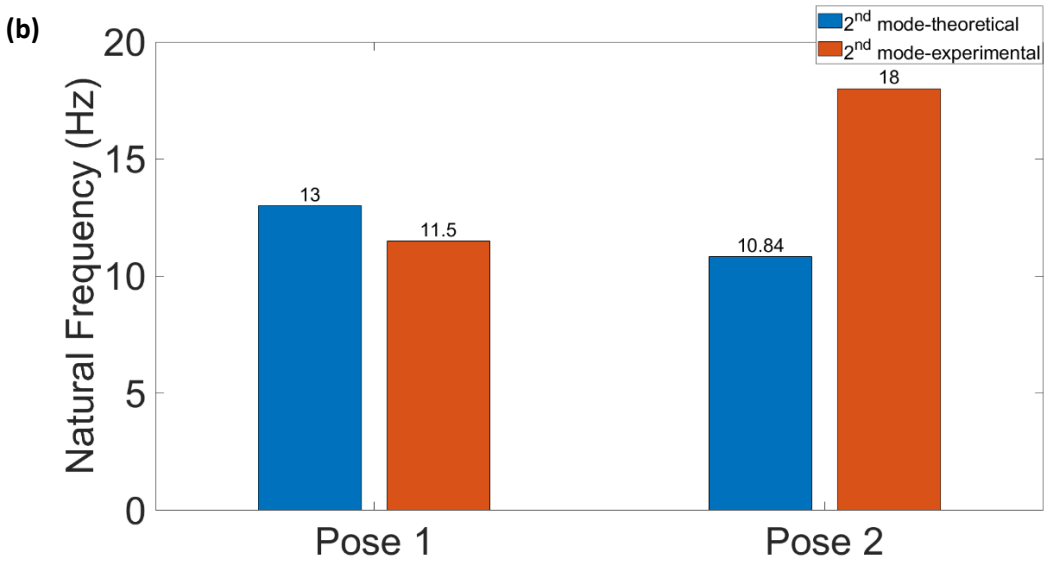

Figure 2-14: Experimental and theoretical natural frequencies of pose 1 and pose 2 (a)1st mode, (b) 2nd mode

Natural frequencies of the 1st mode and 2nd mode are shown in Figure 2-14(a)-(b) for pose 1 and pose 2, respectively. The lowest frequency is measured around 6.5 Hz where the robot is stretched to reach 2.885 m in the X direction with respect to the base frame. When the end effector of the robot moved towards its base, measured 1st mode of the robot is shifted from starting 6.5 Hz to 7 Hz and 2nd modes are observed around 11.5 Hz and 18 Hz regarding pose 1 and pose 2, respectively. Besides FRF measurements, theoretical calculations are used to identify natural frequencies and 1st mode's natural frequencies are identified as 10 Hz and 9 Hz, and 2nd mode's natural frequencies are calculated as 13 Hz and 10.84 Hz. Computed frequencies are close to experimental modal analysis results. However, deviations are observed, and error percentages are calculated to distinguish the deviation differences regarding the same posture. The most deviated mode is observed in the first posture of the robot. Calculated errors are around 35% and 22% for the 1st mode with respect to the first posture of the robot. Then, errors were observed around 11% and 66% for the 2nd mode's natural frequency comparisons. Simulations in MATLAB© and NX© are given for the pose 3 and pose 4 in the Figure 2-15 (a)- (b) and (c)-(d), respectively.

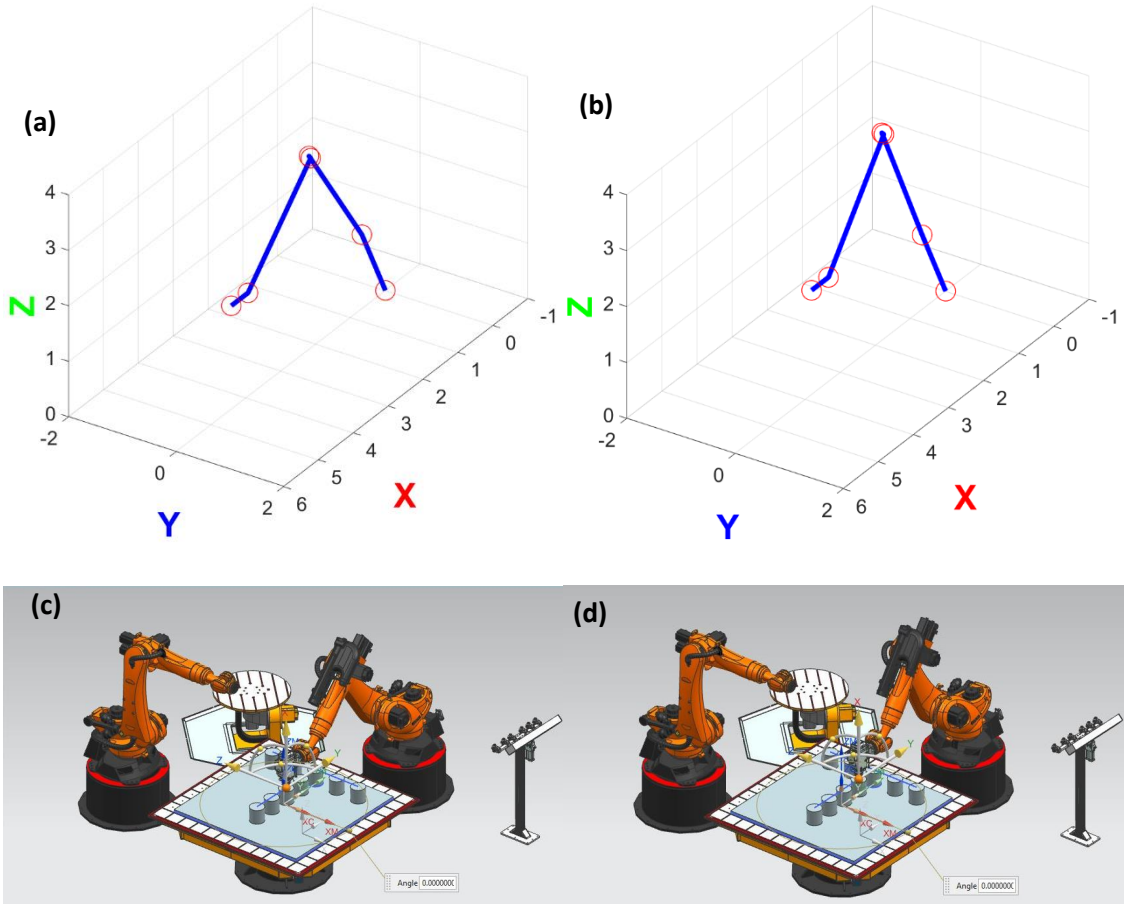

Figure 2-15: MATLAB© and NX© simulations for different postures of the robot (a)pose 3-MATLAB© (b) pose 3-NX© (c) pose 4-MATLAB© (d) pose 4-NX©

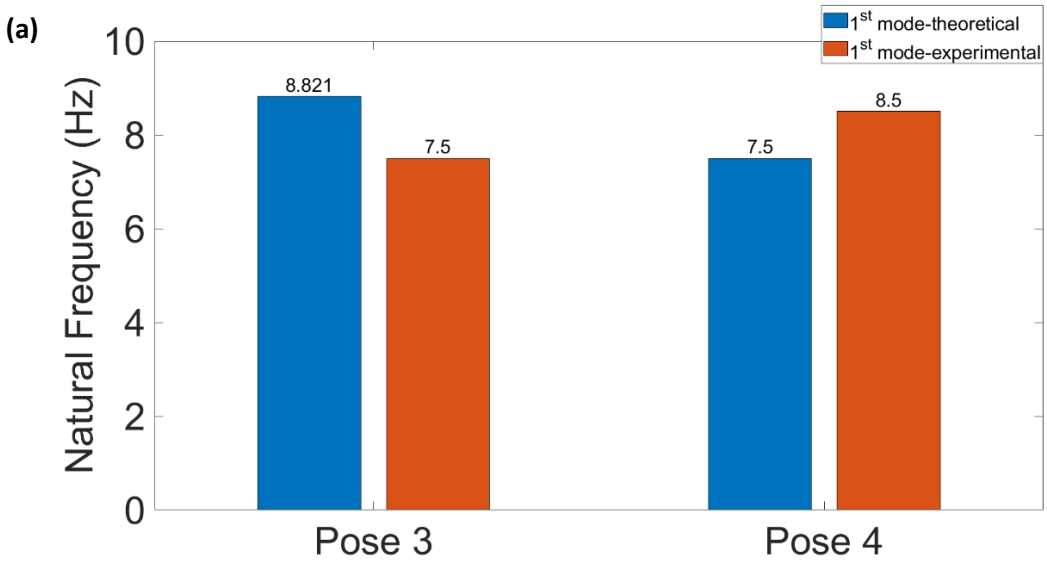

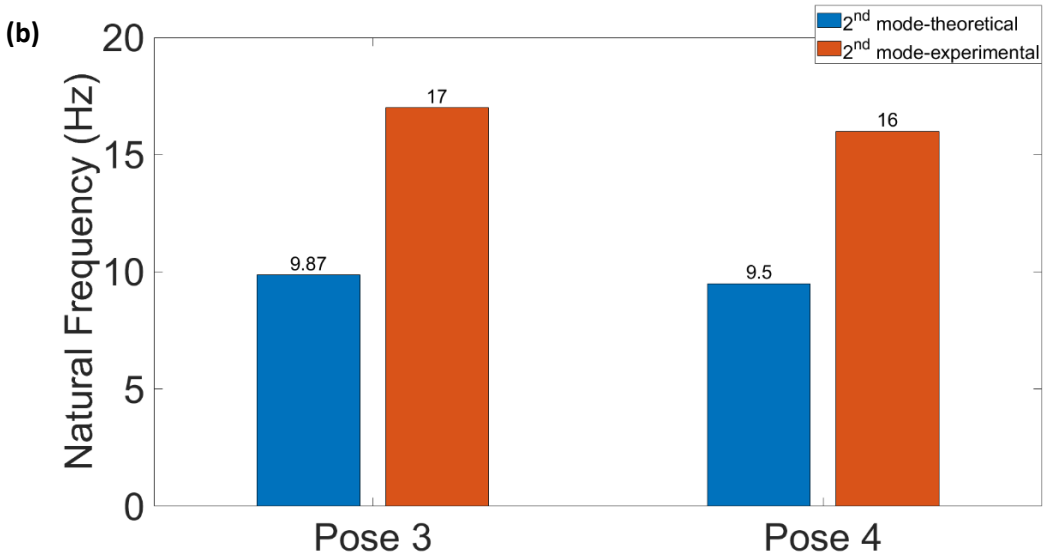

Figure 2-16: Experimental and theoretical natural frequencies of pose 3 and pose 4 (a)1st mode, (b) 2nd mode

Natural frequencies of the 1st mode and 2nd mode are shown in Figure 2-16(a)-(b) for pose 3 and pose 4, respectively. According to modal analysis results, natural frequencies are observed around 7.5 Hz and 8.5 Hz for pose 3 and pose 4, respectively. 17 Hz and 16 Hz are identified as 2nd mode's natural frequencies from modal analysis results for pose 3 and pose 4, respectively. Next, theoretical frequencies are calculated for 1st mode and frequencies are found as 8.821 Hz and 7.5 Hz for pose 3 and 4, respectively. 2nd modes are calculated as 9.87 Hz and 9.5 Hz. Larger deviations are observed for 2nd modes. 15% and 13% errors are calculated for 1st mode of pose 3 and pose 4, respectively. However, error percentages are increased compared to 2nd modes of the pose 1 and pose 2 and observed around 72% and 68%. Then, evaluations are completed for the last posture of the robot. Simulations in MATLAB© and NX© are given for the last posture of the robot, pose 5, in the Figure 2-15 (a)- (b), respectively.

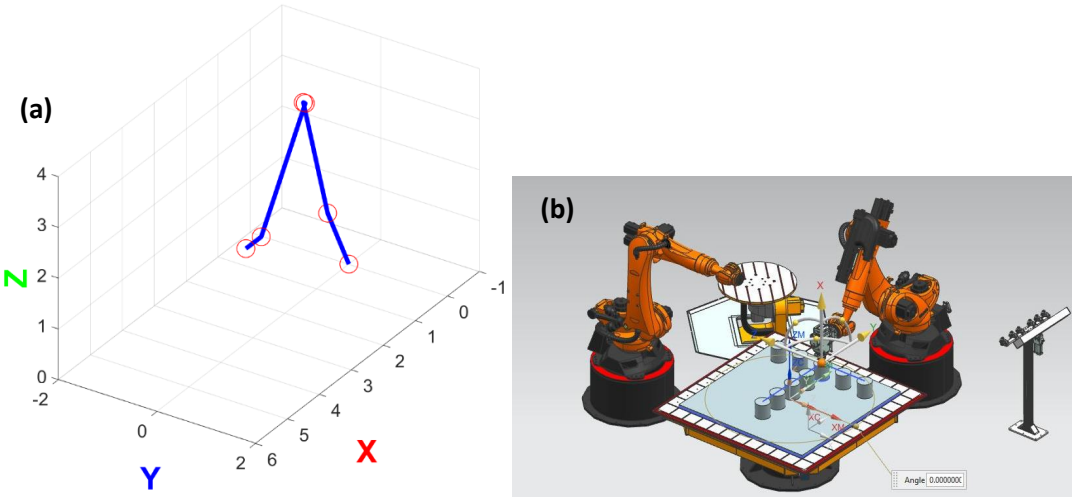

Figure 2-17: MATLAB© and NX© simulations for the last posture of the robot (a)pose 5-MATLAB© (b) pose 5-NX©

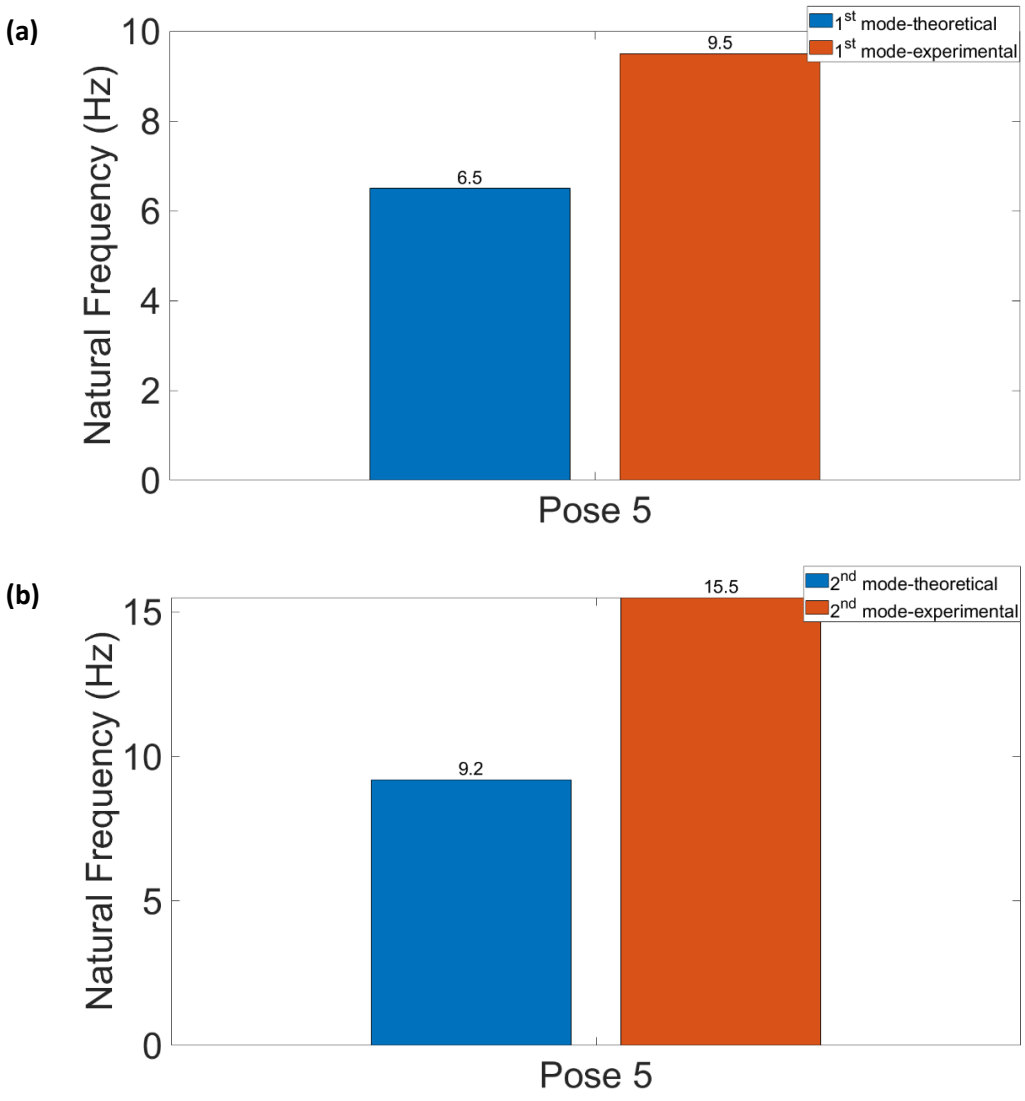

Figure 2-18: Experimental and theoretical natural frequencies of pose 5

Natural frequencies of the 1st mode and 2nd mode are shown in Figure 2-18(a)-(b) for pose 5, respectively. At the last pose of the robot, 1st mode's natural frequencies are identified as 9.5 Hz and 6.5 Hz, respectively. 15.5 Hz and 9.5 Hz are found for 2nd mode's natural frequency of pose 5. Increasing trend is observed for 1st mode while robot was moving from its strecthed form towards folding form of the arms in terms of experimental modal analysis. However, theoretical trend deviated at the beginning, merged in the middle and deviated towards the end of the posture. A spike is observed when the robot moved from pose 1 to pose 2 in terms of natural frequencies of the 2nd modes. Then, increasing trend is observed from pose 2 to pose 5 in terms of experimental analysis as well as theoretical calculations with lower values. One of the possible error sources is using CAD data ,which can give rough estimation due to exterior shape of the robot model, for mass and inertia properties with center of mass coordinates. Another possible source of error might be inaccuracies in FRF measurements. Therefore, identification of the dynamic parameters is required and extensive FRF measurements with more points on the robot structure should be performed.

2.3 Summary

In this chapter, robot dynamics are investigated through simulations by using inverse dynamics models namely Recursive Newton-Euler and Lagrangian approach. Later on, computation time comparisons are added to distinguish the normal algorithms and parallel algorithms for 2 DOF planar serial robot mechanisms with verification of the different equation structure results. Another systematic robot dynamics' formulation is derived to model 3-D 6-axis industrial robots and its implementation for KUKA KR 240 R2900 is given. Finally, natural frequency identification is established and compared to experimental results.

CHAPTER 3: Robotic Milling Dynamics

The experimental modal analysis method is based on a real object, which avoids the complexity to describe the flexibility of the arm and joint using the mathematical model. Based on the method, the parameters that reflect the dynamic characteristics of the robot can be obtained more accurately. Therefore, steps for the hammer impact tests and modal analysis are followed and schematized in Figure 3-1.

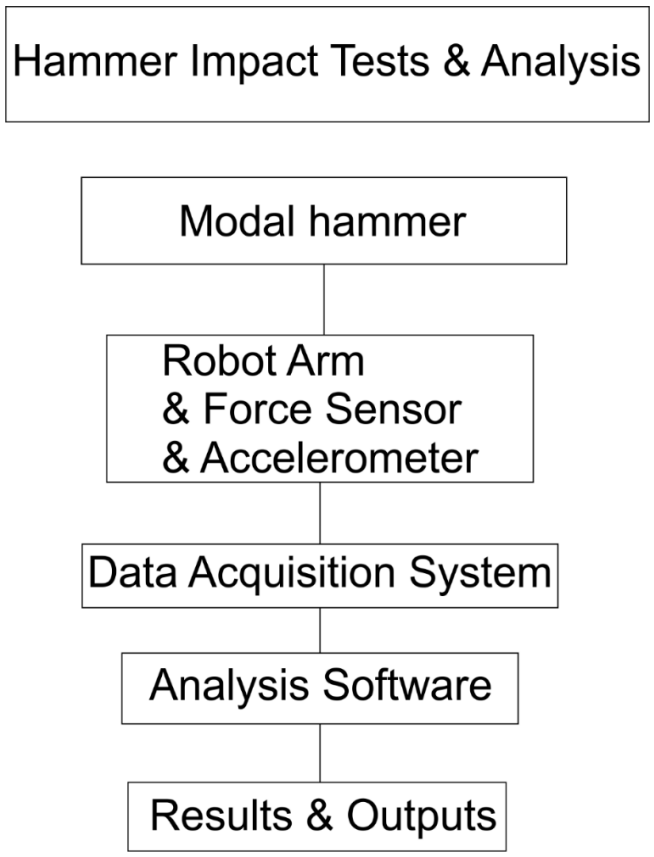

Figure 3-1: Hammer impact test steps

Impact hammer test setup consists of a modal hammer, accelerometer, data acquisition system, and analysis software. A mechanical system should be excited with a force, input signal, and output of the system can be measured as a displacement or acceleration with an accelerometer. Data acquisition systems should be used in order to collect, store, and transfer the data to the software. Then, the frequency response function is obtained and it is abbreviated as FRF. FRF expresses the relation between the given input and the

obtained output. Natural frequencies existence is represented by the peaks and natural frequencies with modal parameters (such as damping, modal stiffness, and modal mass) can be determined. To obtain reliable data, impact hammer tests should be repeated several times and coherence values, which are between 0 and 1 as shown in Figure 3-3, should be checked for closeness to 1. A representative hammer impact test setup is shown in Figure 3-2 for the robotic milling system.

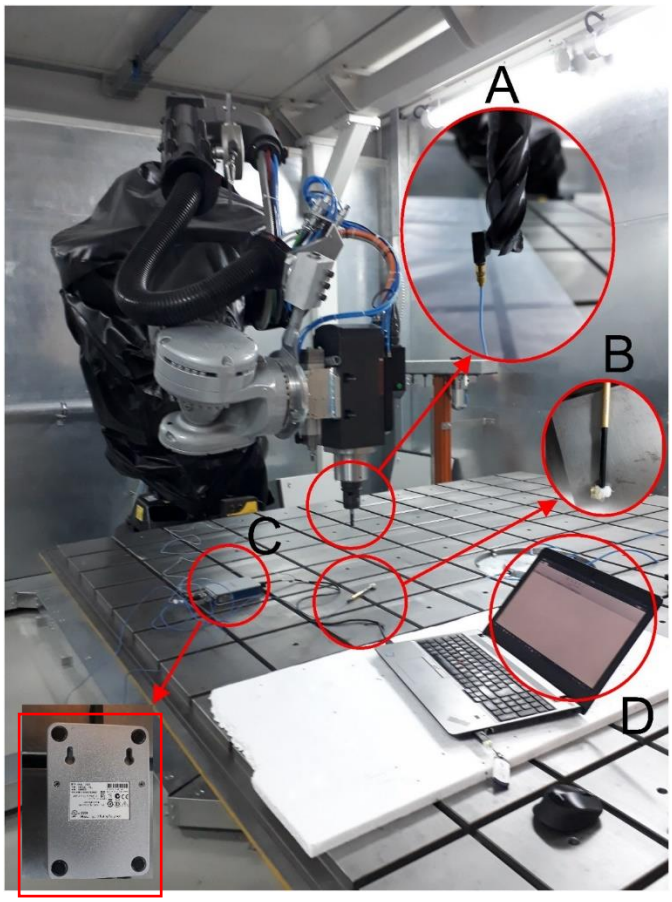

Figure 3-2: Representative impact hammer test setup for robotic milling system A.) The uniaxial accelerometer B.) Mini Modal Hammer C.) Data acquisition system D.) Computer and software

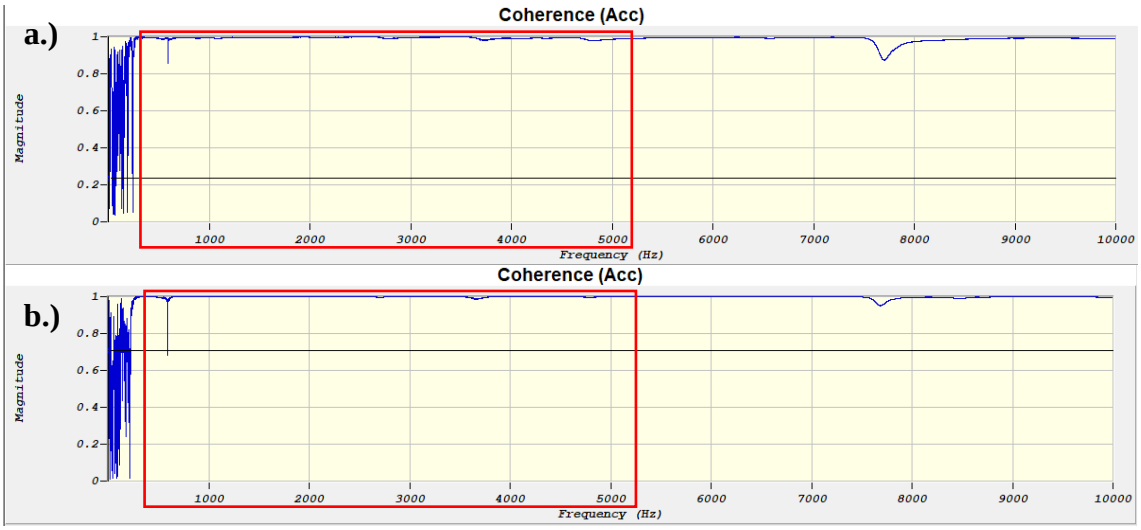

Figure 3-3: Coherence values for (a) Gxx (X direction) and (b) Gyy (Y direction) with used frequency range (red rectangle)

In Figure 3-2, representative carbide Ø12 flat end mill and uniaxial accelerometer, 352C22 PCB-PIEZOTRONICS, are represented with mounting position of the accelerometer as shown in Figure 3-2(A)-(B). 2301-Endevco-Meggitt mini-modal hammer is shown in Figure 3-2(A). Data acquisition board is shown in the Figure 3-2(C). and representative sofware is shown in the Figure 3-2(D). After giving the steps for modal hammer tests, the idea behind of the robotic configuration variation is illustrated in in terms of redundancy. 6 DOF industrial robots consist of links associated with one another by rotational joints. The kinematic analysis can be performed in two different ways, forward and inverse to change by transformations from joint directions to cartesian coordinates and the other way around as shown in Figure 3-4. In addition, tool position and orientaiton is defined with respect to end effector position and orientation by multiplying with another homogenous transformation matrix.

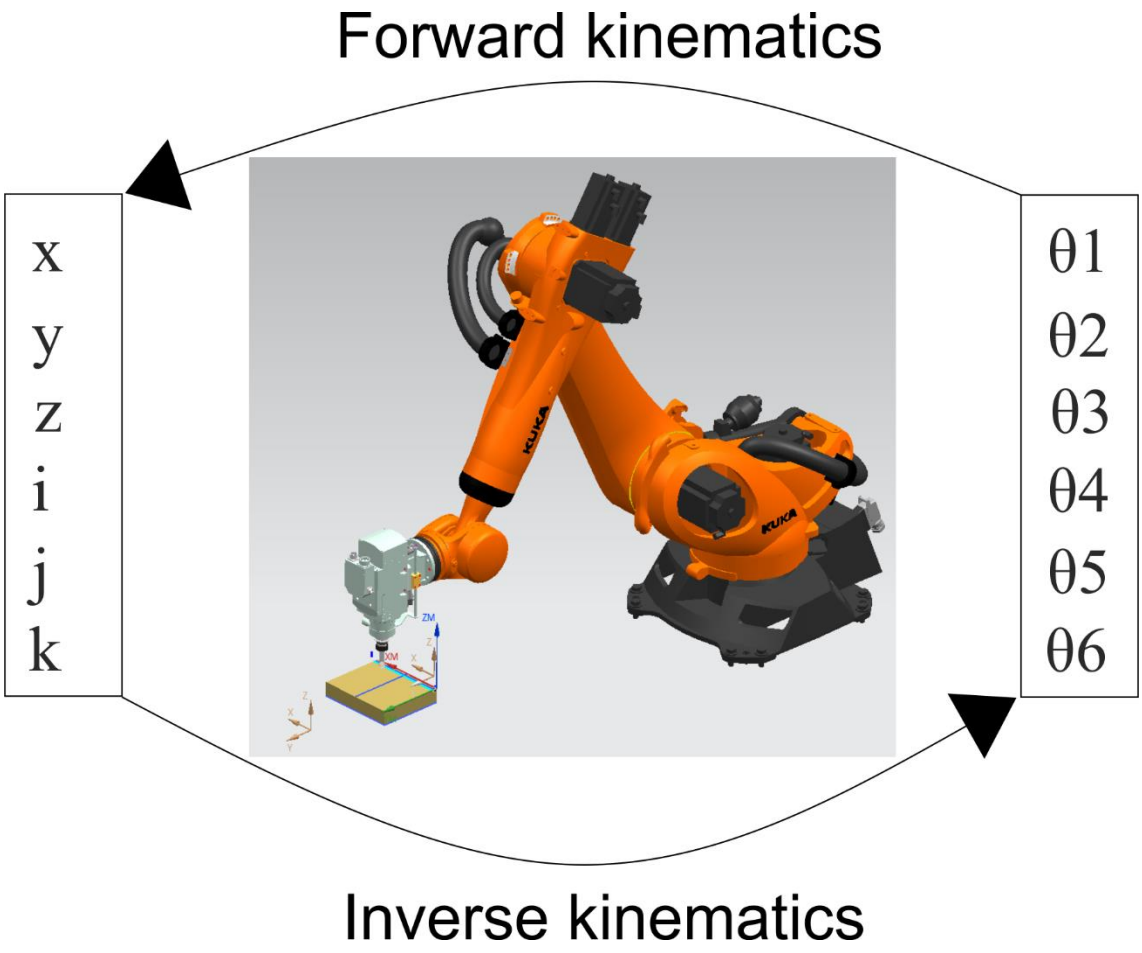

Figure 3-4: Representation of the forward and inverse kinematics for the tool position and orientation

KUKA KR240 R2900 6-axis serial arm robot was used to accomplish the milling operation as a milling robot. Robot kinematics was established dependent on the methodology proposed by Denavit and Hartenberg[39] utilizing 4x4 homogenous transformation matrices. In milling applications, the tool posture is defined by the tool tip position and tool axis. The translational movement is defined by 3D position x, y, z. Later on, 5-axis milling operations are defined by changing the lead and tilt angles and tool axis orientation is described by a unit vector i, j, k components. In this manner, kinematic redundancy is introduced to reach same position and orientation of the tool in different configurations. Configuration variation is illustrated in Figure 3-5.

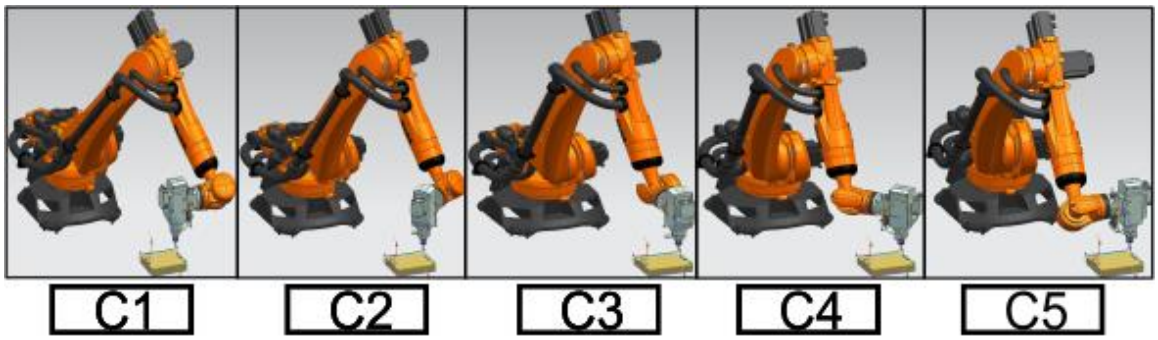

Figure 3-5: Definition of configurations in terms of redundant link rotation

Different configurations are defined as a rotation around the tool axis which is fixed. 5 different configurations are presented at the same location. When the robot approaches the workpiece with keeping its wrist parallel and the same direction regarding the feed direction in the X direction, it is named C1. Then, it is rotated 45° around the tool axis to create a distinguishable dynamic variation and related effect on tooltip dynamics. Then, it is named as C2. Next, another 45° rotation is completed, and this configuration is named C3 which the wrist is perpendicular to the feed direction in the X-direction. Then, an additional 45° added to the C3 and it is named as C4. The last configuration is named C5 which the wrist of the robot is parallel and opposite side of the feed direction in the X-direction. To reach C5 from C4, another 45° rotation around the tool axis is provided. Thus, the description of the different configurations is completed for the X-axis. 5 different configurations are used, and maximum wrist rotation is defined 180°. Same procedure is followed for Y direction and same configuration sequence is used.

3.1 Milling Dynamics

The tool tip dynamics is defined as a coupled reaction of robot structure, spindle, tool holder and the tool. In this coupling, the robot dynamics largely varies over its entire workspace, where the dynamics of different parts are assumed to be not involving or fixed. Although assuming the dynamics of other parts are fixed, robot's configuration and position contribute to the tool tip dynamics which is affected by joint configuration and robot kinematics. By taking directional contribution of the robot's structure into consideration, reflection to the tool tip is investigated in terms of FRFs. In such a manner, aforementioned coupling is shown in Figure 3-6.

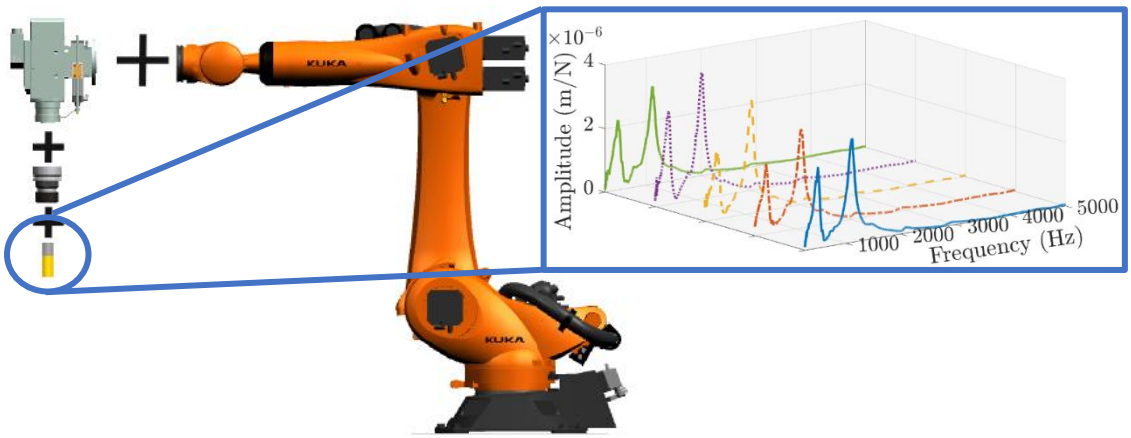

Figure 3-6: Coupled response in robotic milling

The equations of motion for a 2-DOF milling operation required to be written in feed and cross-feed directions which corresponds to X and Y directions regarding the workpiece frame after obtained FRFs of the tooltip. Therefore, it is important to highlight that frequency response functions represent the dynamics of the tool tip along with principal directions, X and Y, which are shown in the equation (93) and equation (94) when milling operation is planned along the X direction. The feed and principal direction of the feed are illustrated in Figure 3-7.

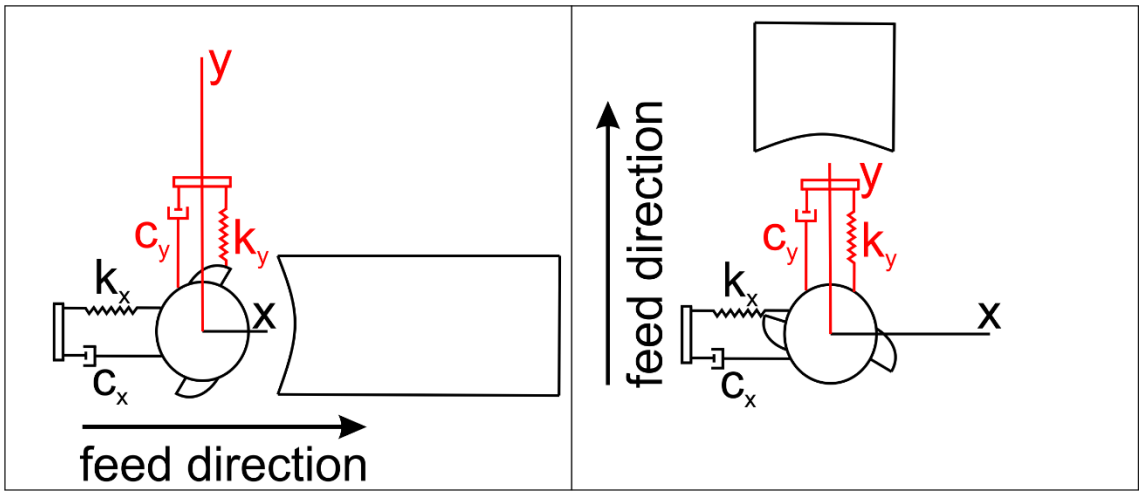

Figure 3-7: 2 DOF milling representation in principal directions regarding feed direction

$$Gxx = Gf \tag{93}$$

$$Gyy = Gcf \tag{94}$$

Equation (95) and equation (96) represent principal directions in terms of feed and cross-feed directions when the milling operation is planned along the Y direction.

$$Gxx = Gcf \tag{95}$$

$$Gyy = Gf \tag{96}$$

Regarding that, the stable depth of cut is related to the FRF in two directions, Gxx and Gyy, as solved in the frequency domain[40] for end milling operations the variation in the tool tip dynamics reflected in the stability lobes. Stable cutting depth for the end milling system is obtained by eigenvalue in terms of FRFs.

$$a_{lim} = -\frac{2\pi\Lambda_R}{NK_t}(1+\kappa^2)$$
$$\text{Here, } \Lambda = -\frac{1}{2a_0}\left(a_1 \pm \sqrt{a_1^2 - 4a_0}\right) \tag{97}$$

In Equation (97), ΛR is the real part of the eigenvalue Λ. κ is the ratio between the imaginary and the real part of the eigenvalue, which is also written in terms of the chatter frequency, ωc, and the tooth-passing period, T. In the stability solution proposed by Altintas and Budak[40], a0 and a1 are written in terms of the direct frequency response functions of the system, Gxx and Gyy. It should be noticed that in the stability solution, xx and yy are referred as the feed and cross-feed directions with respect to principal directions, X and Y, respectively. Although robot's wrist is rotating around tool axis, projection of the FRFs is not needed due to obtained FRF direction are aligned along the principal directions. FRF analysis and necessary experimental setup with modal hammer test location selection are explained in the following sections.

3.2 Robotic Milling Unit and Experimental Setup

Tests, simulations and experiments were performed by using the robotic milling system which contains KUKA KR240 R2900 6-axis serial arm robot controlled by KR C4 controller and 15-kW motorized spindle (ES789-H6161H1046) attached to the flange next to the 6th axis of the robot. Maximum spindle speed is 24 000 rpm. Rated payload on the robot is 240 kg which allows light, medium. The position repeatability can reach ± 0.06 mm and the maximum reachable distance is 2900 mm. Workpiece material is selected as Aluminum alloy 6061 and size of the workpiece is 350 x 296 x 100 (mm). Experiments designed regarding to dry cutting operations. Representative Ø20 indexable milling tool with 2 inserts (R390-11 T3 08M-MM S30T) is used to carry out cutting operations and FRF measurements as shown in Figure 3-8(a). Length of the indexable milling tool is $170^{\pm 0.05}$ mm, which is tightly fastened at 49.39 mm measured from the end of the tool and attached to the collet that is placed in DIN69893 HSK-F63 (Ø2-20). To

measure FRFs (tool tip FRFs at high-frequency band), 2301-Endevco-Meggitt mini-modal hammer is used and the uniaxial accelerometer, 352BG Dytran, is used to measure vibration as shown in Figure 3-8(a)-(b). Mounting position of the accelerometer and alignment of the mini modal hammer position is shown in the Figure 3-8(c). CutPro© simulation software is used for stability lobe simulations based on the FRF results.

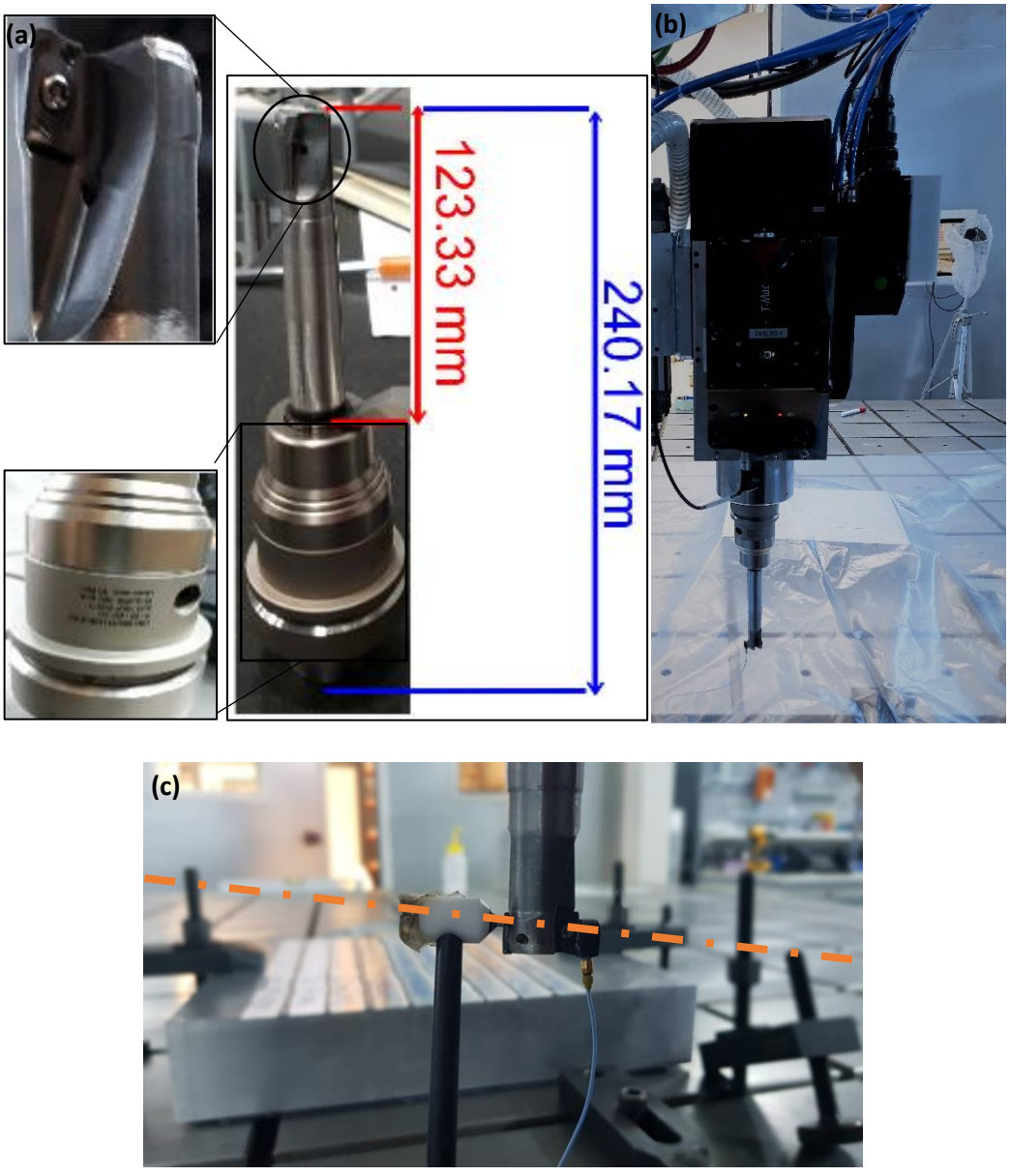

Figure 3-8: (a)Indexable milling tool with inserts and length properties, (b) milling tool, accelerometer and spindle representation (c) alignment of the accelerometer and mini-modal hammer position

3.3 Impact Hammer Test Location Selection

To analyze dynamic behavior, which differs from one position and configuration to another position and configuration, of the robot-tool system along the tool path. Progressive steps for convenient FRF measurement and stability lobe diagrams generation are given in Figure 3-9.

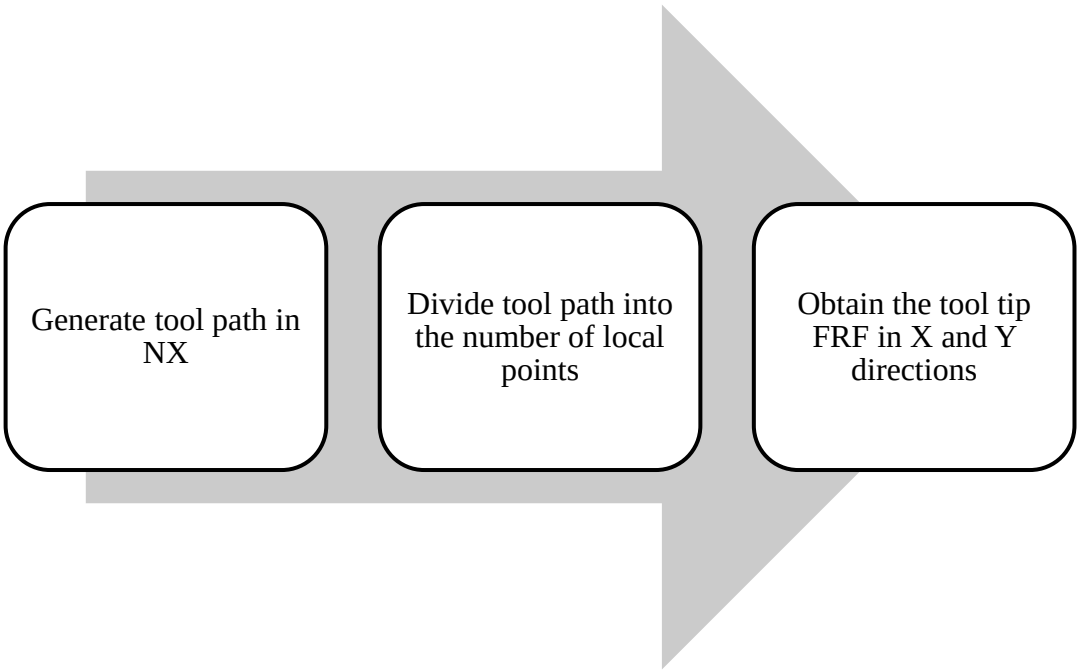

Figure 3-9: Steps of impact hammer test location and stability lobe diagram generation

First, reference tool path is designed to allow distinguished FRF measurements for different positions and configurations. Straight line tool path is generated in X direction which indicates the same direction with respect to robot base. According to the generated tool path, tool center points and G-codes are generated by using NX© and utilized to adoption of functionally redundant link of the robot. The tool path is divided 6 equal portions to be able determine FRF measurement positions of robot as given in Figure 3-10. In every point on the tool path, with varying position from one point to another, robot configuration has been changed between C1 to C5 as shown in Figure 3-5.

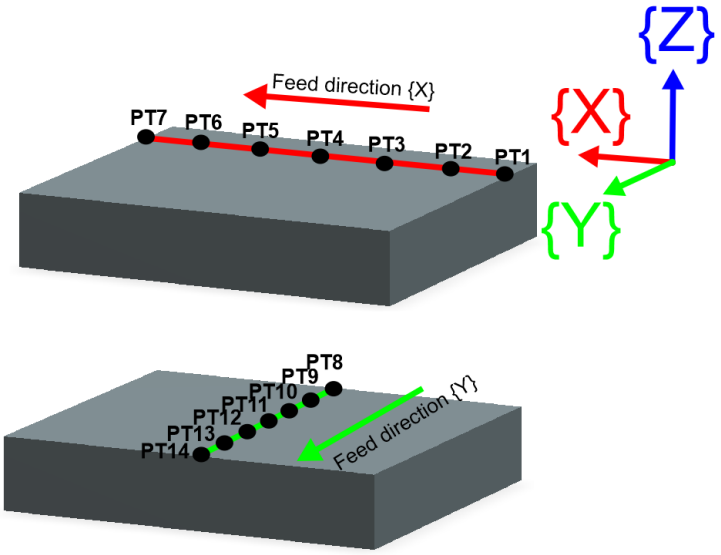

Figure 3-10: Workpiece and FRF measurement locations on the workpiece

By measuring FRFs at the tool tip in different configuration and positions, FRF differences are observed throughout along the tool path. As a second block of experiments, Y direction is used to evaluate FRF measurements and observe differences between X direction and Y direction as an effect of feed direction which allows to investigate positional dependency and configurational factor based on feed direction under the spindle speed limitations. Same procedure is followed in Y direction. G-code generating and adoption of functionally redundant link of the robot made by NX© and MATLAB©, respectively. Implementation of the programming approach is given in the section 3.4.

3.4 Implementation of Programming Algorithm based on Redundant Link Utilization

A programming algorithm is proposed for continuously variable configuration sequence in robotic milling for improved stable cutting conditions and proposed algorithm steps are schematized in Figure 3-11.

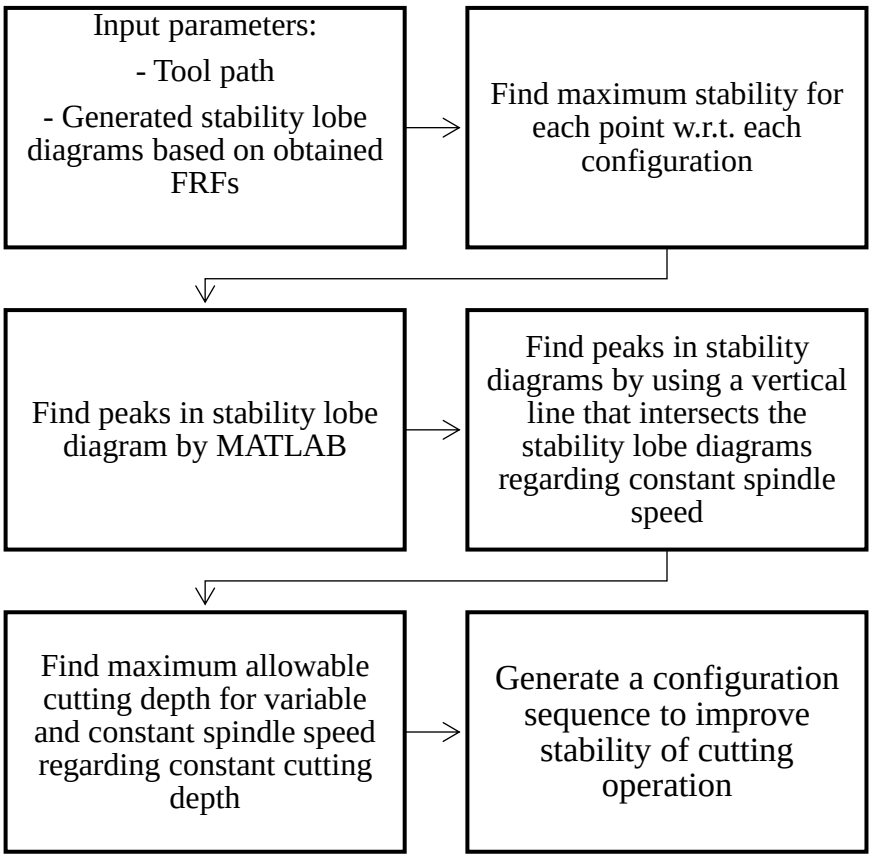

Figure 3-11: Steps for the automated programming algorithm for improved stable cutting conditions

Tool path and generated stability diagrams are given as inputs to the program. Program is utilized to find maximum stability limits for each configuration by searching all stability lobes in each location (position) on the workpiece. After the highest maximum stability detection for different configurations (see Figure 3-5) in each location on workpiece (see Figure 3-10), the configurations are determined with accompanying locations. Then, highest maximum stability with accompanying spindle speed is determined within all tool path with respect to positions and configurations. Configuration sequences without any restriction are generated based on this step. However, A vertical black line which intersects with stability lobe diagrams of the different configurations is generated to search allowable cutting depths with respect to constant spindle speeds (see Figure 4-2). By the help of this line, shifts in the configuration sequence can be determined with differences and another configuration sequence can be generated with applied restrictions such as spindle speeds and rotation of the redundant link. Configuration effect with accompanying positions is investigated for high speed robotic milling although positional dependency of the FRF variation is a well-studied and demonstrated phenomenon in robotic milling. These effects on FRFs

and dynamic characteristics of the robot are evaluated and demonstrated in the following sub-sections, 3.5 and 3.6 respectively.

3.5 Positional Dependency

Measured FRFs that taken from tool tip are plotted at 7 different position by using the same configuration. Observed modes contributed by tool holder and tool are seen in the Figure 3-12.

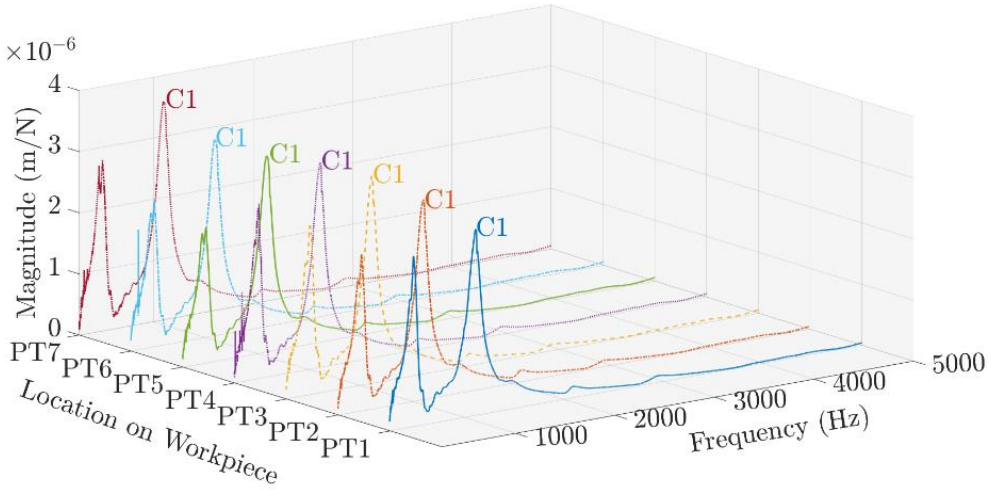

Figure 3-12: Representative positional dependency and accompanying tool mode shifts

Two significant modes are observed contributed by tool and tool holder around 500 Hz and 1100 Hz. The variation of tool modes in terms of natural frequency and magnitude are shown in Figure 3-13.

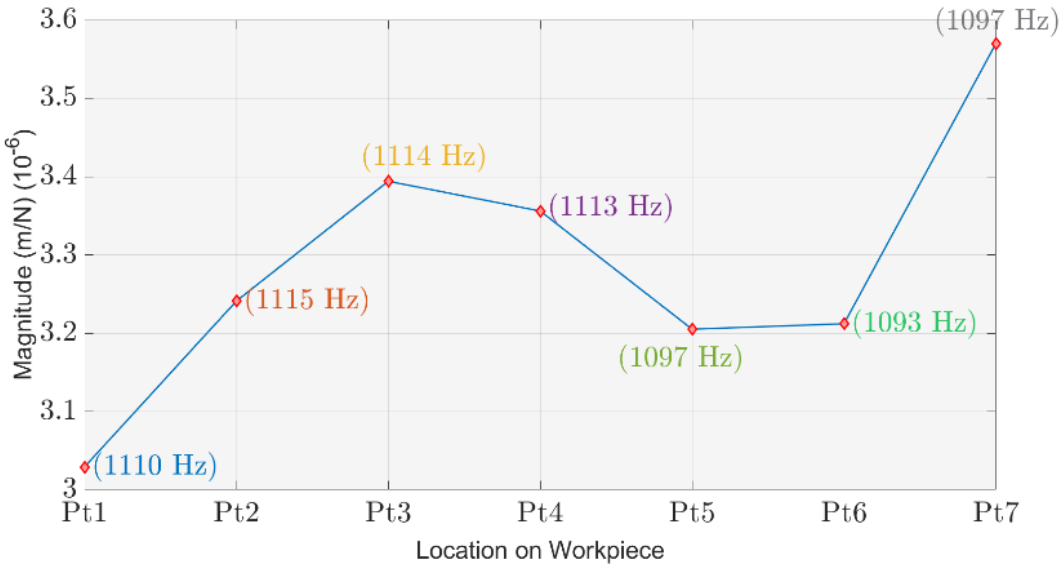

Figure 3-13: Tool mode variation in terms of amplitude and frequency with respect to positional variation

In Figure 3-13, effect of positions is evaluated and illustrated regarding to same configuration, C1. Variation of the tool modes in terms of magnitude and natural frequency is seen clearly from one position to another one. Highest dynamic rigidity observed at PT1-C1 as 3.029×10^{-6} m/N at 1110 Hz and lowest one observed at PT7-C1 as 3.570×10^{-6} m/N at 1097 Hz. As a comparison between first position and the last one taking into account, which indicates most rigid and flexible tool modes with respect to TCP positions all along the tool path, dynamic rigidity is decreased 17.86%. As position changing continuously, frequency of the tool mode shifts from 1110 Hz, 1115 Hz, 1114 Hz, 1113 Hz, 1097 Hz, 1093Hz and 1097 Hz, respectively. Variation in magnitude accompanies the frequency from 3.029 $\times 10^{-6}$ m/N to 3.241 $\times 10^{-6}$ m/N, 3.394 $\times 10^{-6}$ m/N, 3.356 $\times 10^{-6}$ m/N ,3.205 $\times 10^{-6}$ m/N, 3.212 $\times 10^{-6}$ m/N and 3.570 $\times 10^{-6}$ m/N, respectively. This variation reflects into stability lobe diagram plots in terms of positional effect.

3.6 Configurational Dependency

FRF measurements obtained from tool tip based on 5 different configurations are plotted with respect to the PT1 as a representative case. Then, evaluation for all points on the workpiece with different configurations has been carried out.

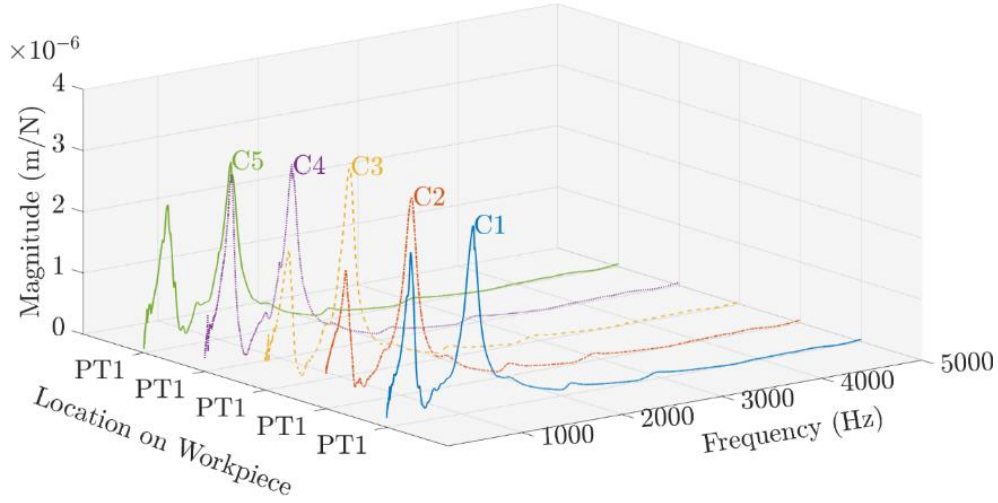

Figure 3-14:Tool mode variation in terms of amplitude and frequency with respect to configurational dependency

Two significant modes are observed contributed by tool and tool holder around 500 Hz and 1100 Hz as shown in Figure 3-14. The variation of tool modes in terms of natural frequency and magnitude are shown in Figure 3-15.

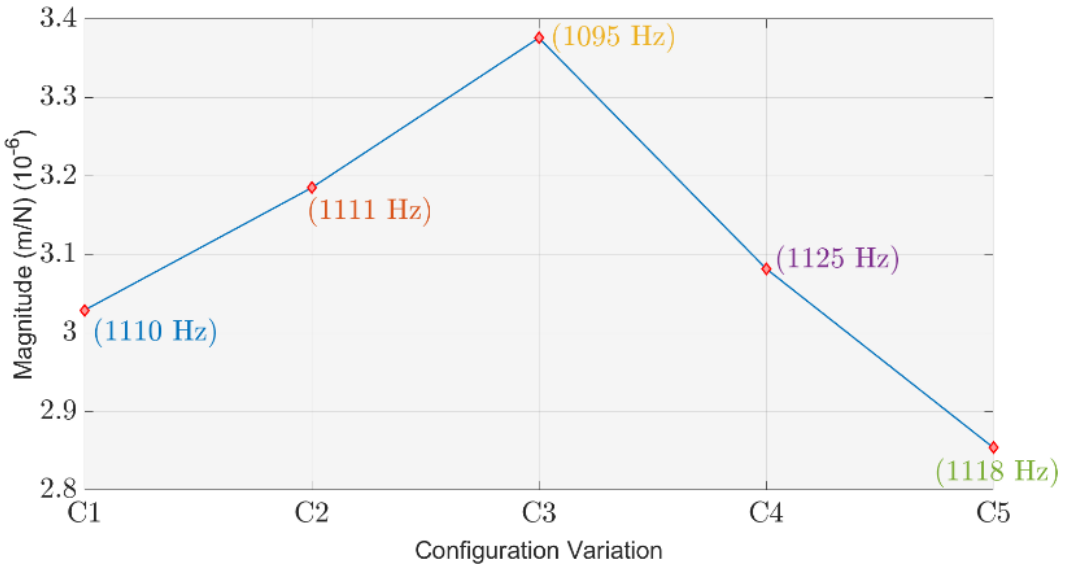

Figure 3-15: Variation in tool mode values at PT1

In Figure 3-15, the effect of configurations is evaluated and illustrated regarding to same position, PT1. Variation of the tool modes in terms of magnitude and natural frequency is plotted to evaluate the effect of configuration on the tooltip dynamics when redundant axis rotated from one configuration to another. Lowest dynamic rigidity observed at PT1-C3 as 3.326x10-6 m/N at 1095 Hz and highest one observed at PT1-C5 as 2.854x10-6 m/N at 1118 Hz. At the same location as configuration changes, C3 and C5 brought about the most flexible and rigid tool modes. Dynamic rigidity dropped 16.53% compared to the most flexible case. That percentage close to dynamic rigidity variation arising from the positional effect. This phenomenon demonstrated that changing configuration affects the tool tip dynamics at an approximate rate as positional dependency. As configuration variation taking into consideration, frequency of the tool mode shifts from 1110 Hz, 1111 Hz, 1095 Hz, 1125 Hz, and 1118 Hz, respectively. Variation in magnitude accompanies the frequency from 3.029 x10-6 m/N to 3.185 x10-6 m/N, 3.376 x10-6 m/N, 3.082 x10-6 m/N ,2.854 x10-6 m/N with respect to the order of configurations. This variation reflects into stability lobe diagram plots in terms of configurational effect.

3.7 Summary

In this chapter, the backbone for the stability investigation is explained depending on the obtained tool tip FRFs in conjunction with milling dynamics. Experimental setup for impact hammer tests and detailed information about setup such as tool length, spindle model, robot's payload, robot's repeatability with maximum reachable length, insert types for cutting tool, accelerometer type to acquire vibration and modal hammer type for high-frequency excitation are given in this chapter. Then, test location selection with the application of the program for redundant axis rotation is explained. In this manner, positional dependency, which is variation in the joint configuration during movement of the robot's end-effector, is explained in terms of tool tip's FRF variation. Next, configurational dependency is investigated and explained in terms of dynamic compliance when the robot's redundant link rotates around the tool axis at the same location.

CHAPTER 4: Stability simulations

After providing details for positional dependency and configurational dependency in terms of tool tip dynamics. To reveal the convenient configurations and identify highest stability limits regarding to position and configuration regarding workpiece material and process parameters, stability lobe diagrams are plotted. In this manner, positional and configurational effect on stability lobes are acquired. Then, depth of cut selection procedure and parameters are explained in section 4.1. Next, Different configuration structure generation is elaborated based on stability limits. This elaboration is followed by cases which contains different criteria to explore chatter characteristics along the generated tool path. This chapter is concluded with comparison between cases and related sub cases through simulations.

4.1 Stability predictions and simulation results

To reveal the convenient configurations and identify highest stability limits regarding to position and configuration by using workpiece material with process parameters, stability lobe diagrams are plotted, maximum and absolute stability conditions based on configurations are acquired. The effect of configurational dependency on stability limits is plotted in terms of stability lobe diagrams in as a representative case for last point, PT7, in the X direction with respect to all configurations as shown in Figure 4-1 (a)-(b)-(c) with different perspectives and magnification of the maximum stability zone, respectively.

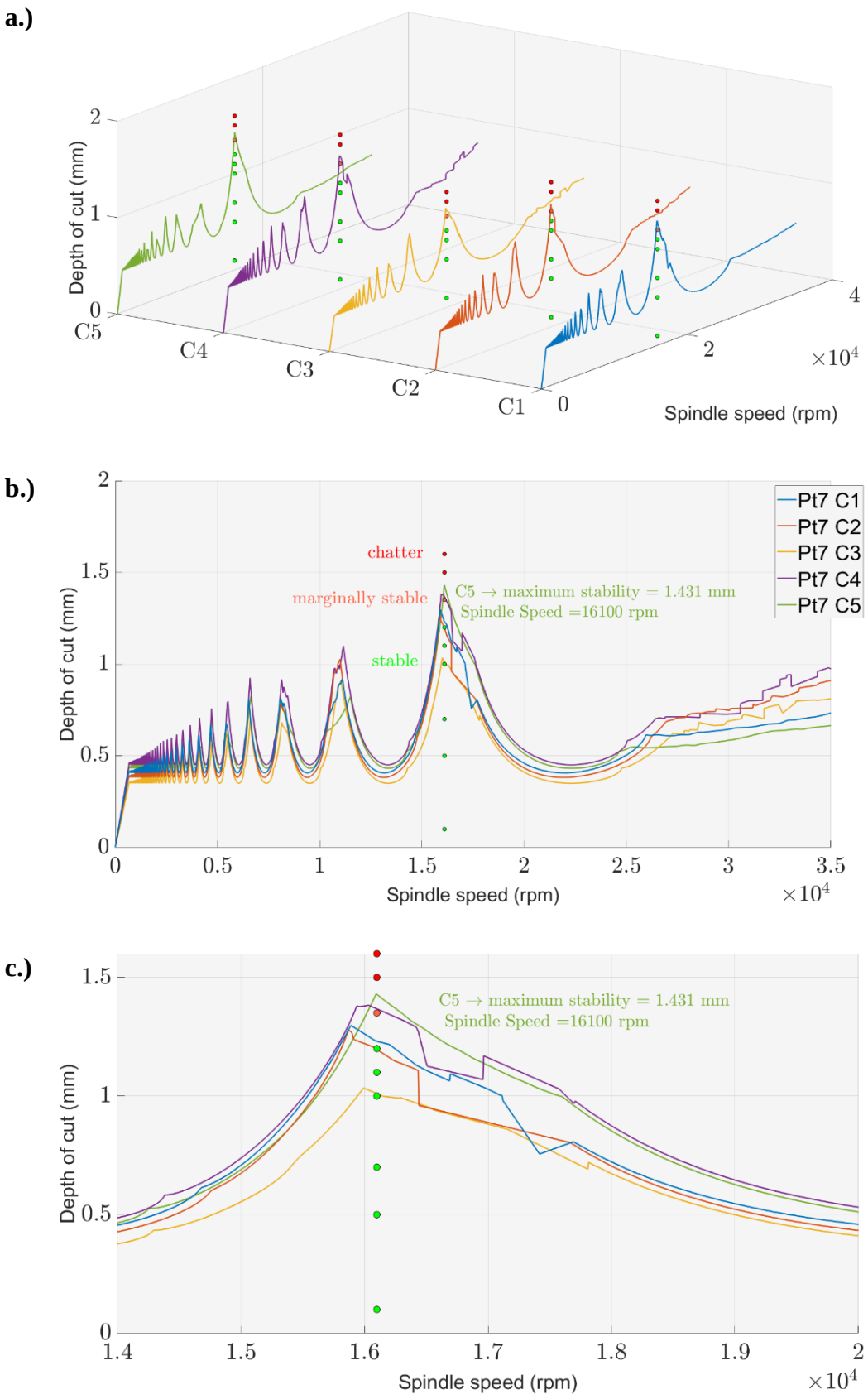

Figure 4-1: (a) stability lobe diagrams at PT7 (b) chatter representation from the front perspective at PT7 (c) maximum stability zone magnification at PT7

In evaluation of stability limits and identification of configurations based on the stability lobe diagrams for PT7, maximum stability limits are determined in terms of a sequence of configurations C5, C4, C1, C2, and C3 that correspond to 1.431 mm, 1.382 mm, 1.298 mm, 1.278 mm, and 1.034 mm, respectively. Among them, the highest maximum stability limit is achieved at the C5 where the accompanying depth of cut is 1.431 mm. To maintain improved stability limits, the preferable configuration is identified as C5 for the PT7. However, it should be noticed that variation in stability limits bring about different spindle speeds. In this case, as stability limit changes with the configuration in terms of maximum stability, spindle speed shifts from 16100 rpm to 16020 rpm,15890 rpm, 15870 rpm, and 16000 rpm, respectively, by using the same sequence. Therefore, once the stability limits based on configuration and related spindle speed is determined, alternatives should be convenient regarding to same spindle speed. In configuration adjustment, this procedure should be taken into consideration. In this regard, the highest maximum stability is used as a reference which corresponds to C5 at PT7. Therefore, spindle speed selection made based on that criteria which is related to 16100 rpm. At this spindle speed, stability intersection points are defined with respect to the black line passing through 16100 rpm by MATLAB©. Later on, the same procedure is followed to discover related maximum allowable depth of cuts at variable and selected constant spindle speeds.

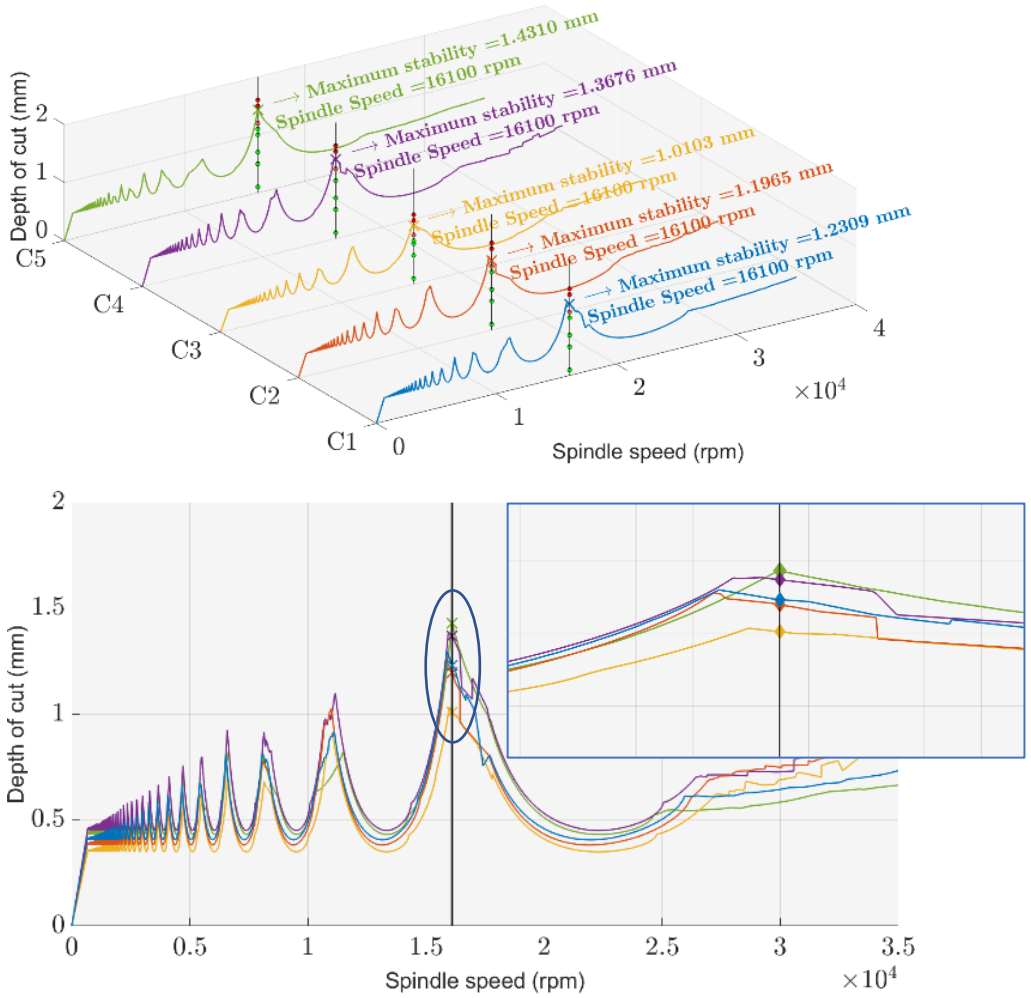

Figure 4-2: Consideration of configuration & dependent stability predictions & shifts in maximum stability at 16100 rpm

According to Figure 4-2, stability limits shifted slightly. Maximum allowable cutting depths can be sorted into 1.2309 mm, 1.1965 mm, 1.0103 mm, 1.3676 mm and 1.431 mm with accompanying configurations C1, C2, C3, C4 and C5, respectively. To compare variable spindle speed results and adjusted spindle speed results, Table 4-1 is created.

Configuration	**C1**	**C2**	**C3**	**C4**	**C5**
Spindle speed = variable#	1.298 mm 15890 rpm	1.278 mm 15870 rpm	1.034 mm 16000 rpm	1.382 mm 16020 rpm	1.431 mm 16100 rpm
Spindle speed = constant#	1.2309 mm 16100 rpm	1.196 mm 16100 rpm	1.010 mm 16100 rpm	1.367 mm 16100 rpm	1.431 mm 16100 rpm
Differences	0.0671 mm	0.081 mm	0.024 mm	0.014 mm	0 mm

Table 4-1: Variable and constant spindle speed (16100 rpm) comparison with respect to configurations

Differences, between constant spindle speed and variable spindle speed, are 67.1 µm, 81.5 µm, 23.7 µm, 14.4 µm and 0 at the last configuration which is expected due to adjustments are made based on that configuration which was selected as maximum allowable cutting depth. In that case, one configuration, C5, is chosen and comparisons are made by taking last point, PT7, into the consideration.

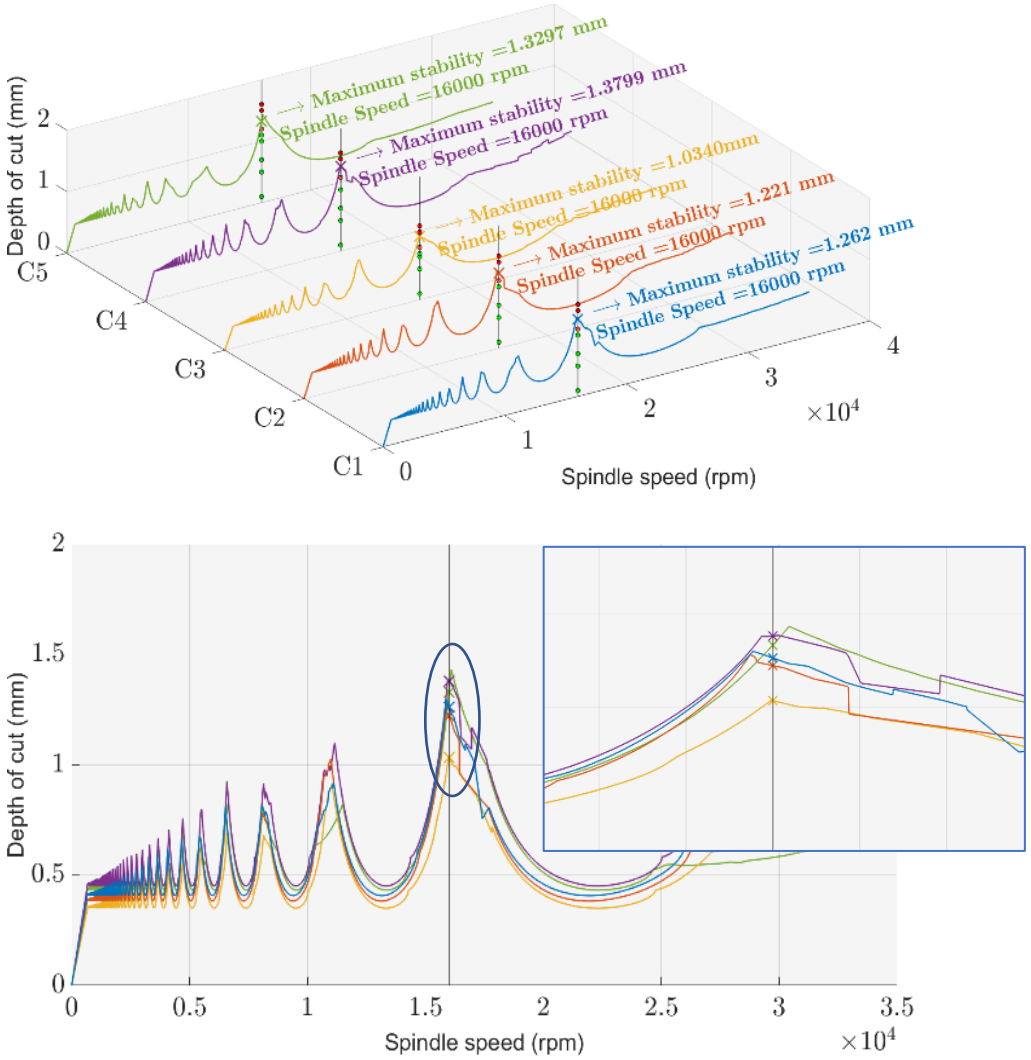

Table 4-2: Consideration of configuration & dependent stability predictions & shifts in maximum stability at 16000 rpm

According to Figure 4-2, stability limits shifted slightly. Maximum allowable cutting depths can be sorted into 1.2309 mm, 1.1965 mm, 1.0103 mm, 1.3676 mm and 1.431 mm with accompanying configurations C1, C2, C3, C4 and C5, respectively. To compare variable spindle speed results and adjusted spindle speed results, Table 4-3 is created.

Configuration	C1	C2	C3	C4	C5
Spindle speed = variable#	1.298 mm 15890 rpm	1.278 mm 15870 rpm	1.034 mm 16000 rpm	1.382 mm 16020 rpm	1.431 mm 16100 rpm
Spindle speed = constant#	1.262 mm 16000 rpm	1.221 mm 16000 rpm	1.034 mm 16000 rpm	1.379 mm 16000 rpm	1.3297 mm 16000 rpm
Differences	0.036 mm	0.057 mm	0 mm	0.002 mm	0.1013 mm

Table 4-3: Variable and constant spindle speed (16000 rpm) comparison with respect to configurations

Differences, between constant spindle speed and variable spindle speed, are 67.1 µm, 81.5 µm, 23.7 µm, 14.4 µm and 0 at the last configuration which is expected due to adjustments are made based on that configuration which was selected as maximum allowable cutting depth. In that case, C5 is chosen and comparisons are evaluated by taking last point, PT7, into the consideration.

In broad spectrum analysis, position effects with all configurations for the tool path are charted. Evaluations and analyses are collected to evaluate position effects from a wider perspective. Highest and lowest stability limits are identified along the tool path for X and Y directions as given with cutting depth values in Figure 4-3 and Figure 4-4, respectively.

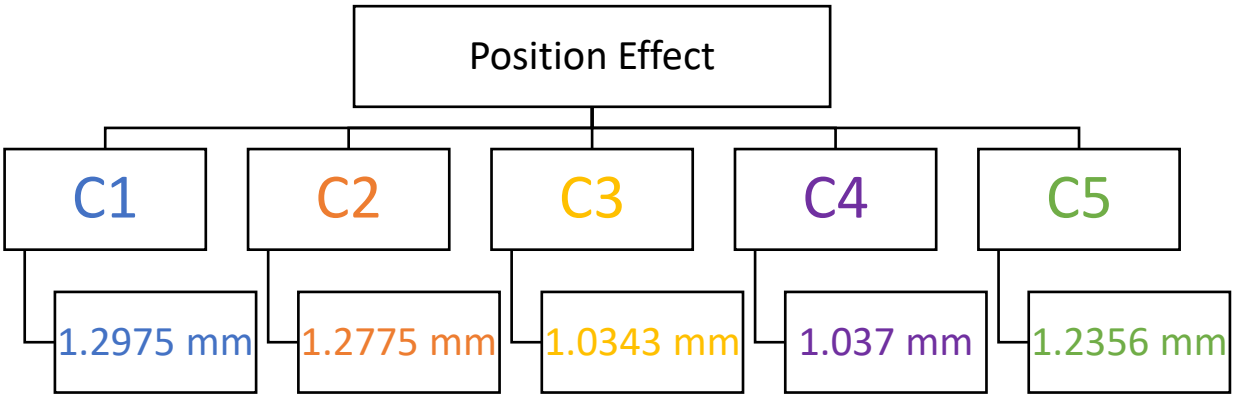

Figure 4-3: Position effects in terms of lowest maximum stability regarding related configurations in X direction

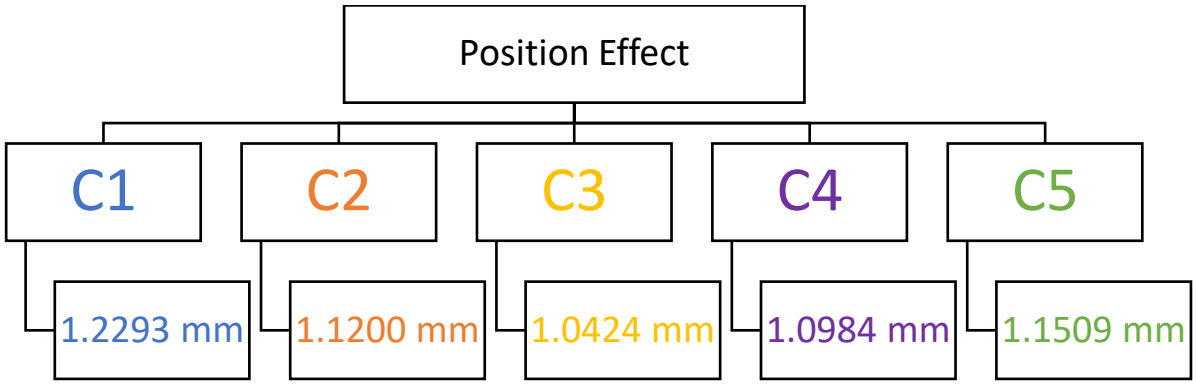

Figure 4-4: Position effects in terms of lowest maximum stability regarding related configurations in Y direction

When C1 is used for each segment of the tool path, lowest maximum stability, which is 1.2975 mm, is observed at the last point, PT7. Other configurations evaluated based on same criteria and highest constant depth of cuts are given in Figure 4-3 as reflection of the positional effect on the stability limits regarding same configuration conditions for X direction. When configuration selected as C2 for all the fractions of the toolpath, lowest maximum stability limit is identified as 1.2775 mm. Later on, evaluation for C3, C4 and C5 is completed. According to evaluation of stability limits, lowest maximum stabilities can be sorted as 1.0343 mm, 1.037 mm and 1.2356 mm. Restrictive points can be sorted as PT7, PT7, PT7, PT5 and PT5. At these points, lowest maximum stability observed. These limits are identified for variable spindle speed case. Results of the all different configurations are charted as shown in Figure 4-4 in terms of highest cutting depths along the tool path for Y direction. When C1 is selected throughout tool path, maximum allowable constant cutting depth is identified as 1.2293 mm and lowest maximum stability is observed at PT8 which is determiner along the tool path in terms of cutting depth. Same approach applied for Y direction and lowest maximum stabilities are identified. Restricted maximum allowable depth of cuts is sorted with related locations on the workpiece; 1.1200 mm, 1.0424 mm, 1.0984 mm, 1.1509 mm for C2, C3, C4 and C5, respectively. Accompanying restrictive locations on the workpiece are given as; PT9, PT9, PT10 and PT8, respectively.

Points	PT1 (rpm)	PT2 (rpm)	PT3 (rpm)	PT4 (rpm)	PT5 (rpm)	PT6 (rpm)	PT7 (rpm)
C1	15985	15990	15980	15990	15905	15815	15890
C2	16080	15900	15915	15985	15950	15850	15870
C3	15980	15980	16005	16085	16015	15995	15995
C4	16130	15965	16020	16040	15975	15885	16035
C5	16150	16080	16170	16140	16005	16050	16095
Points	**PT8 (rpm)**	**PT9 (rpm)**	**PT10 (rpm)**	**PT11 (rpm)**	**PT12 (rpm)**	**PT13 (rpm)**	**PT14 (rpm)**
C1	15995	15970	15920	15925	15975	15860	15940
C2	15920	15925	15870	15900	15870	15865	15880
C3	16005	15915	15915	15970	15985	15900	15925
C4	16035	16270	15855	16055	16050	16010	15985
C5	16160	16165	16095	16125	16145	16080	16110

Table 4-4: Points and related spindle speeds for maximum stability w.r.t. constant depth of cut in Y direction

Constant cutting depth is taking into consideration as restriction criteria. Thus, constant and variable spindle speed adjustment are completed and explained in the following cases, even if different spindle speeds are convenient and available, all adjustment are made based on aforementioned criteria. In this manner, to calculate the impacts of the stability limit variations on the productivity, material removal rates can be calculated for each segment and then, average of removal rates are compared to be more explanatory. Different spindle speeds along the tool path are stated clearly to be more precise. These spindle speeds are listed in Table 4-4. In each segment from initial point to final point, spindle speed is distributed continuously. Therefore, average spindle speed is calculated between points to calculate MRR.

$$\text{Feed Rate} = \text{Spindle Speed x Number of Teeth x Feed per Tooth} \quad (98)$$

$$\text{MRR} = \text{Radial Depth of Cut x Axial Depth of Cut x Feed Rate} \quad (99)$$

Material removal rates are calculated based on equation (98) and (99). Cutting conditions and workpiece properties are given in Table 4-5.

Process	Robotic Milling
Milling Tool	Indexable milling tool with 2 inserts (R390-11 T3 08M-MM S30T)
Tool Diameter (mm)	Ø20
Feed per Tooth	0.1 mm/rev/tooth
Operation name	Full slotting
Feed Direction	X & Y direction
Milling Type	Down Milling
Workpiece	Aluminum 6061-T6
Hardness	95 Hb
Density	2.7 g/cm^3
Yield Strength	2.75x10^8 N/m^2

Table 4-5:Cutting conditions for X & Y direction with respect to the workpiece local frame and mechanical properties of aluminum 6061-T6

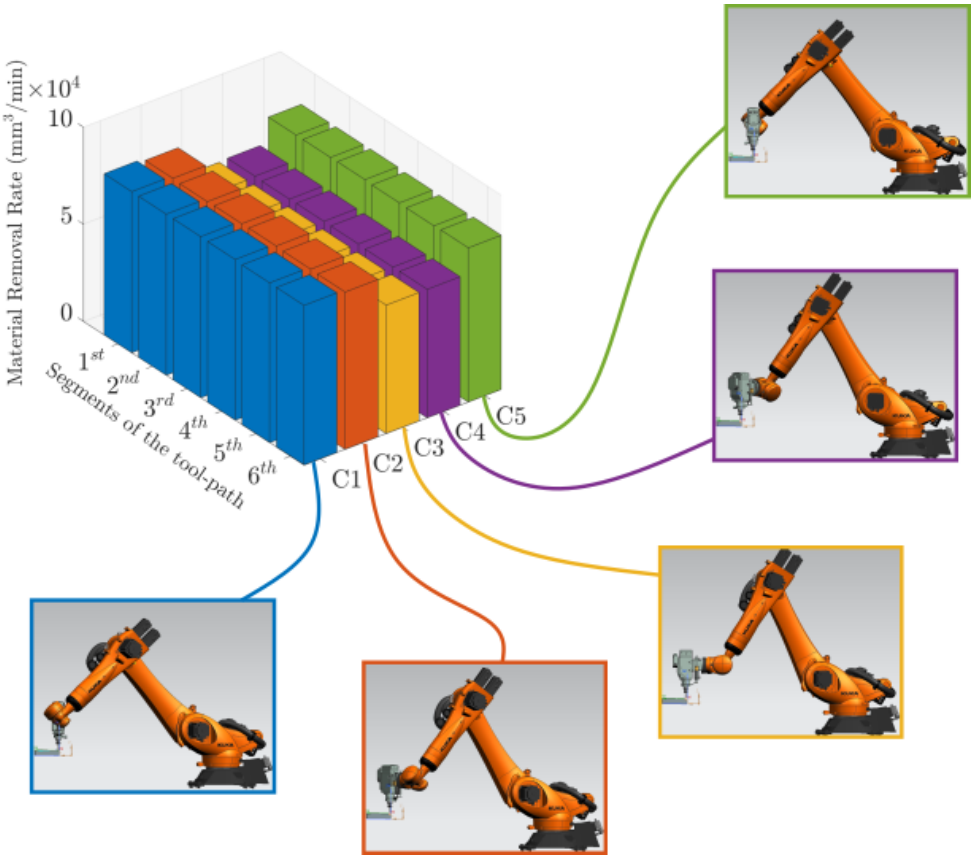

Figure 4-5: Material Removal comparison in X direction

Different configurations result in different MRRs although maintaining the same configuration throughout the tool path. MRR comparisons are shown in Figure 4-5 for X direction. Positional effect with different configurations can be used as a beneficial factor to increase the material removal rate. When C1 selected, the material removal rate is calculated 82975 mm^3/min approximately for the first segment of the tool path. MRRs calculated 82962 mm^3/min,82962 mm^3/min, 82767 mm^3/min, 82313 mm^3/min, and 82274 mm^3/min for the second, third, fourth, fifth and sixth segments of the tool path, respectively. When C2 selected as the main configuration, accompanying material removal rates observed approximately 81708 mm^3/min, 81287 mm^3/min, 81504 mm^3/min, 81593 mm^3/min, 81429 mm^3/min, and 81044 mm^3/min from first segment to last one, respectively. C3 is close by C4 in terms of material removal rate which is approximately 66241 mm^3/min and 66345 mm^3/min, respectively. In the case where the C5 is the main configuration, MRRs are varied from 79646 mm^3/min to 79696 mm^3/min and continue with 79844 mm^3/min, 79436 mm^3/min, 79214 mm^3/min and end with 79436 mm^3/min.

Based on the findings, C1, C2, C5, C4, C3 configuration sequence should be applied to maintain increased maximum stability limits at the highest level by using convenient configuration which is kept same throughout the tool path.

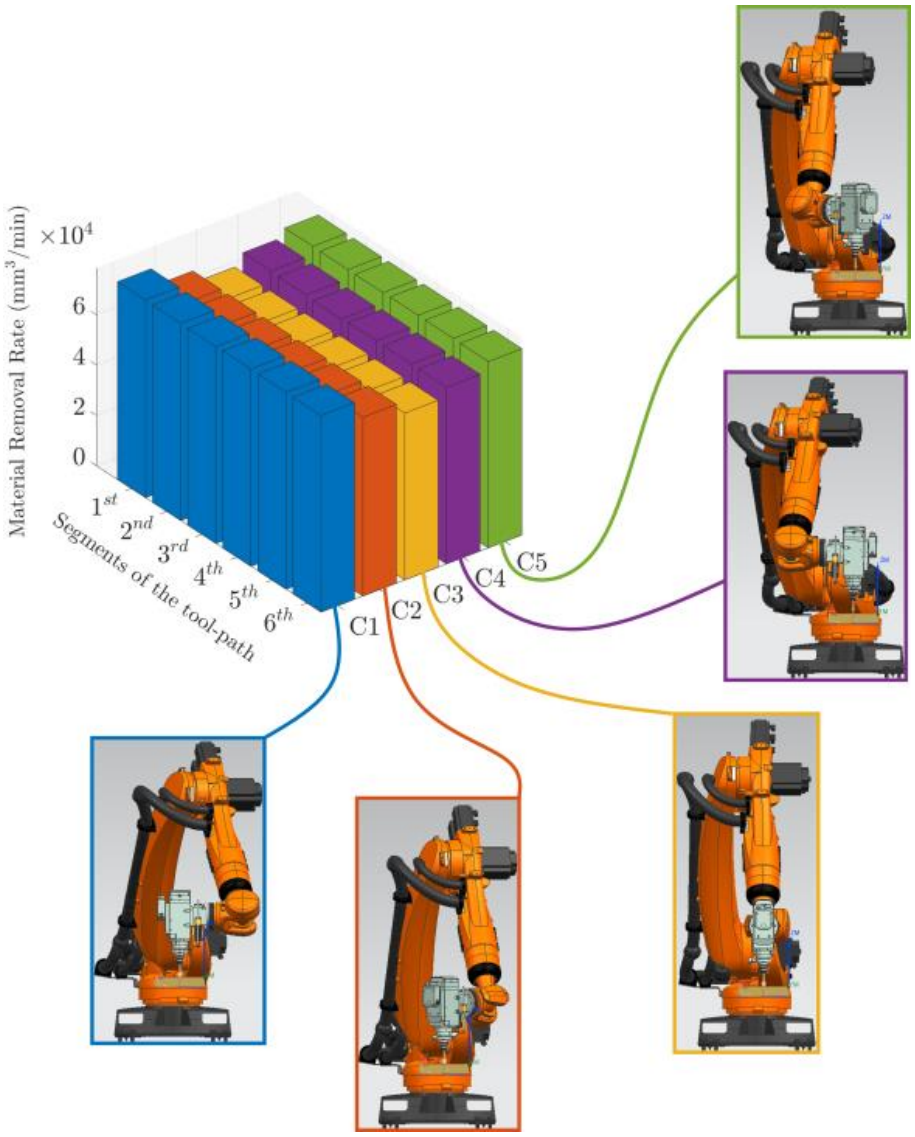

Figure 4-6: Material Removal comparison in Y direction

Same MRR methodology is used for Y direction and positional effect with different configurations based on redundant axis utilization can be used to improve and maintain the material removal rate. MRR comparisons are shown in Figure 4-6 for Y direction. When C1 is used as a reference configuration along the tool path, material removal rates are calculated 78590 mm^3/min, 78400 mm^3/min, 78290 mm^3/min, 78430 mm^3/min, and 78180 mm^3/min regarding the order of the segmentation. On average, 74230 mm^3/min is calculated as MRR when C5 is selected as base configuration. MRR is calculated 71180 mm^3/min where C2 is used throughout the tool path. 70481 mm^3/min and 66470 mm^3/min are calculated when C4 and C3 are used for the base configurations along the tool path, respectively. Based on the findings, C1, C2, C5, C4, C3 configuration sequence should be applied to maintain increased maximum stability limits at the highest level by using convenient configuration which is kept same throughout the tool path. This section is

followed by cases to reveal differences between position, configuration, variable spindle speed and constant spindle speed.

4.2 CASE 1: Maximum stability in X direction

To maximize the stability improvements, three different scenarios are formed in the following sub-cases. In the first scenario, Case 1.1, a sequence is generated for the maximum stability without any restriction on the rotation of the wrist axis and spindle speeds. In the second scenario, constant spindle speed is taking into account which corresponds to the highest maximum stability among the configurations, and the accompanying spindle speed is 16100 rpm. This limitation and influence on the stability limits are explained in the Case 1.2. In the third scenario, the lowest maximum stability limit's spindle speed is selected for comparison which is 16000 rpm. The effects of the lowest stability limit's spindle speed are investigated and illustrated in the Case 1.3. Then, the results of the different scenarios are compared, and differences are discussed.

4.2.1 Case 1.1: Maximum stability in X direction – Variable spindle speed

A configuration sequence is formed for the maximum improved stability. This sequence is sorted into C1, C2, C5, C5, C1, C3 and C5 in terms of stability with respect to order of locations on the workpiece. It is plotted in Figure 4-7.

Figure 4-7: Configuration identification based on maximum stability in X direction

Maximum depth of cuts is sorted into 1.471 mm, 1.435 mm, 1.466 mm, 1.509 mm, 1.428 mm, 1.419 mm and 1.431 mm, respectively. Limiter depth of cut for constant depth cutting operation is identified as 1.419 mm which corresponds to location at PT6. In this configuration structure, three different reductions and a huge increment observed among

all configurations in PT2, PT5, PT6, and PT4 respectively in terms of stability limits, respectively. Accompanying spindle speeds are 15990 rpm, 15900 rpm, 16170 rpm, 16140 rpm, 15910 rpm, 16000 rpm and 16100 rpm with respect to cutting depths and related locations on the workpiece. This sequence is followed by the spindle speed adjustment for 16000 rpm. However, to carry out milling operation along the tool path, other aims should be included, and stability limits should be investigated under these constraints which contains 3 different limitations: constant spindle speed, constant maximum allowable depth of cut and rotation of redundant axis.

4.2.2 Case 1.2: Maximum stability in X direction – Constant Spindle Speed (16000 rpm)

In this case, a configuration sequence is created for the adjusted spindle speed at 16000 rpm. Configuration structure is sorted into C1, C2, C1, C1, C1, C3 and C4 regarding order of the locations on the workpiece. This sequence is illustrated in Figure 4-8.

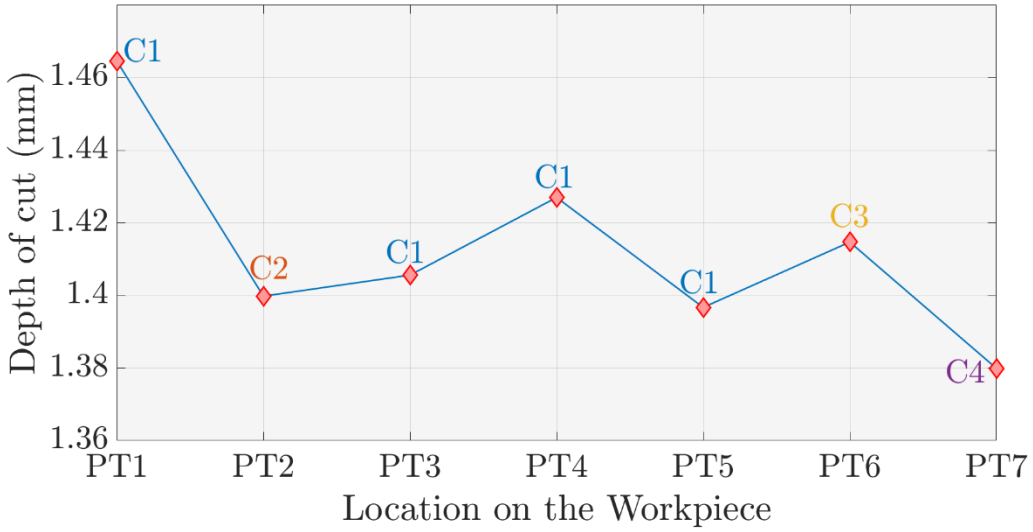

Figure 4-8: Configuration identification based on maximum stability along the tool path at 16000 rpm

When spindle speed adjusted to the 16000 rpm, sequence is re-written as C1, C2, C1, C1, C1, C3 and C4. Accompanying cutting depths are 1.465 mm, 1.400 mm, 1.406 mm, 1.427 mm, 1.397 mm, 1.415 mm and 1.380 mm. Maximum cutting depth dropped from 1.419 mm to 1.380 mm. According to the difference between configurations, sequence should be re-adjusted to cope with shifts in the stability limits zone.

4.2.3 Case 1.3: Maximum stability in X direction – Constant Spindle Speed (16100 rpm)

In this case, another configuration sequence is generated for 16100 rpm. The configuration structure is sorted into C1, C5, C5, C5, C1, C3 and C5 regarding the order of locations on workpiece which are highest in terms of depth of cut. This sequence is plotted in Figure 4-9.

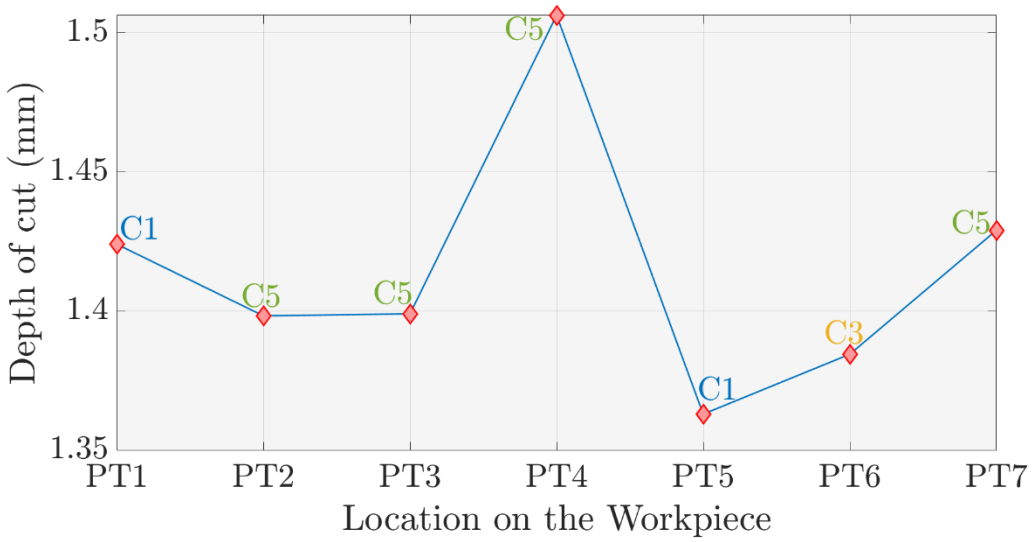

Figure 4-9:Configuration identification based on maximum stability along the tool path at 16100 rpm

Maximum depth of cuts are 1.424 mm, 1.398 mm, 1.399 mm, 1.506 mm, 1.363 mm, 1.385 mm, and 1.429 mm. Peak point is observed in PT4 at C5 which possesses the maximum cutting depth among the alternatives at 16100 rpm. However, lowest stability observed around PT5 at C1 which is highest among alternatives in terms of cutting depth and it is selected as reference for constant cutting depth milling operation. In this manner, determiner for the constant cutting depth is switched from the 1.380 mm to 1.363 mm. Then, all configuration structures in CASE 1 are compared to distinguish the effects of spindle speeds and re-adjusted configuration sequence in terms of milling stability. This comparison is plotted in Figure 4-10.

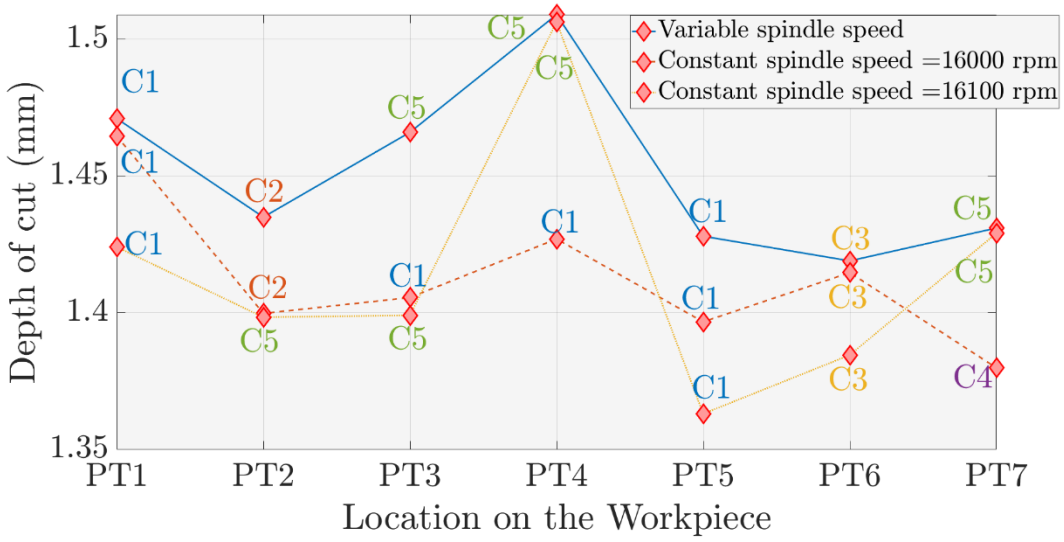

Figure 4-10: Comparison on different spindle speeds at maximum stability without rotation restriction

Maximum stability configuration comparisons and identifications are evaluated to cover all possibilities throughout the tool path in X direction. In terms of maximum stability, configuration sorting is made as C1, C2, C5, C5, C1, C3 and C5 with accompanying depth of cuts which can be sorted 1.471 mm, 1.435 mm, 1.466 mm, 1.509 mm, 1.428 mm 1.419 mm and 1.431 mm, respectively. According to maximum stability versus preferable configuration evaluation, configurations of the robot must vary between C1 and C5 along the tool path. However, excessive rotations may cause either intermittent motions of robot or robot stops which is not desired during the process. For instance, in that case, distance between PT4 and PT5 is approximately 58.5 mm which is relatively short distance for robot to change its configurations from C5 to C1. This variation in the configuration close to the 180 ° that is not feasible for short distances and may cause harm to the robot due to attempted commissioning the commands written in G-code. In addition to harm, robot is getting more prone to deviation along the straight toolpath. That cause immense loss in accuracy. Therefore, an alternative sequence is generated to decrease rotation angle around fixed tool axis and these sequences are explained in CASE 2.

4.3 CASE 2: Maximum stability in X direction with rotation constraint

To avoid harmful rotation and accuracy loss, decrement in the maximum stability can be acceptable to a certain extent. In this manner, three different scenarios are presented in the following sub-cases. In the first scenario, Case 2.1, a sequence is generated for the maximum stability by restricting the maximum rotation into the half which is

corresponding to the 90° where the maximum rotation occurs. In the second scenario, constant spindle speed is taking into account which is the highest maximum stability among the configurations, and the accompanying spindle speed is 15900 rpm. This limitation and influence on the stability limits are explained in the Case 2.2. In the third scenario, the lowest maximum stability limit's spindle speed is selected for comparison which is 15920 rpm. The effects of the lowest stability limit's spindle speed are investigated and illustrated in the Case 2.3. Then, the results of the different scenarios are compared, and differences are discussed.

4.3.1 Case 2.1: Maximum stability in X direction with rotation constraint – Variable spindle speed

In this case, configuration sequence is generated regarding rotation constraint between C2 and C4. This sequence is sorted into C4, C2, C2, C4, C2, C3, and C4 as shown in Figure 4-11.

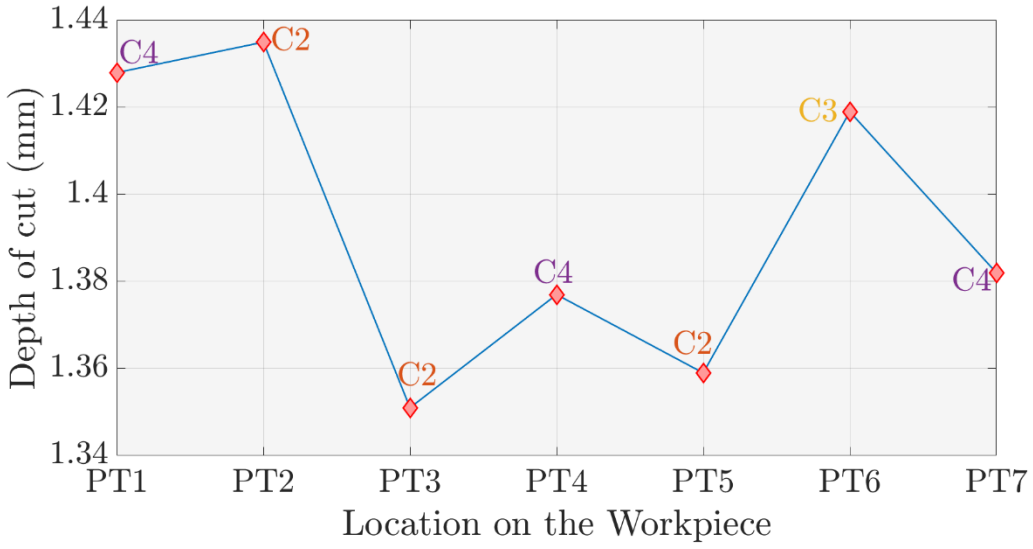

Figure 4-11: Configuration identification based on maximum stability along the tool path regarding variable spindle speed & limited configuration variation between C2—C4 in X direction

To stay in the limited rotation boundary by using configuration variation, configuration limits are selected between C2 and C4. Aiming to limited rotation and maximum stability, the following sequence is generated. The maximum allowable depth of cuts change from 1.428 mm to 1.435 mm and continue with 1.351 mm, 1.377 mm, 1.359 mm, 1.419 mm, and ends at 1.382 mm. Accompanying spindle speeds are identified as 16130 rpm, 15900 rpm, 15920 rpm, 16040 rpm, 15960 rpm, 16000 rpm, and 16040 rpm. In this case,

restricting depth is 1.351 mm at PT2 which corresponds to C2 in terms of configurational dependency. By changing spindle speed along the tool path, 1.351 mm can be identified as a maximum constant depth. Although all configurations between C2 and C4 with effects of them on stability limits are evaluated for each location, a huge decrement is observed between PT2 and PT3. Constant spindle speed cases are investigated in the Case 2.2 and Case 2.3.

4.3.2 Case 2.2: Maximum stability in X direction with rotation constraint – Constant spindle speed (15900 rpm)

The maximum and minimum values of the Case 2.1 are used to keep spindle speed constant in terms of stability limits. A sequence is generated and sorted into configurations: C4, C2, C2, C4, C2, C3, and C4. In this sequence, C2 at PT2 is identified as the highest stability limit with accompanying spindle speed at 15900 rpm. The results are plotted in Figure 4-12.

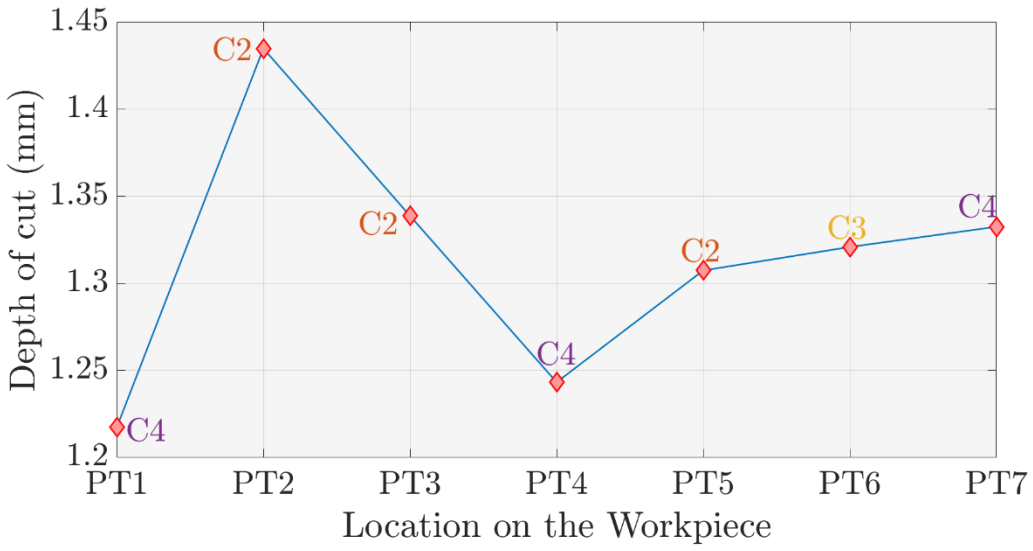

Figure 4-12: Representative plot on maximum stability along the tool path regarding constant spindle speed at 15900 rpm & limited configuration variation between C2—C4 in X direction

When spindle speed is selected as 15900 rpm, depth of cuts is varied from 1.2174 mm, 1.435 mm, 1.3389 mm, 1.2433 mm, 1.3075 mm to 1.3326 mm with respect to the locations on the workpiece, respectively. However, the maximum stability limit is dropped from 1.351 mm to 1.2174 mm at PT1. This decreased stability is identified as the most deviated when spindle speed kept constant. In this case, limiter depth switched from C2 at PT3 to C4 at PT1 compared to Case 2.1. Differences between the Case 2.1

and Case 2.2 are identified. The maximum deviation is calculated as 0.2106 mm at PT1, and the second maximum deviation is calculated as 0.1337 mm at PT4, C4. Other deviations can be accepted as negligible due to differences are under 0.1 mm.

4.3.3 Case 2.3: Maximum stability in X direction with rotation constraint – Constant spindle speed (15920 rpm)

C2 at PT3 is determined as limiter for constant spindle at 15920 rpm speed implementation. First, all stability limits are identified with respect to 15920 rpm and results are shown in Figure 4-13.

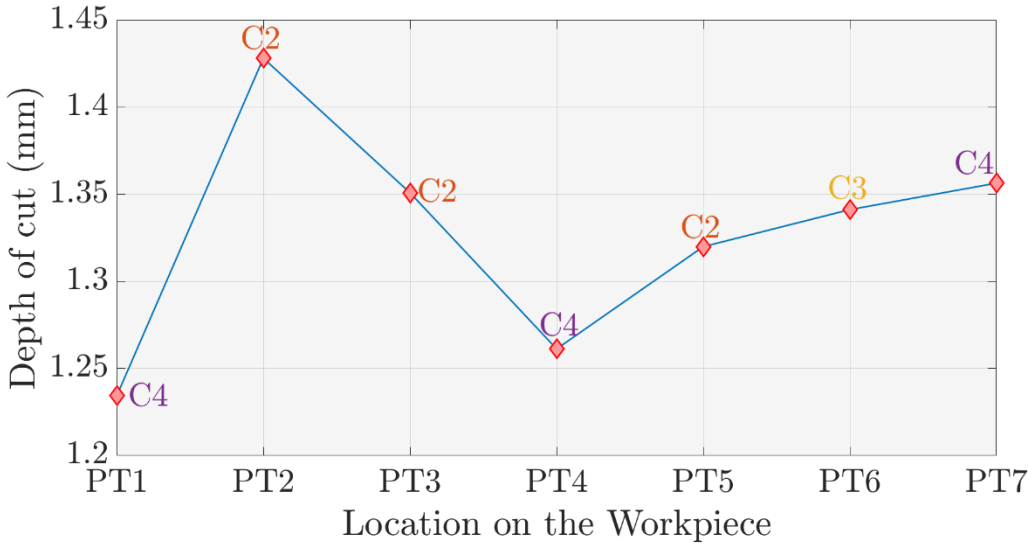

Figure 4-13: Representative plot on maximum stability along the tool path regarding constant spindle speed at 15920 rpm & limited configuration variation between C2—C4 in X direction

When spindle speed is selected as 15920 rpm, maximum stability limit is dropped from 1.351 mm to 1.2344 mm at PT1. This decreased stability is identified as the most deviated when spindle speed kept constant at 15920 rpm. In this case, limiter depth switched from C2 at PT3 to C4 at PT1 compared to variable spindle speed case. Configurations are not changed compared to Case 2.1 and Case 2.2. Deviations are minimally changed along the tool path. The maximum deviation is calculated as 0.1936 mm at PT1, C4, and the second maximum deviation is calculated as 0.1157 mm at PT4, C4. Other deviations at different locations are omitted due to small differences for machining applications. In Figure 4-14, comparison on different scenarios is plotted.

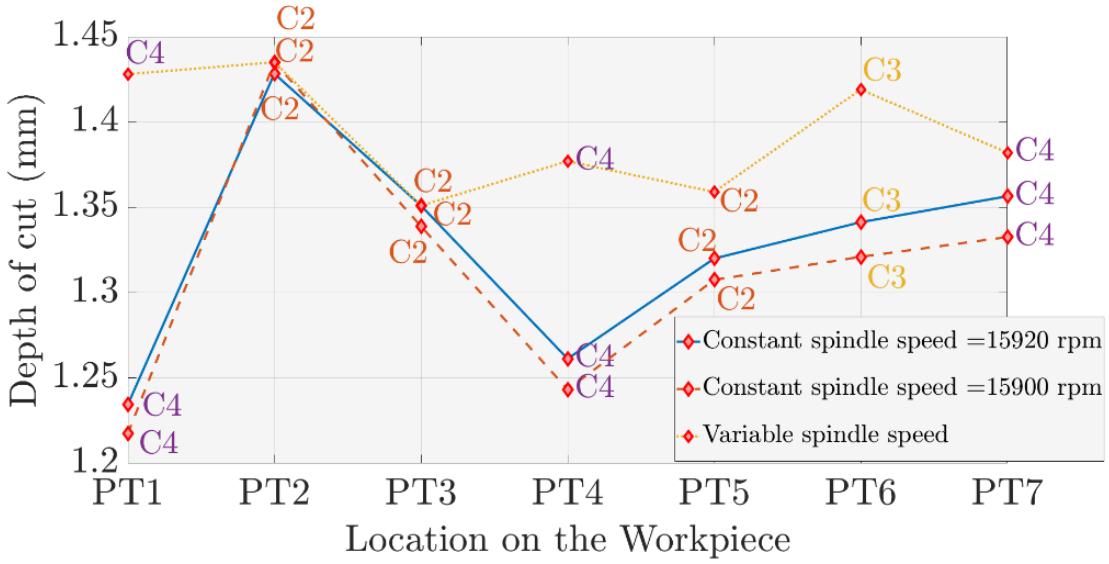

Figure 4-14: Comparison on different spindle speeds at maximum stability — in CASE 2 in X direction

Utilization of the redundant axis with rotation constraints has resulted in 1.351 mm in Case 2.1 as the highest constant depth of cut limit with variable spindle speed in terms of maximum allowable cutting depth. When spindle speed adjusted to 15920 rpm in Case 2.2, C4, at PT1 has appeared as lowest maximum stability which is used as a determiner for the constant depth of cut. Just as other adjustments for the constant spindle speed resulted in 1.2344 mm which identified as the lowest maximum stability throughout the tool path. Constant spindle speeds are close to each other. A significant deviation is observed at PT4 with respect to sub-cases. However, restrictive cutting depth for Case 2.1 is located in the last point, PT7, where other restrictive cutting depths are located in the first point, PT1, for Case 2.2 and Case 2.3. Thus, it is observed that deviations are not enormous in terms of stability limits. Stability limit deviations are observed as expected with the same trends.

4.4 CASE 3: Maximum stability in X direction without rotation

A sequence without rotation is generated to distinguish the differences between CASE 1, which maximum rotation is allowed, CASE 2, which limited rotation is allowed and CASE 3, which rotations are not allowed. C3 is selected as the reference configuration to compare. In this manner, three different scenarios are presented in the following sub-cases. In the first scenario, Case 3.1, a sequence is generated for the maximum stability without restricting the spindle speed variation. In the second scenario, constant spindle speed is taking into account which corresponds to the highest maximum stability among

the configurations, and the accompanying spindle speed is 15890 rpm. This limitation and influence on the stability limits are explained in the Case 3.2. In the third scenario, the lowest maximum stability limit's spindle speed is selected for comparison which is 15995 rpm. The effects of the lowest stability limit's spindle speed are investigated and illustrated in the Case 3.3. Then, the results of the different scenarios are compared, and differences are discussed.

4.4.1 Case 3.1: Maximum stability in X direction without rotation – Variable spindle speed

Constant configuration sequence is generated for the variable spindle speeds to maintain possible highest stability limits. Therefore, configuration kept constant throughout the tool path and maximum allowable depth of cuts are plotted in Figure 4-15 with respect to locations on the workpiece which introduces position effect of the robot's dynamic behavior and influence on the tool tip dynamics in X direction.

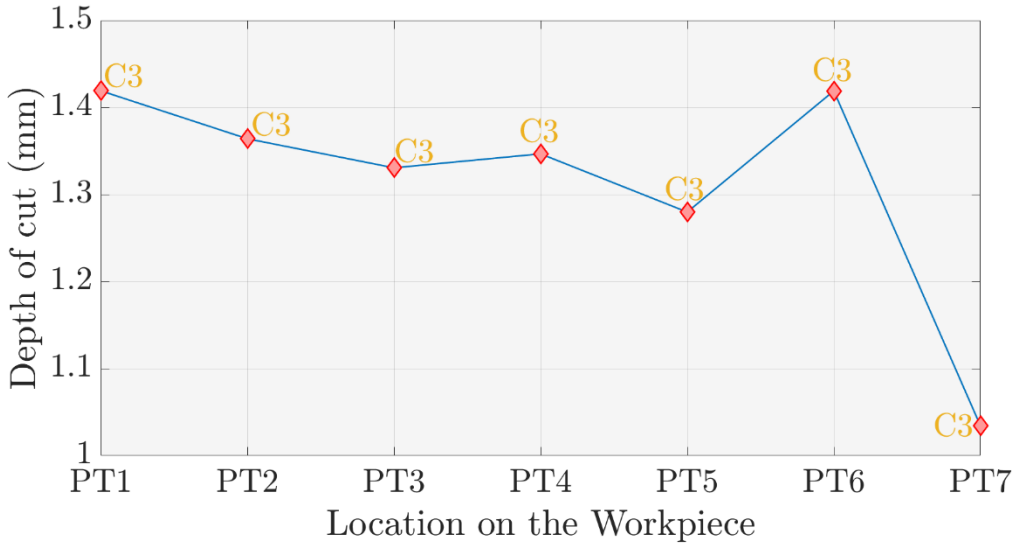

Figure 4-15: Variation in stability with respect to constant configuration —C3 in X direction

When configuration is selected C3, maximum allowable cutting depths are varied from the beginning of the tool path to the end of tool path as 1.4191 mm, 1.3640 mm, 1.3306 mm, 1.3467 mm, 1.2798 mm, 1.4189 mm and 1.0343 mm, respectively. In this case, restrictive depth of cut is identified at the last point of the tool path. At this point, accompanying spindle speed is identified as 15995 rpm. Limiter of the tool path for the constant cutting depth is found at the last location on the workpiece.

4.4.2 Case 3.2: Maximum stability in X direction without rotation – Constant spindle speed (15980 rpm)

In this case, constant spindle speed is selected 15980 rpm which has the maximum stability among other alternatives. When spindle speed is constant, maximum cutting depths are plotted in Figure 4-16 to distinguish the effect of constant spindle speed.

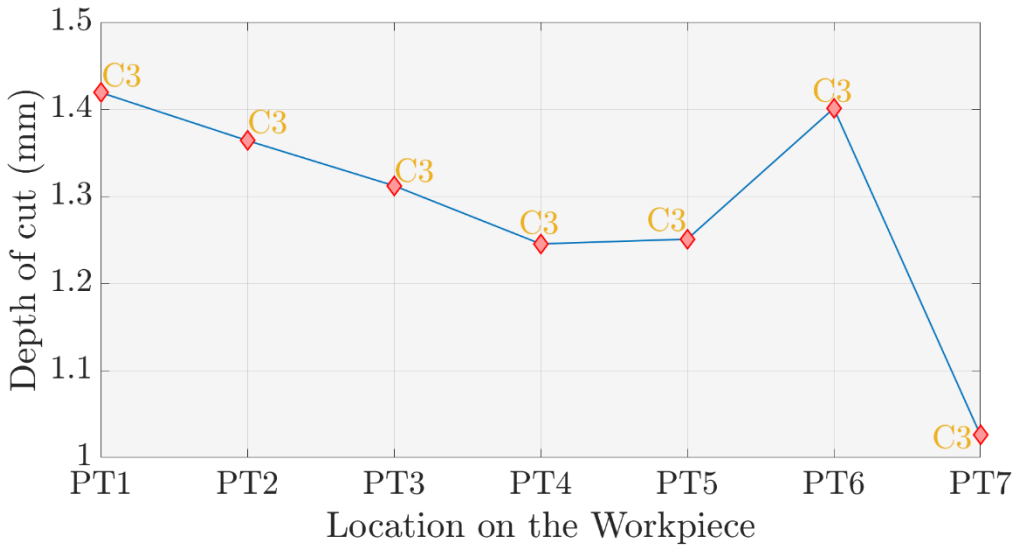

Figure 4-16: Variation in stability with respect to constant configuration —C3 at 15980 rpm in X direction

When spindle speed is selected 15980 rpm, maximum allowable cutting depths are varied from the starting point of the tool path to the last point of the tool path as 1.4191 mm, 1.3640 mm, 1.3122 mm, 1.2454 mm, 1.2508 mm, 1.4011 mm, and 1.0259 mm, respectively. In this case, the restrictive depth of cut is identified at the last point of the tool path. Additionally, maximum cutting depth dropped from the 1.0343 mm to the 1.0259 mm compared to Case 3.1. However, decrement in the maximum cutting depth is 0.089 mm which is negligible especially in robotic milling applications due to the robot's accuracy.

4.4.3 Case 3.3: Maximum stability in X direction without rotation – Constant spindle speed (15995 rpm)

In this case, constant spindle speed is selected 15995 rpm which is the lowest maximum stability among other alternatives compared to Case 3.1. When spindle speed is constant, variation in the maximum cutting depths are plotted in Figure 4-17 to distinguish the effect of different constant spindle speed regarding Case 3.2.

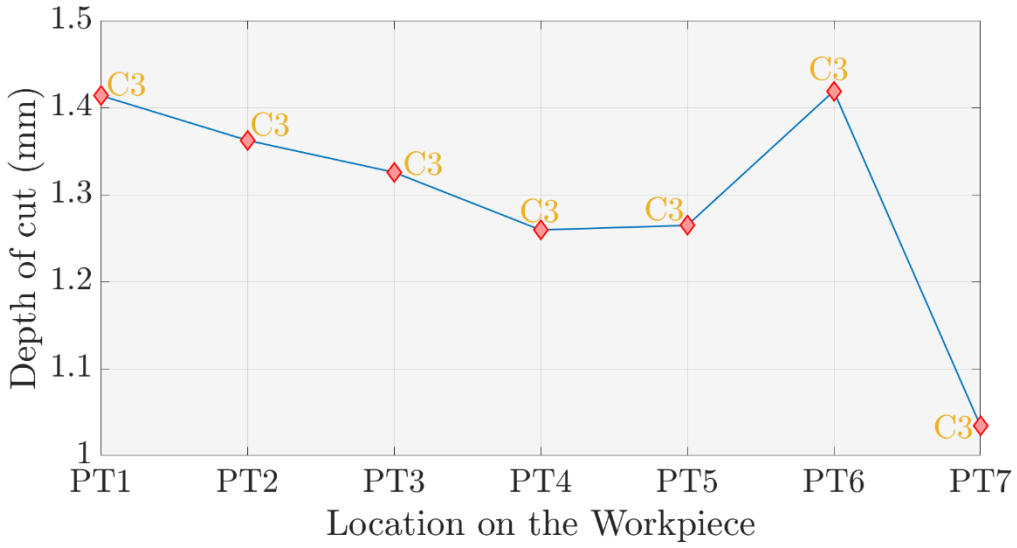

Figure 4-17: Variation in stability with respect to constant configuration —C3 at 15995 rpm in X direction

When spindle speed is selected 15995 rpm, maximum allowable cutting depths are varied from the beginning of the tool path to the end of the tool path as 1.4138 mm, 1.3624 mm, 1.3257 mm, 1.2594 mm, 1.2646 mm, 1.4189 mm, and 1.0343 mm, with respect to order of locations on the workpiece. In this case, the restrictive depth of cut is identified at the last point of the tool path and limiter cutting depth has not changed. Differences between sub-cases of CASE 3 are plotted in Figure 4-18 to reveal trends between sub-cases.

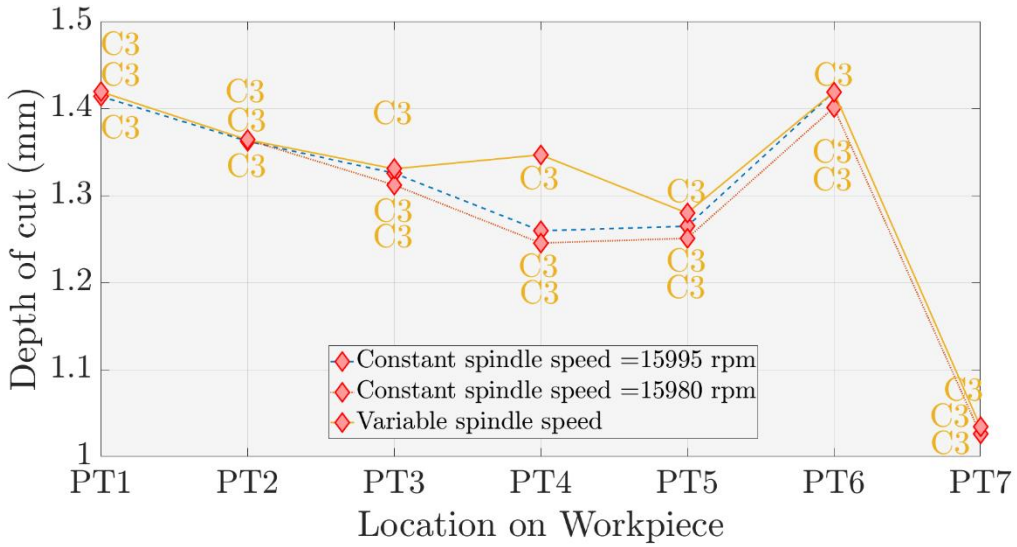

Figure 4-18: Comparison on different spindle speeds at maximum stability under constant configuration condition —C3 in X direction

Without rotation of the redundant axis has resulted in 1.0343 mm in Case 3.1 that the highest constant depth of cut limit with variable spindle speed in terms of maximum allowable cutting depth. When spindle speed adjusted to 15980 rpm in Case 3.2, PT7 has appeared as lowest maximum stability which is used as a determiner for the constant depth of cut. In Case 3.3, spindle speed adjustment is accomplished for the 15995-rpm resulted in 1.0343 mm which identified as the minimum constant depth of cut along the tool path. All of the sub-cases are close to each other and no meaningful differences are observed. A slight deviation is observed at PT4 with respect to sub-cases. In the first scenario, Case 3.1, the maximum allowable depth of cut is identified as 1.3467 mm at PT4, and in Case 3.2, cutting depth dropped from the 1.3467 mm to 1.2454 mm. In Case 3.2 at PT4, 1.2594 mm is found as the reachable cutting depth. Cutting depths are similar in Case 3.2 and Case 3.3. The highest difference is observed around 0.1 mm between Case 3.1, Case 3.2, and Case 3.3, respectively. Thus, it is observed that deviations are negligible in terms of usage of the robot for milling applications.

4.5 CASE 4: Maximum stability in Y direction

Three different scenarios are presented in the following sub-cases and the same procedure is followed in CASE 1 for Y direction. In the first scenario, Case 4.1, a sequence is generated for the maximum stability without limiting rotation and spindle speed variation. In the second scenario, constant spindle speed is taking into account which corresponds to the lowest maximum stability among the configurations, and the accompanying spindle speed is 15920 rpm. This limitation and influence on the stability limits are explained in the Case 4.2. In the third scenario, the lowest maximum stability limit's spindle speed is selected for comparison which is 15975 rpm. The effects of the highest stability limit's spindle speed are investigated and illustrated in the Case 4.3. Then, the results of the different scenarios are compared, and differences are discussed.

4.5.1 Case 4.1: Maximum stability in Y direction – Variable spindle speed

To maximize the stability along the tool path in the Y direction, a unique sequence of the configurations is used. The sequence and related allowable cutting depths are plotted in Figure 4-19.

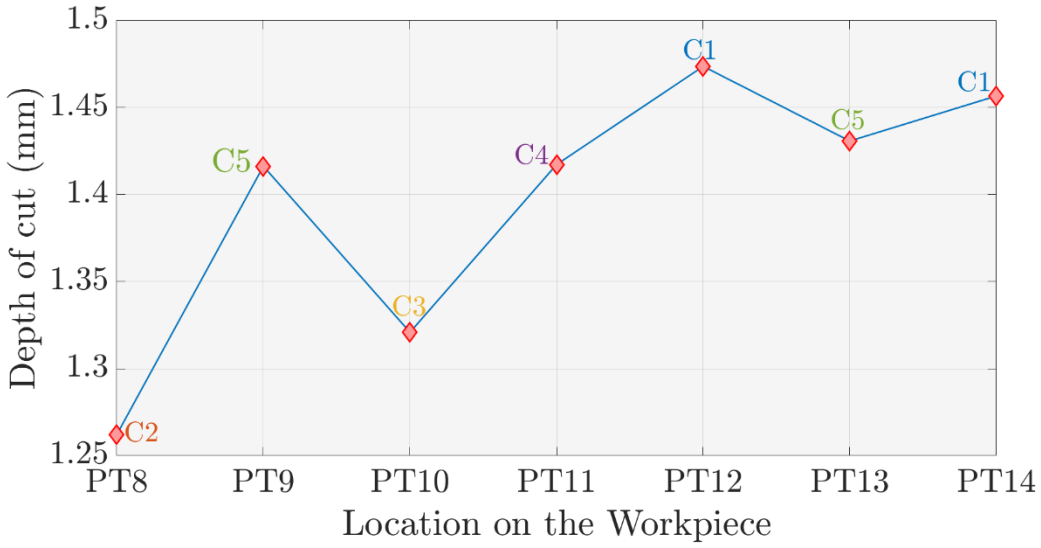

Figure 4-19: Configuration identification based on maximum stability in Y direction

Maximum stability configuration comparisons and identifications are evaluated to cover all possibilities throughout the tool path in Y direction. In terms of maximum stability, configurations can be sorted as C2, C5, C3, C4, C1, C5, and C1 with accompanying depth of cuts which can be sorted: 1.2621 mm, 1.4163 mm, 1.3209 mm, 1.4173 mm, 1.4737 mm 1.4308 mm and 1.4567 mm with respect to order of locations on the workpiece. The highest cutting depth is observed at C1 in PT12 where the lowest maximum cutting depth is encountered at C2 in PT8 among all configurations evaluated in the same position. According to this evaluation, the configuration of the robot's redundant axis should be changed between C1 and C5 along the tool path especially through the last portions of the tool path. Variation of the configuration reaches maximum limitations in a short distance which may cause loss in accuracy. Since the determiner is the lowest maximum stability for constant cutting depth, cutting operation should be limited with at most 1.2621 mm to prevent chatter and maximize productivity.

4.5.2 Case 4.2: Maximum stability in Y direction – Constant Spindle Speed (15920 rpm)

Limited rotation between C2 and C4 is generated at 15920 rpm to explore the effects of constant spindle speed on the stability limits. This sequence is placed in order as C2, C1, C3, C2, C2, C2, and C1. Result of the sequence , in terms of stability, and accompanying depth of cuts are plotted in Figure 4-20.

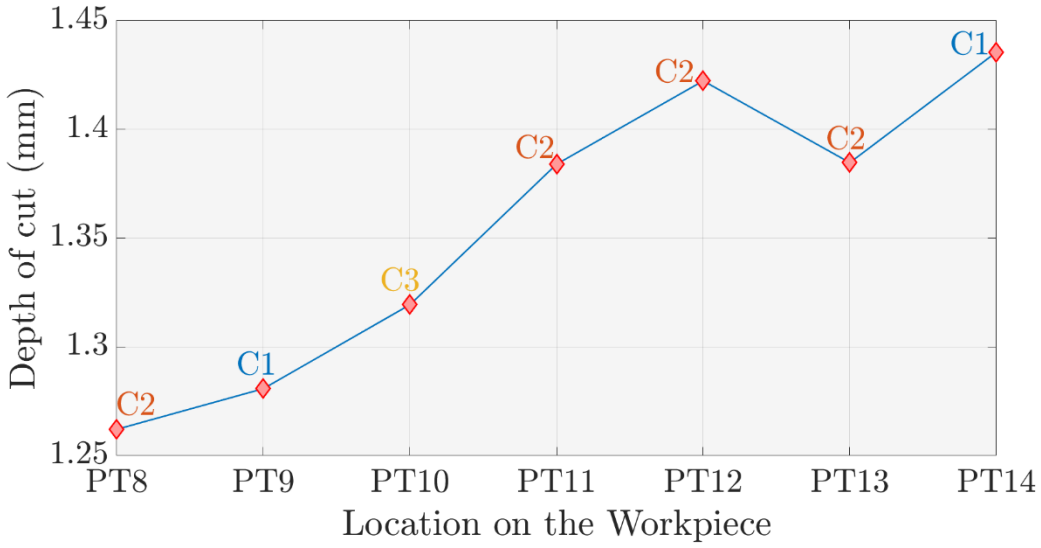

Figure 4-20: Representative plot on maximum stability along the tool path regarding constant spindle speed at 15920 rpm & limited configuration variation between C2—C4 in Y direction

When spindle speed adjusted to 15920 rpm, maximum allowable cutting depths are 1.2621 mm, 1.2808 mm, 1.3194 mm, 1.3840 mm, 1.4223 mm, 1.3847 mm and 1.4355 mm with respect to locations on the workpiece. These cutting depths are highest among all the configurations at the same location. Stability limits are rising from the starting points of the tool path until PT12 at C2. Then, depth of cut is reduced from 1.4223 mm to 1.3847 mm. Maximum allowable cutting depth is increased to 1.4355 mm at the last point of the tool path. Limiter depth of cut is observed as 1.2621 mm at PT8, C2.

4.5.3 Case 4.3: Maximum stability in Y direction – Constant Spindle Speed (15975 rpm)

Another sequence is generated for the constant spindle speed at 15975 rpm under the constraint of rotation between the C2 and C4. This sequence order is sorted as C2, C1, C3, C2, C1, C4, and C1 as shown in Figure 4-21.

Figure 4-21: Representative plot on maximum stability along the tool path regarding constant spindle speed at 15975 rpm & limited configuration variation between C2—C4 in Y direction

After the adjustment of the spindle speed, maximum cutting depths are identified as 1.2419 mm ,1.2789 mm ,1.3016 mm, 1.3609 mm, 1.4737 mm, 1.3800 mm,1.4437 mm. Rising trend in stability limits is reached to PT12. Then, maximum reachable cutting depth is decreased from 1.4737 mm to 1.3800 mm and maximum stability is maintained by using C4. At the last point, it increased again and reached to 1.4437 mm. Besides of the slight differences, deviation has not been observed between Case 4.2 and Case 4.3. Comparison on sub-cases plotted in Figure 4-22.

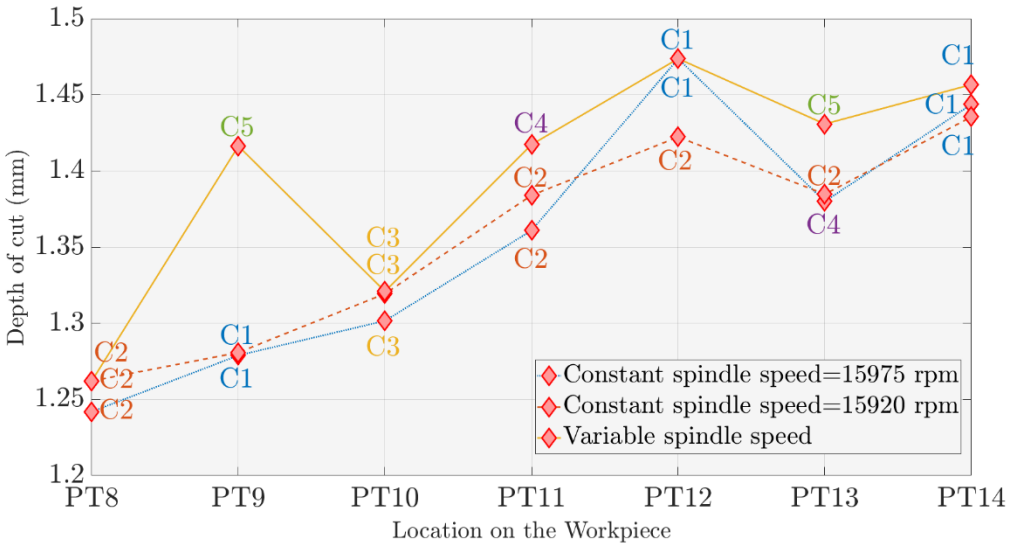

Figure 4-22: Comparison on different spindle speeds at maximum stability — in CASE 4 in Y direction

Comparative study has been conducted for exploring stability variations between sub-cases which can be described as variable spindle speed in Case 4.1 for without any restriction on rotation of the redundant axis, constant spindle speed adjusted to 15920 rpm in Case 4.2, and constant spindle speed adjusted to 15975 rpm in Case 4.3. Most improved stability conditions are observed in Case 4.1 especially when robot configuration switches from the C2 to C5 and C1 to C5. Although a significant improvement is observed in first switch between PT8 and PT9, redundant axis should rotate around 135° to maintain stability. Furthermore, another improvement is observed in PT13 at C5. However, robot's redundant axis rotation is at the maximum level and it should rotate 180° to achieve the improved stability conditions. This maximum rotation case, Case 4.1, might be dangerous due to excessive rotation in a shortest path.

4.6 CASE 5: Maximum stability in Y direction with rotation constraint

The same procedure, which is applied to CASE 2 in terms of restrictions of the configuration variation, is followed in this case. Limited rotations between C2 and C4 configurations are taken into account to reveal chatter characteristics along the tool path. Therefore, stability limits are evaluated for each configuration staying in the rotation boundaries with respect to the locations on the workpiece.

4.6.1 Case 5.1: Maximum stability in Y direction without rotation – Variable spindle speed

Based on chatter stability evaluations, a sequence is generated without any spindle speed adjustments. This sequence is plotted in Figure 4-23. Following sequence is sorted as C2, C2, C3, C4, C4, C4 and C2 with accompanying spindle speeds that 15920 rpm, 15925 rpm, 15915 rpm, 16055 rpm, 16050 rpm, 16020 rpm and 15880 rpm, respectively.

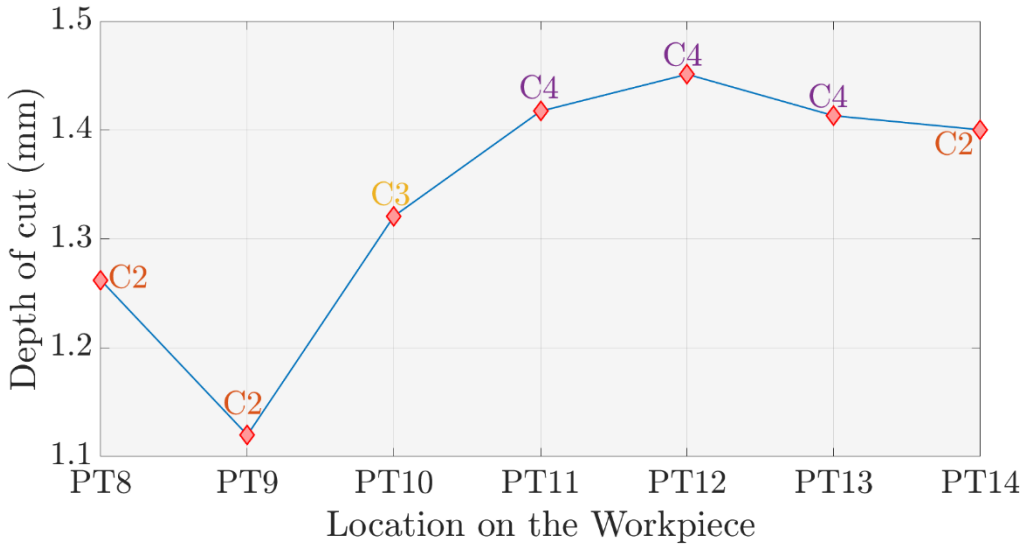

Figure 4-23: Configuration identification based on maximum stability along the tool path regarding variable spindle speed & configuration constraints in Y direction

In the Figure 4-23, stability limitations are plotted. Highest maximum depth of cut is observed at C4 in PT12 where the lowest maximum depth of cut is observed at C2 in PT9 where the highest cutting depth is among the alternatives between C2 and C4. In this sequence, related cutting depths can be sorted as: 1.2621 mm, 1.1198 mm, 1.3209 mm, 1.4173 mm, 1.4512 mm, 1.4131 and 1.4002 mm, respectively. In this case, in terms of maximum stability, maximum reachable cutting depth dropped from 1.2621 mm to 1.1198 mm compared to Case 4.1 in terms influences of rotation limits on stability diagrams.

4.6.2 Case 5.2: Maximum stability in Y direction with rotation constraint – Constant spindle speed (15925 rpm)

In this case, limited rotation is used to generate sequence between C2 and C4 configurations, which is half of the maximum rotation, and selection has been carried out by taking constant spindle speed adjustment into the consideration. Based on maximum stability evaluation among limited configuration variation, the sequence can be written C2, C1, C3, C2, C2, C2 and C1 in the form of configuration and it is plotted in the Figure 4-24.

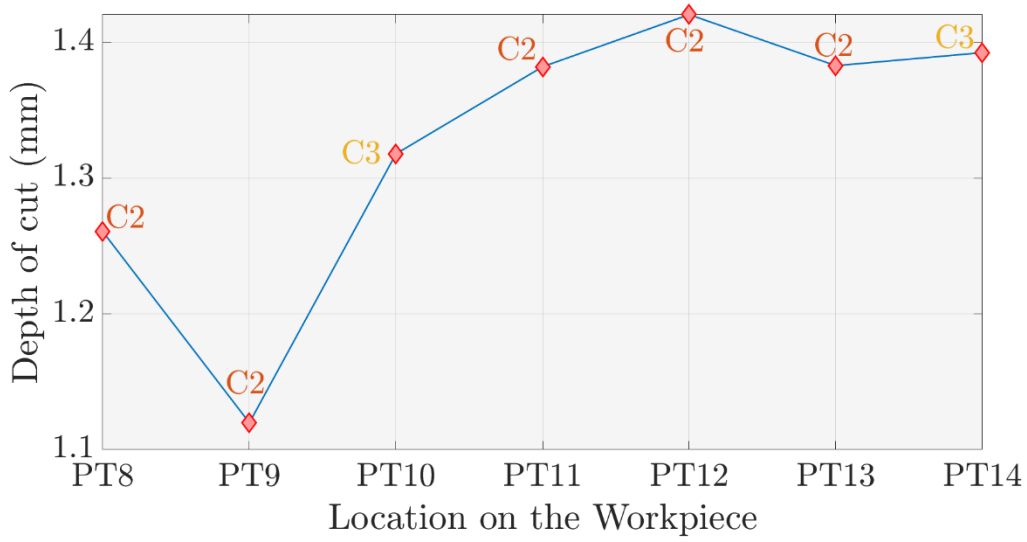

Figure 4-24: Variation in stability with respect to limited configuration variation between C2—C4 at 15925 rpm in Y direction

When spindle speed adjusted to 15925 rpm, maximum allowable cutting depths are varied and this variation can be explained as 1.2605 mm, 1.1198 mm ,1.3178 mm, 1.3819 mm, 1.4203 mm ,1.3827 mm and 1.3923 mm with respect to order of locations on the workpiece in terms of cutting depths. A huge decrement has observed when robot moves towards the PT9. In this case, the restrictive depth of cut is identified at the second location on the workpiece and limiter cutting depth is observed as 1.1198 mm. In this case, same trends are observed compared to Case 5.1.

4.6.3 Case 5.3: Maximum stability in Y direction with rotation constraint – Constant spindle speed (16050 rpm)

Spindle speed adjusted to 16050 rpm which has the highest maximum stability among the other configuration-location pairs. The sequence is generated by taking into consideration of this spindle speed. Results are plotted in Figure 4-25 and it is sorted as C3, C2, C3, C4, C4, C4, C3. In this manner, configuration structure has changed compared to Case 5.2.

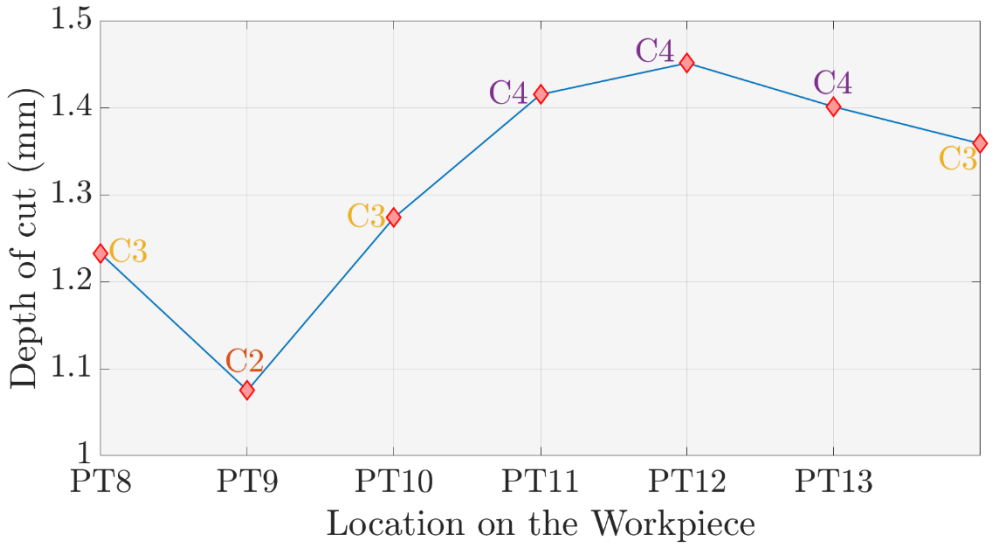

Figure 4-25: Variation in stability with respect to limited configuration variation between C2—C4 at 16050 rpm in Y direction

Maximum allowable cutting depths are 1.232 mm,1.075 mm,1.2735 mm,1.4151 mm,1.4512 mm,1.4010 mm, and 1.3586 mm. In this sequence, C2 at PT9 is the limiter one for the constant cutting depth. A meaningful stability reduction has observed when the robot reached PT9 whereas in Case 5.2. Therefore, the limiter for the constant depth of cut is identified as 1.075 mm at PT9, C2. However, this sequence starts with C3 and continues with the C2, C3, and rotation switched from C3 to C4 and ends with C3 for an increased stability approach.

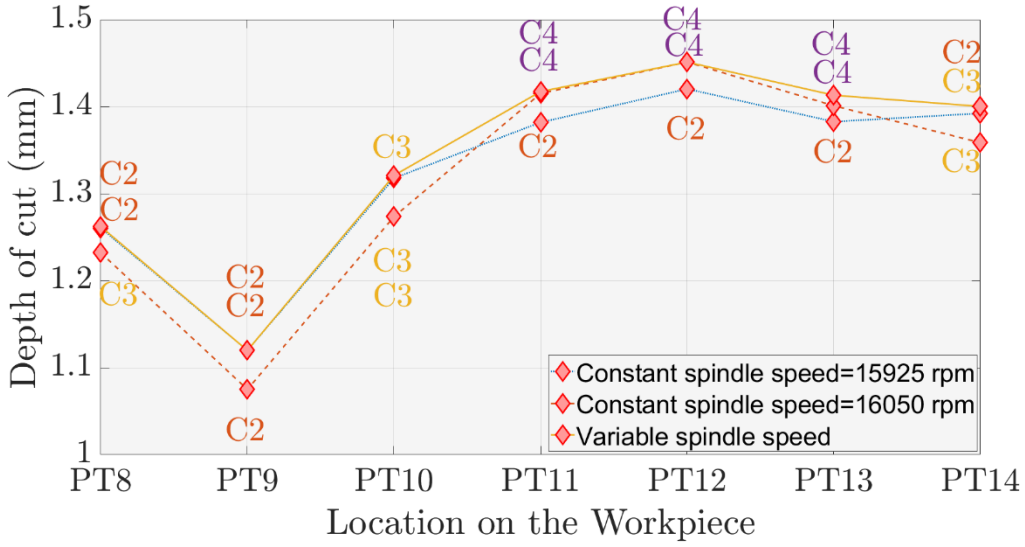

Figure 4-26: Comparison on different spindle speeds at maximum stability

In the, sub cases are compared in terms of improved stability and configurational structure along the tool path. Most improved stability is Case 5.1 in which no restriction on spindle speed is applied. All subcases are close to each other and Although all subcases are close to each other, changes in configuration structure is observed at 16050 rpm. Same trend has been preserved as shown in Figure 4-26.

4.7 CASE 6: Maximum stability in Y direction without rotation

Same procedure is followed in the CASE 3, a sequence without rotation is generated to distinguish the differences between CASE 4, which maximum rotation is allowed, CASE 5, which limited rotation is allowed and CASE 6, which rotations are not allowed. In this manner, C3 is selected as the fulcrum configuration to carry out comparative study about stability limits in terms of configurational and positional dependency which is introduced by selecting constant configuration along the tool path. However, it is needed to investigate stability characteristics along the tool path under variable and constant spindle speed limitations.

4.7.1 Case 6.1: Maximum stability in Y direction without rotation – Variable spindle speed

A sequence is generated to compare maximum stabilities without changing the configuration of the robot. Configuration kept at same throughout the tool path, positional dependency of the robot's structure on tool tip dynamics is analyzed. In this manner, cutting depths are analyzed and identified along the tool path and plotted in Figure 4-27.

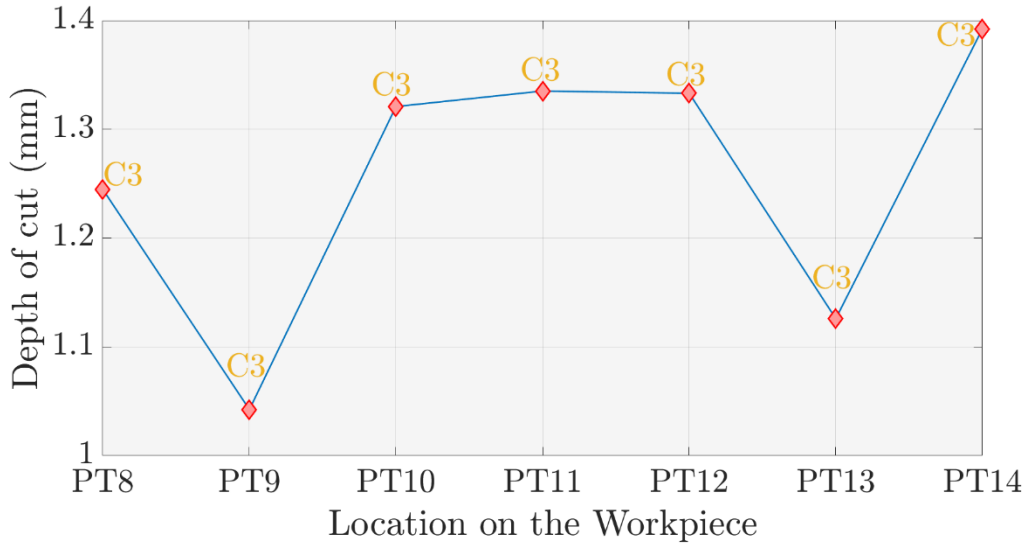

Figure 4-27: Representative plot on maximum stability along the tool path regarding variable spindle speed & position effect at C3 configuration in Y direction

In Y direction at C3, depth of cuts are 1.2448 mm, 1.0424 mm, 1.3209 mm, 1.3352 mm, 1.3331 mm, 1.1259 mm and 1.3923 mm with respect to the predefined points on the tool path with respect to order of locations on the workpiece. Maximum allowable cutting depth reduced in two different locations at PT9 and PT13, respectively. At PT13, maximum allowable depth dropped from the 1.3331 mm to 1.1259 mm. However, more reduction has been observed when robot's tool tip dynamics measured at PT9. Cutting depth reduced from 1.2448 mm to 1.0424 mm. Henceforward, limiter depth is identified as 1.0424 mm which is located at PT9.

4.7.2 Case 6.2: Maximum stability in Y direction without rotation – Constant spindle speed (15915 rpm)

In this case, constant spindle speed adjusted to 15915 rpm which has the lowest stability among other alternatives. When spindle speed is selected as constant, maximum cutting depths are plotted in Figure 4-28 explore the effect of constant spindle speed.

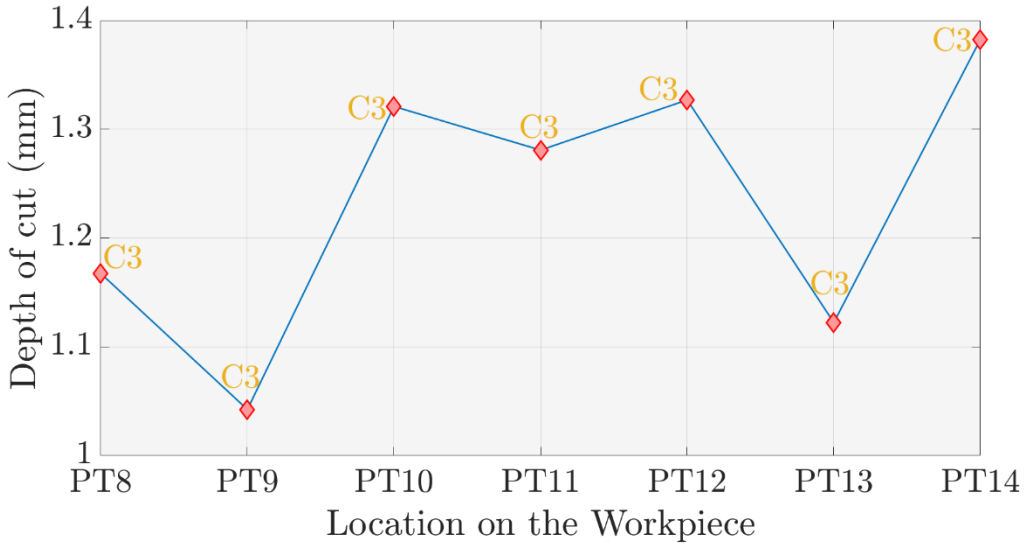

Figure 4-28: Representative plot on maximum stability along the tool path regarding variable constant spindle speed at 15915 rpm & position effect at C3 configuration in Y direction

These cutting depths are 1.1674 mm, 1.0424 mm, 1.3209 mm, 1.2808 mm, 1.3268 mm, 1.1223 mm and 1.3825 mm with respect to the order of locations on the workpiece. Stability limits and related cutting depths are reduced in two different locations. First, a drop occurred when robot reaches the PT9 and cutting depth is reduced from 1.1674 mm to 1.0424 mm which is appeared as the lowest one along tool path. Second, another drop observed in PT13 in where cutting depth reduced from 1.3286 mm to 1.1223 mm. Finally,

second reduced depth of cut is higher than the first one. In this manner, restrictive depth of cut is identified as 1.0424 mm at PT9.

4.7.3 Case 6.3: Maximum stability in Y direction without rotation – Constant spindle speed (15925 rpm)

Spindle speed adjusted to 15925 rpm which has the highest maximum depth of cut value among the other configuration-location pairs for better understanding the behavior of the chatter characteristics along the tool path. This sequence is shown in Figure 4-29.

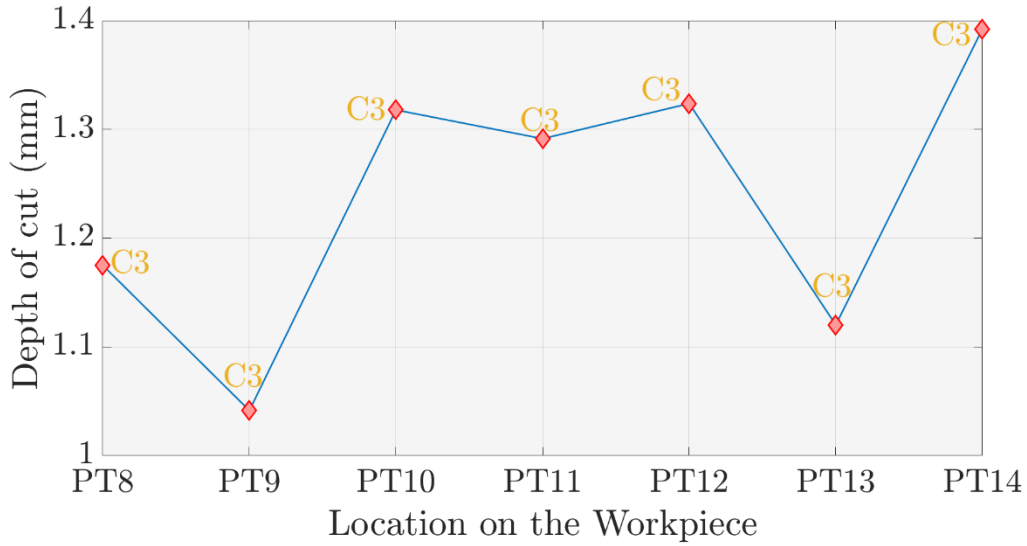

Figure 4-29: Representative plot on maximum stability along the tool path regarding variable constant spindle speed at 15925 rpm & position effect at C3 configuration in Y direction

In this case, cutting depths are 1.175 mm, 1.042 mm, 1.318 mm, 1.291 mm, 1.324 mm, 1.120 mm and 1.392 mm with respect to order of locations on the workpiece. As in Case 6.2, considering the minor difference between the spindle speeds, two different reduced cutting depths are observed around same locations. First drop occurred at PT9 where the second drop occurred at PT13. However, as in Case 6.2, reduced stability limit in PT13 is still higher than PT9. Therefore, aiming constant depth of cut, limiter depth is identified as 1.042 mm as in Case 6.2.

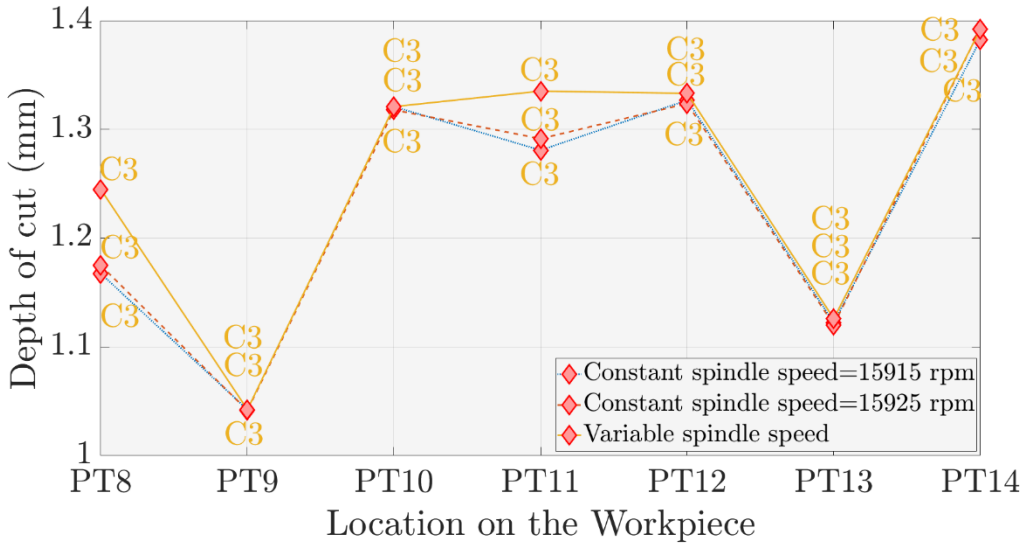

Figure 4-30:Comparison on different spindle speeds at maximum stability under constant configuration condition —C3 in Y direction

In the Figure 4-30, sub cases are compared in terms of improved stability under constant configuration criteria. Most improved stability observed in Case 6.1 in which no restriction on spindle speed is applied. Although all subcases are close to each other, at constant spindle speed cases, which are Case 6.2 and Case 6.3, maximum allowable cutting depth is slightly reduced. However, these reductions can be negligible due to the less rigid structure of the industrial robots.

4.8 Results and Discussion

6 different cases, 3 cases for each direction, are generated to obtain better understanding of the chatter characteristics and related cutting depths due to robot's position and configuration. 3 sub-cases are generated for each case to explore the effect of spindle speeds on the stability limits for the robotic milling operation depending on selection of the highest stability provided by the position and configuration. Therefore, to observe the variation between each case and accompanying sub-cases, comparative study is carried out and differences are plotted in Figure 4-31.

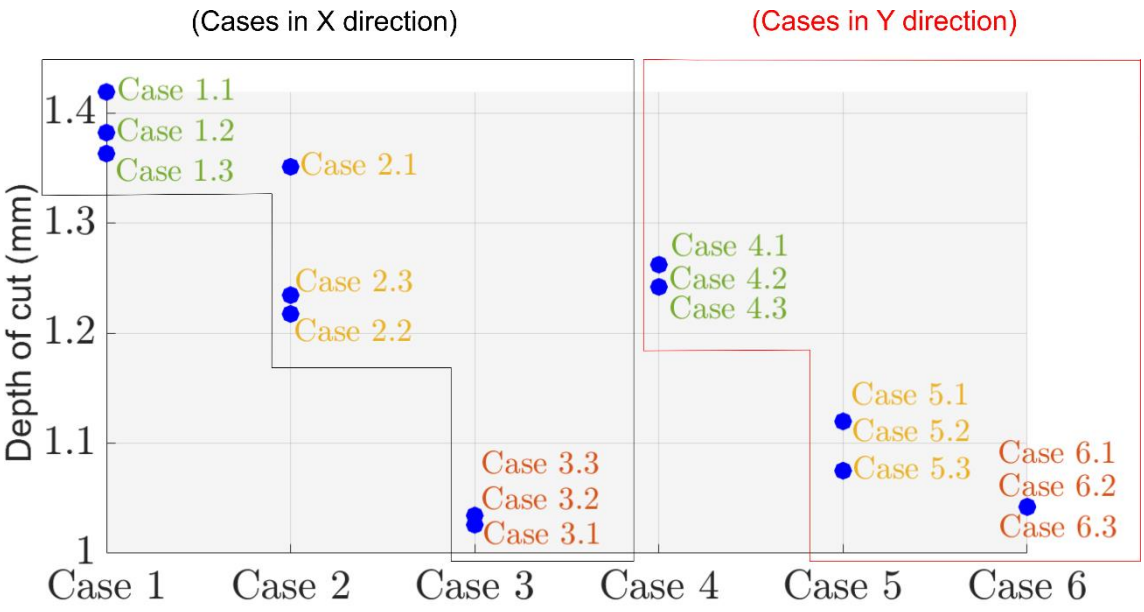

Figure 4-31: Comparison on Cases in terms of maximum allowable cutting depth

In Figure 4-31, maximum allowable cutting depths are plotted to present variation between cases and subcases regarding to different configuration sequences. Case 1 is the most beneficial one in terms of improved stability limits. In the subcases of Case 1, some minor deviations are observed due to constant spindle speed constraints. Case 1 painted green due to it has the most improved stability limits. Case 2 is placed in the middle among the cases in X direction due to limited rotation which is half of the maximum rotation and painted orange to indicate that neither it has the most improved stability conditions nor the lowest stability. A meaningful difference is observed between Case 2.1 and Case2.2, Case 2.3. Selected constant depth of cut is reduced from 1.351 mm to 1.2174 mm and 1.2344 mm at Case 2.2 and Case 2.3, respectively. In this manner, the maximum allowable cutting depth is reduced around 11% compared to Case 2.2 and it is reduced by approximately 9.4% compared to Case 2.3. Lowest stability conditions are satisfied in Case 3 and painted red. Considering all the sub-cases, the difference between Case 1 and Case 3 is significant. In Case 3, limiter depth was 1.0343 mm at the highest configuration-spindle speed pair and 1.419 mm was the determiner for Case 1.1 which was satisfying the most improved stability. The maximum cutting depth is reduced around %37.2 compared to Case 3. In Y direction, the same painting procedure is used to distinguish the most improved, middle improved, and lowest improved stability conditions. Case 4 has a maximum cutting depth in terms of improved stability. This case is followed by Case 5 which is a limited rotation case. Then, the specific lowest case is identified as Case 6 which no rotation is allowed. According to spindle speed constraints which comprises

sub-cases, no meaningful difference is observed. The highest depth of cut was identified as 1.2621 mm in Case 4, and the highest cutting depth was identified as 1.042 mm at Case 6 which is the lowest among other alternatives in Y direction. In this manner, stability is reduced around %21.2 compared to Case 6. After giving the comparisons, it is deduced that spindle speed variation provides higher stability limits than the constant case. According to simulation results, using the lowest maximum depth of cut with variable spindle speeds is acceptable. However, in the practical implementation of the utilization of redundant axis, stable cutting conditions might be violated due to robot errors related to coupled motion to track the straight path. To prevent this violence and avoid undesired shifts in maximum allowable cutting depths, influential constraints (redundant link rotation, spindle speed variation) should be taking into consideration along the entire tool path. Simulation results have been demonstrated the effects of the spindle speed in each case with related configuration as well as the effects of the positional and configurational dependency. Stability for high-speed cutting is not influenced due to positional dependency when the configuration effect is applied and taking into consideration. In the scope of position effect, certain configurations were found to be superior to others in terms of stability with accompanying material removal rate. These superior configurations are C1, C2, C5, and inferior configurations are C4 and C3, respectively, in the X-direction. In Y direction, superior configurations are C1, C2, C5, and inferior configurations are C4 and C3, respectively. According to this evaluation, if configuration selection is obstacle-free which means there should not be any kind of physical object that can cause a collision when the robot is rotating, C1, C2, and C5 should be used to maintain increased stability in both directions. Productivity limits are close by between 3 superior configurations. Therefore, the selection of one the superiors will have an approximately similar impact on productivity and selection of the best configuration sequence is essential to improve stability beyond of the positional effects.

4.9 Summary

In this chapter, as well as the impact of positional dependency on tool tip dynamics, effects of the robot configuration on the tool tip dynamics and milling stability are analyzed through FRF measurements and stability simulations. Maximum stability limits are utilized as a correlation paradigm for determination of the robot configuration all through the tool path. In this way, preferable configurations along large region tool paths

may should be chosen dependent on the absolute stability limits. Rather than changing workpiece place and generated tool path, configuration can be changed on the same workspace and milling operation continues processing within the range of predetermined stability limits. Positional dependency of stability limits in robotic milling is well-known, which can be compensated by changing the robot configuration as demonstrated in this thesis. Even at the same position, robot can be eluded from the chatter vibration by using different configuration as it influences the tool tip dynamics.

CHAPTER 5 Conclusions

5.1 Conclusions

Industrial robots are used more and more for the manufacturing of large parts made of lightweight materials like aluminum, fiber-reinforced plastics, or composites such as large frames in aerospace or automotive industries. Industrial robots might be an alternative to conventional machine tools for machining of fiber-reinforced materials or metals, yet dynamic performance needs to be improved for the use in cutting operations due to effects on the machining stability. Prediction of the natural frequencies based on robot dynamics and preventing chatter or chatter avoidance still are challenging issues for robotic milling applications with improved stable cutting conditions. In this thesis, different dynamic modeling approaches of the industrial robots with their basics and comparison of the computation time are given by using MATLAB© symbolic toolbox and parallelization of the algorithms. Lagrange-Euler based robot dynamics with the construction of the inertia matrix is given and natural frequency identification is elaborated. The alternative approach to increase chatter stability limits by using the redundant axis rotation of the 6-axis industrial robot is presented. Within the scope of the natural frequency identification analysis based on robot dynamics, 1st mode experimental results and theoretical results are diverging in the most stretched form, converging in the middle posture, and another deviation is observed towards the last predefined posture of the robot. 2nd mode theoretical and experimental theoretical result trends are similar with lower values in terms of the natural frequencies except for the transition between most stretched form (1st pose) and the 2nd pose of the robot. Later, an alternative approach was developed for a wider use of industrial robots in machining operations. In the scope of the proposed approach, besides of the positional effects on the tooltip dynamics, configuration effects are included to improve stable cutting conditions for robotic milling operations by using redundant axis utilization as a functional tool. Maximum stability

limits, rotation of the redundant axis, spindle speed variations are used as criteria to explore the effects of the different configurations in conjunction with position effects. Thus, positional dependency and configurational dependency are evaluated along the tool path with different constant and variable spindle speeds based on the impact hammer tests and stability lobe diagrams. Then, a comparative study is carried out to evaluate the importance of the spindle speeds with configuration assessment in terms of maximum stability due to deviation and variation in FRF results and tool modes. Henceforth, this approach demonstrates the importance of the variable spindle speeds, constant spindle speeds, and accompanying configurations to maintain improved stability conditions.

These effects can be sorted into 3 main groups:

- Positional effect contributed by variation in the joint configuration of the robot

- Configuration effect contributed by utilized usage of the redundant axis

- Variable spindle speed and constant spindle speed differences in terms of configuration and maximum allowable depth of cut

As a result, simulation analysis demonstrates a trade-off between configuration selection and improved productivity. Instead of placing the workpiece in a different location and applying the modification on tool path or cutting parameters, the proposed approach can be beneficial for maintaining the stability of the robotic milling operation stability, moreover, the stability of the robotic milling operations can be increased using the proposed approach.

5.2 Contributions

The contributions are listed as the following,

- Fast calculation of the robot dynamics calculation based on the Euler Lagrange approach is studied with the identification of the natural frequencies after giving the basic role of the equations with pros and cons.
- An extensive research on the effects of the position and configuration of the robot on the tooltip dynamics and milling stability is carried out along the tool path in conjunction with other influential effects such as spindle speed and restricted utilization of the redundant axis progressive points on the tool path based on experimental results.

- A novel approach to increase or maintain the possible highest stability limits in robotic milling applications is presented by using the redundant link utilization concept of the 6-axis industrial robots as a beneficial tool.
- A programming framework is given based on experimental results and post-process and re-modification of the redundant link utilization to generate preferable configuration sequences.

5.3 Future Work

The potential research topics are given in the following,

- Dynamic parameter identification and gravity compensator modeling for accurate dynamic simulations of the industrial robot and enabling the accurate predictions of the dynamic behavior of the robots are yet to be well-investigated. TCP FRFs and chatter frequencies could be predictable.
- The redundant link utilization approach can be used for low-speed milling operations via extending the concept with variable depth of cut. A module can be developed to program robots for metal cutting operations considering the proposed approach.
- An optimization framework can be applied to combine the effect of tooltip dynamics, robot dynamics, and stiffness properties for the broader utilization of the industrial robots for the machining field.
- Robust programming approaches for robot dynamics can be investigated and performed to facilitate model-based control strategies.
- To predict chatter, FRFs can be predicted with extensive data sets by using machine learning algorithms that can be useful and novel.

Bibliography

[1]Chen, Yonghua, and Fenghua Dong. "Robot machining: recent development and future research issues." The International Journal of Advanced Manufacturing Technology 66.9-12 (2013): 1489-1497.

[2]Pandilov Z, Dukovski V. Comparison of the characteristics between serial and parallel robots. Acta Technica Corvininesis-Bulletin of Engineering. 2014; 7(1).

[3]Dumas, Claire, et al. "Joint stiffness identification of industrial serial robots." Robotica 30.4 (2012): 649-659.

[4]Iglesias, I., M. A. Sebastián, and J. E. Ares. "Overview of the state of robotic machining: Current situation and future potential." Procedia engineering 132 (2015): 911-917.

[5]Schneider, Ulrich, et al. "Improving robotic machining accuracy through experimental error investigation and modular compensation." The International Journal of Advanced Manufacturing Technology 85.1-4 (2016): 3-15.

[6]He, Jianmin, Zengxi Pan, and Hui Zhang. "Adaptive force control for robotic machining process." 2007 American Control Conference. IEEE, 2007.

[7]Vulliez, Margot, Sylvain Lavernhe, and Olivier Bruneau. "Dynamic approach of the feedrate interpolation for trajectory planning process in multi-axis machining." The international journal of advanced manufacturing technology 88.5-8 (2017): 2085-2096.

[8]Quintana G, Ciurana J. Chatter in machining processes: A review. International Journal of Machine Tools and Manuf. 2011; 51(5):363-76.

[9]Oki Y, Kanitani K. Development of robot machining system for aluminium building materials. J JSME. 1996; 99(937):78-87.

[10]Pan Z, Zhang H, Zhu Z, Wang J. Chatter analysis of robotic machining process. Journal of materials processing technology 2006; 173(3):301-9.

[11]Tunc LT, Shaw J. Experimental study on investigation of dynamics of hexapod robot for mobile machining. The International Journal of Advanced Manufacturing Technology 2016; 84(5-8):817-30.

[12]Tunc, L. T., and Dave Stoddart. "Tool path pattern and feed direction selection in robotic milling for increased chatter-free material removal rate." The International Journal of Advanced Manufacturing Technology 89.9-12 (2017): 2907-2918.

[13]Tunc, Lutfi Taner, and Jay Shaw. "Experimental study on investigation of dynamics of hexapod robot for mobile machining." The International Journal of Advanced Manufacturing Technology 84.5-8 (2016): 817-830.

[14]Bisu C, Cherif M, Gérard A, K'nevez JY. Dynamic behavior analysis for a six-axis industrial machining robot. In Advanced Materials Research 2012 (Vol. 423, p. 65-76). Trans Tech Publications.

[15]Mejri S, Gagnol V, Le TP, Sabourin L, Ray P, Paultre P. Dynamic characterization of machining robot and stability analysis. The International Journal of Advanced Manuf. Tech. 2016; 82(1-4):351-9.

[16]Li J, Li B, Shen N, Qian H, Guo Z. Effect of the cutter path and the workpiece clamping position on the stability of the robotic milling system. The International Journal of Advanced Manufacturing Technology 2017; 89(9-12):2919-33.

[17]Bauer J, Friedmann M, Hemker T, Pischan M, Reinl C, Abele E, von Stryk O. Analysis of industrial robot structure and milling process interaction for path manipulation. In Process Machine Interactions 2013; p. 245-263. Springer, Berlin, Heidelberg.

[18]Zhang H, Wang J, Zhang G, Gan Z, Pan Z, Cui H, Zhu Z. Machining with flexible manipulator: toward improving robotic machining performance. In Proceedings, 2005 IEEE/ASME International Conference on Advanced Intelligent Mechatronics. 2005; p. 1127-1132. IEEE

[19]Guo, Yingjie, Huiyue Dong, and Yinglin Ke. "Stiffness-oriented posture optimization in robotic machining applications." Robotics and Computer-Integrated Manufacturing 35 (2015): 69-76.

[20]Abele, Eberhard, Matthias Weigold, and Stefan Rothenbücher. "Modeling and identification of an industrial robot for machining applications." CIRP annals 56.1 (2007): 387-390.

[21]Liu, Zhao, et al. "Comparison of finite element and experimental modal analysis of multi-joint flexible robotic arm." 2017 International Conference on Mechanical, System and Control Engineering (ICMSC). IEEE, 2017.

[22]Zhang, Jiabo, et al. "Optimization of Comprehensive Stiffness Performance Index for Industrial Robot in Milling Process." 2019 IEEE 10th International Conference on Mechanical and Aerospace Engineering (ICMAE). IEEE, 2019.

[23]Hao, Daxian, et al. "Experimental study of stability prediction for high-speed robotic milling of aluminum." Journal of Vibration and Control 26.7-8 (2020): 387-398.

[24]Sui, Shaochun, et al. "Study on Improving Accuracy in Robotic Milling of Aluminum Alloy." ASME 2018 13th International Manufacturing Science and Engineering Conference. American Society of Mechanical Engineers Digital Collection, 2018.

[25]Cordes, Marcel, Wolfgang Hintze, and Yusuf Altintas. "Chatter stability in robotic milling." Robotics and Computer-Integrated Manufacturing 55 (2019): 11-18.

[26]Wang, Guifeng, et al. "Chatter mechanism and stability analysis of robotic boring." The International Journal of Advanced Manufacturing Technology 91.1-4 (2017): 411-421.

[27]Denkena, Berend, and Thomas Lepper. "Enabling an industrial robot for metal cutting operations." Procedia CIRP 35 (2015): 79-84.

[28]Özer, Abdullah, et al. "Delaying tool chatter in turning with a two-link robotic arm." Journal of Sound and Vibration 332.6 (2013): 1405-1417.

[29]Sun, Lianjun, et al. "Investigation on chatter stability of robotic rotary ultrasonic milling." Robotics and Computer-Integrated Manufacturing 63 (2020): 101911.

[30]He, Feng-xia, Yu Liu, and Kuo Liu. "A chatter-free path optimization algorithm based on stiffness orientation method for robotic milling." The International Journal of Advanced Manufacturing Technology 101.9-12 (2019): 2739-2750.

[31]Mousavi, Said, et al. "Dynamic modeling and stability prediction in robotic machining." The International Journal of Advanced Manufacturing Technology 88.9-12 (2017): 3053-3065.

[32]Mousavi, S., et al. "Model-based stability prediction of a machining robot." New advances in mechanisms, mechanical transmissions and robotics. Springer, Cham, 2017. 379-387.

[33]Mousavi, Said, et al. "Control of a multi degrees functional redundancies robotic cell for optimization of the machining stability." Procedia CIRP 58.1 (2017): 269-274.

[34]Mousavi, Said, et al. "Stability optimization in robotic milling through the control of functional redundancies." Robotics and Computer-Integrated Manufacturing 50 (2018): 181-192.

[35]Gienke, Orm, et al. "Mode coupling chatter prediction and avoidance in robotic machining process." The International Journal of Advanced Manufacturing Technology 104.5-8 (2019): 2103-2116.

[36]Yuan, Lei, et al. "Mode coupling chatter suppression for robotic machining using semi-active magnetorheological elastomers absorber." Mechanical Systems and Signal Processing 117 (2019): 221-237.

[37]Cen, Lejun, et al. "A method for mode coupling chatter detection and suppression in robotic milling." Journal of Manufacturing Science and Engineering 140.8 (2018).

[38]Cen, Lejun, and Shreyes N. Melkote. "CCT-based mode coupling chatter avoidance in robotic milling." Journal of Manufacturing Processes 29 (2017): 50-61.

[39]Denavit J. A kinematic notation for low pair mechanisms based on matrices. ASME J. Appl. Mech. 1955; 22:215-21.

[40]Altintas Y, Budak E. Analytical prediction of stability lobes in milling. CIRP annals. 1995; 44(1):357-62.

[41]Pérez R, Gutiérrez SC, Zotovic R. A study on robot arm machining: advance and future challenges. Annals of DAAAM & Proceedings 2018; 29.

[42]Tsai, Lung-Wen. Robot analysis: the mechanics of serial and parallel manipulators. John Wiley & Sons, 1999.

[43]Sciavicco, Lorenzo, and Bruno Siciliano. Modelling and control of robot manipulators. Springer Science & Business Media, 2012.

[44]Spong, Mark W., and Mathukumalli Vidyasagar. Robot dynamics and control. John Wiley & Sons, 2008.

[45]Deshpande, Vivek A., and Anurag B. Verma. "Dynamics of Robot Manipulators: A Review." International Journal of Engineering 3.3 (2010): 603-606.

[46]Fu, King Sun, Ralph Gonzalez, and CS George Lee. Robotics: Control Sensing. Vis. Tata McGraw-Hill Education, 1987.

[47]Hollerbach, John M. "A recursive lagrangian formulation of maniputator dynamics and a comparative study of dynamics formulation complexity." IEEE Transactions on Systems, Man, and Cybernetics 10.11 (1980): 730-736.

[48]Luh, John YS, Michael W. Walker, and Richard PC Paul. "On-line computational scheme for mechanical manipulators." (1980): 69-76.

[49]A. K. Bejczy and R. P. Paul, "Simplified robot arm dynamics for control," 1981 20th IEEE Conference on Decision and Control including the Symposium on Adaptive Processes, San Diego, CA, USA, 1981, pp. 261-262, doi: 10.1109/CDC.1981.269524.

[50]Walker, Michael W., and David E. Orin. "Efficient dynamic computer simulation of robotic mechanisms." (1982): 205-211.

[51]Featherstone, Roy, and David Orin. "Robot dynamics: equations and algorithms." Proceedings 2000 ICRA. Millennium Conference. IEEE International Conference on Robotics and Automation. Symposia Proceedings (Cat. No. 00CH37065). Vol. 1. IEEE, 2000.

[52]Featherstone, Roy. "Robot dynamics algorithms." (1984).

[53]Orin, David E., et al. "Kinematic and kinetic analysis of open-chain linkages utilizing Newton-Euler methods." Mathematical Biosciences 43.1-2 (1979): 107-130.

[54]Salisbury, J. Kenneth. "Active stiffness control of a manipulator in cartesian coordinates." Decision and Control including the Symposium on Adaptive Processes, 1980 19th IEEE Conference on. Vol. 19. IEEE, 1980.

[55]Theissen, Nikolas A., Theodoros Laspas, and Andreas Archenti. "Closed-force-loop elastostatic calibration of serial articulated robots." Robotics and Computer-Integrated Manufacturing 57 (2019): 86-91.

[56]Klimchik, Alexandr, et al. "Advanced robot calibration using partial pose measurements." 2013 18th International Conference on Methods & Models in Automation & Robotics (MMAR). IEEE, 2013.

[57]www.robotics.org,2020.

[58]www.spaziobelo.com, 2020.

[59]www.kuka.com, Kr 240 R2900 ,2020.

Appendix A Communication System Description

The communication system has been built for real-time data exchange between the laser tracker, robot, and computer. The connection between pc and NI Compact RIO 9038 device is provided by LAN cable. Then, an EtherCAT cable is connected to the port of the real-time module attached to the laser tracker. That cable provides communication between the laser tracker and the industrial pc. Another connection cable that provides communication between the robot and industrial pc should be connected to the EtherCAT bridge and the latter port should be connected by EtherCAT cable which carries information from the laser tracker. This EtherCAT bridge allows double-sided information exchange between laser tracker, robot, and computer. That schematic is shown in Figure A-1. Robot's controller (KRC4) working frequency is 500 Hz and the laser tracker controller's working frequency is 1000 Hz.

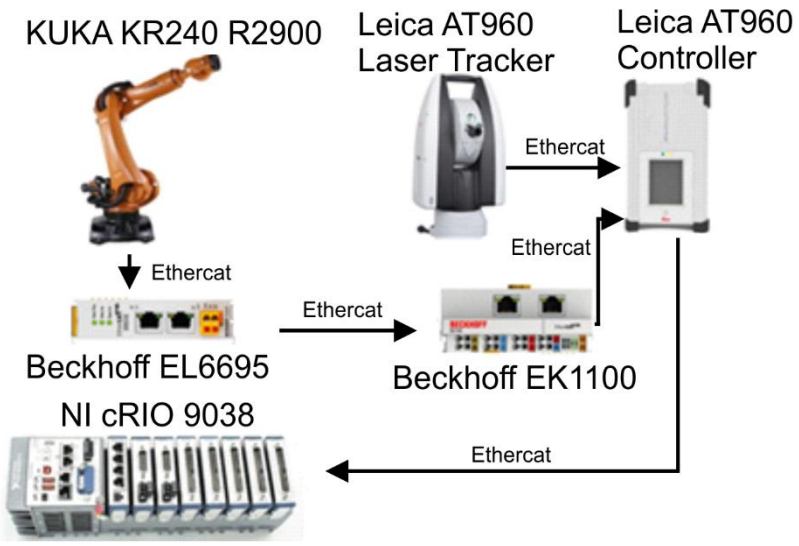

Figure A-1 :Connection and communication procedure for the laser tracker & robot & pc

Appendix B Cubic and Quintic Polynomial Trajectories

Cubic and quintic trajectory interpolations are generated in this appendix to apply robot mechanisms for computation time purposes. From this point of view, it is important to determine the joint trajectories and the angular positions to follow using a particular polynomial or the inverse kinematic solution for a cartesian trajectory, and to find velocities and accelerations according to the generated motion of the system. For this, it will be easy to start from the joint trajectory formed with the cubic polynomial first, and in addition to this, the angular positions, velocities, and accelerations of the joints can be found as a function of time, thus it will be facilitated to find the torque values according to the time. Cubic polynomial is written in terms of joint position, θ , in equation (100).

$$\theta(t) = \alpha_0 + \alpha_1 t + \alpha_2 t^2 + \alpha_3 t^3 \tag{100}$$

The derivation of the equation (100) provides the angular velocity of joints for the cubic trajectory. This velocity polynomial is expressed in the equation (101).

$$\dot{\theta}(t) = \alpha_1 + 2\alpha_2 t + 3\alpha_3 t^2 \tag{101}$$

Then, another derivation is applied to the joint velocity to find joint accelerations which is given in the equation (102).

$$\ddot{\theta}(t) = 2\alpha_2 t + 6\alpha_3 t \tag{102}$$

Initial conditions and final conditions are set to combine equations in terms of function of time and time dependent parameters.

$$\begin{aligned} \theta(0) &= \alpha_0 + \alpha_1 t_0 + \alpha_2 t_0^2 + \alpha_3 t_0^3 \\ \dot{\theta}(0) &= \alpha_1 + 2\alpha_2 t_0 + 3\alpha_3 t_0^2 \\ \theta(final) &= \alpha_0 + \alpha_1 t_f + \alpha_2 t_f^2 + \alpha_3 t_f^3 \\ \dot{\theta}(final) &= \alpha_1 + 2\alpha_2 t_f + 3\alpha_3 t_f^2 \end{aligned} \tag{103}$$

In this manner, the coefficient matrix and parameter vector can be written as a combination of the equations (103) to identify the parameters and joint acceleration which will be the function of time and the necessary matrix is given in equation (104).

$$\begin{bmatrix} 1 & t_0 & t_0^2 & t_0^3 \\ 0 & 1 & 2t_0 & 3t_0^2 \\ 1 & t_f & t_f^2 & t_f^3 \\ 0 & 1 & 2t_f & 3t_f^2 \end{bmatrix} \begin{bmatrix} \alpha_0 \\ \alpha_1 \\ \alpha_2 \\ \alpha_3 \end{bmatrix} = \begin{bmatrix} \theta(0) \\ \dot{\theta}(0) \\ \theta(final) \\ \dot{\theta}(final) \end{bmatrix} \quad (104)$$

The matrix form is defined as $Ra = c$ which represents the multiplication of time dependent parameters and coefficients. R is defined as coefficient matrix and a is defined as parameter vector where the c is defined as a vector that contains initial position and velocity with final position and velocity. Elements of c matrix are given as input parameters to define position, velocity and acceleration profile of the given single cubic trajectory by solving the matrix in terms of parameter vector as $a = R^{-1}c$ [44]. For that purpose, a single cubic trajectory is defined and plotted in Figure B-1.

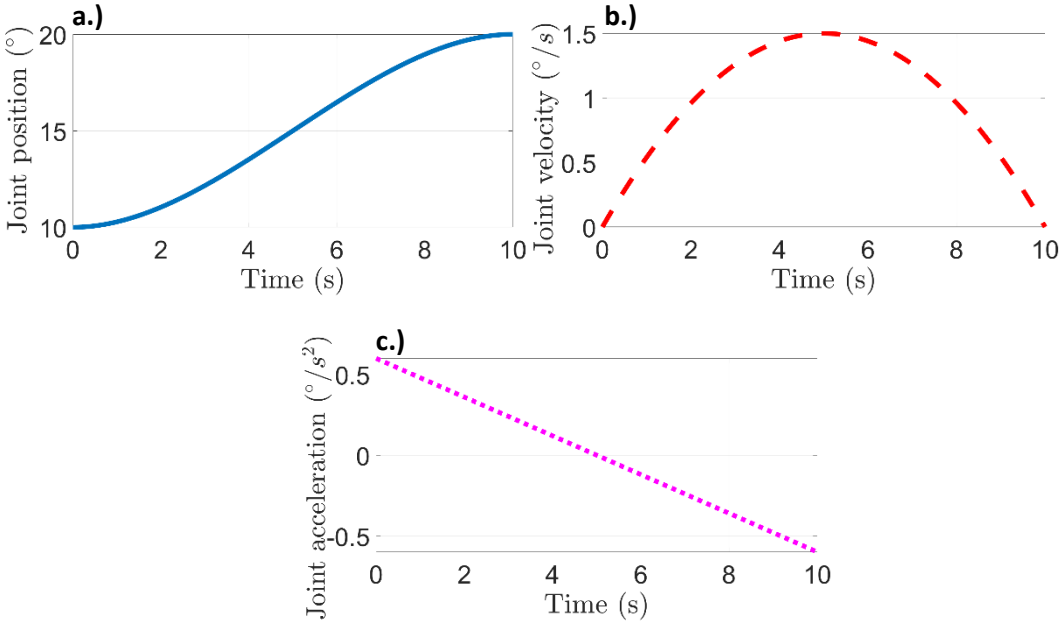

Figure B-1: (a) Joint position, (b)Joint velocity and (c) Joint acceleration variations in time intervals for single cubic polynomial

In Figure B-1, joint position variation is obtained as function of time. Joint position is started from 10° and ending at 20° which are given as input parameters for positional variation and velocity is defined 0 at starting point and final point for the trajectory. Velocity reached 1.5°/s at its peak point and velocity development of the cubic profile is plotted in Figure B-1(b). Later, acceleration profile is obtained, and acceleration is started with 0.6°/s^2 and decreased to 0 where the velocity reached its maximum and deceleration started to reduce the angular velocity of the joint until it reached 0. The acceleration development is plotted in Figure B-1(c). Hereafter, multiple cubic polynomials are used

to generate different trajectories between the different time intervals by using same formulation. In this manner, joint positions, velocities and accelerations are investigated for a multiple cubic polynomial. This polynomial is plotted in Figure B-2.

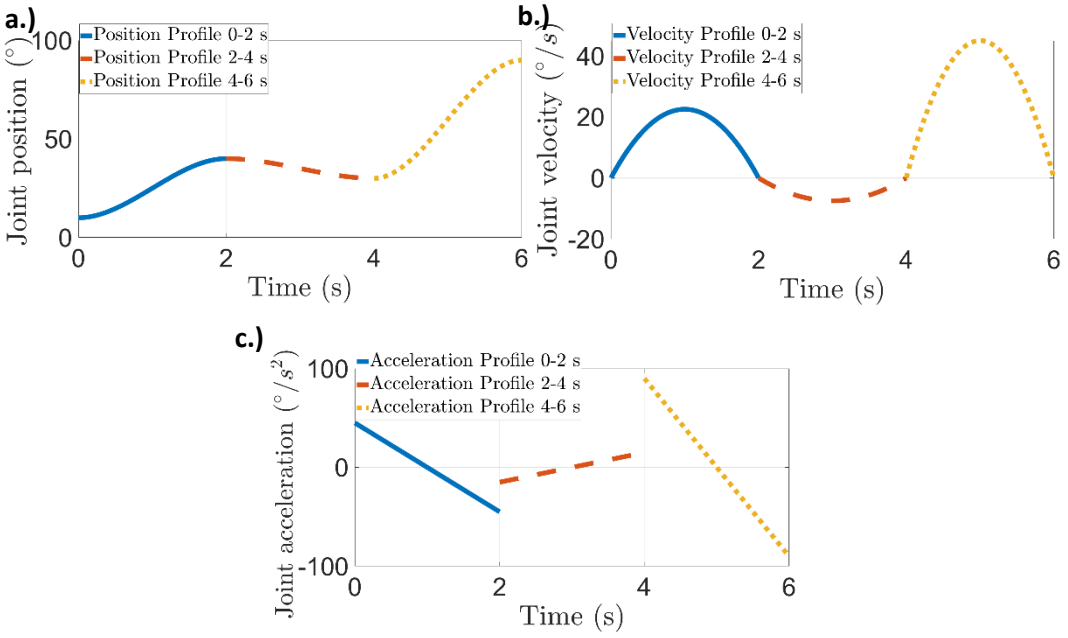

Figure B-2: (a) Joint position, (b)Joint velocity and (c) Joint acceleration variations in different time intervals for multiple cubic polynomial

In Figure B-2(a), joint position is changed from the 10° to 40° in 0-2 second interval and position is changed again from the 40° to 30° in 2-4 second interval, another position profile is added by changing the joint position from 30° to 90° in 4-6 second interval. The position profile variation is shown in Figure B-2(b). Then, Velocities are set as zero in the starting and ending at time intervals for each interval. Velocity profile is obtained as derivative of the joint positions and it is plotted in Figure B-2(c). In first time interval, acceleration is started from 45°/s^2 and ending at -45°/s^2. In second time interval, acceleration changed from -15°/s^2 to 15°/s^2. In the third and last interval deceleration is observed, and it is decreased from 90°/s2 to 0°/s^2, then it increased in opposite direction and reached to -90°/s^2. Another case is generated for quintic polynomial and formulation is explained for the quintic trajectory. First, joint position is written in terms of quintic polynomial equation. This formulation is given in the equation (105).

$$\theta(t) = \alpha_0 + \alpha_1 t + \alpha_2 t^2 + \alpha_3 t^3 + \alpha_4 t^4 + \alpha_5 t^5 \qquad (105)$$

Then, taking the derivation of the joint position with respect to time, angular velocity of the joint is obtained and presented in (106).

$$\dot{\theta}(t) = \alpha_1 + 2\alpha_2 t + 3\alpha_3 t^2 + 4\alpha_4 t^3 + 5\alpha_5 t^4 \tag{106}$$

As a next step, derivation of the joint velocity is taken to obtain acceleration equation in terms of quintic trajectory which is given in equation (107).

$$\ddot{\theta}(t) = \alpha_2 + 6\alpha_3 t + 12\alpha_4 t^2 + 20\alpha_5 t^3 \tag{107}$$

After deriving the acceleration from the velocity formulation in equation (106), initial conditions and terminal conditions are defined as a function of time. Initial and terminal conditions are given in terms of time dependent parameters to facilitate the creating matrices for coefficients and vectors for parameters. This equation series are given in equation (108) as a compact form.

$$\begin{gathered}
\theta(0) = \alpha_0 + \alpha_1 t_0 + \alpha_2 t_0^2 + \alpha_3 t_0^3 + \alpha_4 t_0^4 + \alpha_5 t_0^5 \\
\dot{\theta}(0) = \alpha_1 + 2\alpha_2 t_0 + 3\alpha_3 t_0^2 + 4\alpha_4 t_0^3 + 5\alpha_5 t_0^4 \\
\ddot{\theta}(0) = \alpha_2 + 6\alpha_3 t_0 + 12\alpha_4 t_0^2 + 20\alpha_5 t_0^3 \\
\theta(final) = \alpha_0 + \alpha_1 t_f + \alpha_2 t_f^2 + \alpha_3 t_f^3 + \alpha_4 t_f^4 + \alpha_5 t_f^5 \\
\dot{\theta}(final) = \alpha_1 + 2\alpha_2 t_f + 3\alpha_3 t_f^2 + 4\alpha_4 t_f^3 + 5\alpha_5 t_f^4 \\
\ddot{\theta}(final) = \alpha_2 + 6\alpha_3 t_f + 12\alpha_4 t_f^2 + 20\alpha_5 t_f^3
\end{gathered} \tag{108}$$

Combination of the equations are written as a matrix form to find coefficient matrix and parameter vector. This matrix creation is used for the solving parameters and this matrix form is given in the equation (109).

$$\begin{bmatrix}
1 & t_0 & t_0^2 & t_0^3 & t_0^4 & t_0^5 \\
0 & 1 & 2t_0 & 3t_0^2 & 4t_0^3 & 5t_0^4 \\
0 & 0 & 2 & 6t_0 & 12t_0^2 & 20t_0^3 \\
1 & t_f & t_f^2 & t_f^3 & t_f^4 & t_f^5 \\
0 & 1 & 2t_f & 3t_f^2 & 4t_f^3 & 5t_f^4 \\
0 & 0 & 2 & 6t_f & 12t_f^2 & 20t_f^3
\end{bmatrix}
\begin{bmatrix}
\alpha_0 \\ \alpha_1 \\ \alpha_2 \\ \alpha_3 \\ \alpha_4 \\ \alpha_5
\end{bmatrix} =
\begin{bmatrix}
\theta(0) \\ \dot{\theta}(0) \\ \ddot{\theta}(0) \\ \theta(final) \\ \dot{\theta}(final) \\ \ddot{\theta}(final)
\end{bmatrix} \tag{109}$$

The matrix form of the quintic trajectory is defined as $Ra = c$. In this manner, R represents the coefficients and a is written for the parameters and it is defined as parameter vector. c is given as input values to determine joint trajectory. In such a

purpose, matrix is solved analytically which is written in the form of $a = R^{-1}c$. A single quintic trajectory is defined and plotted in Figure B-3.

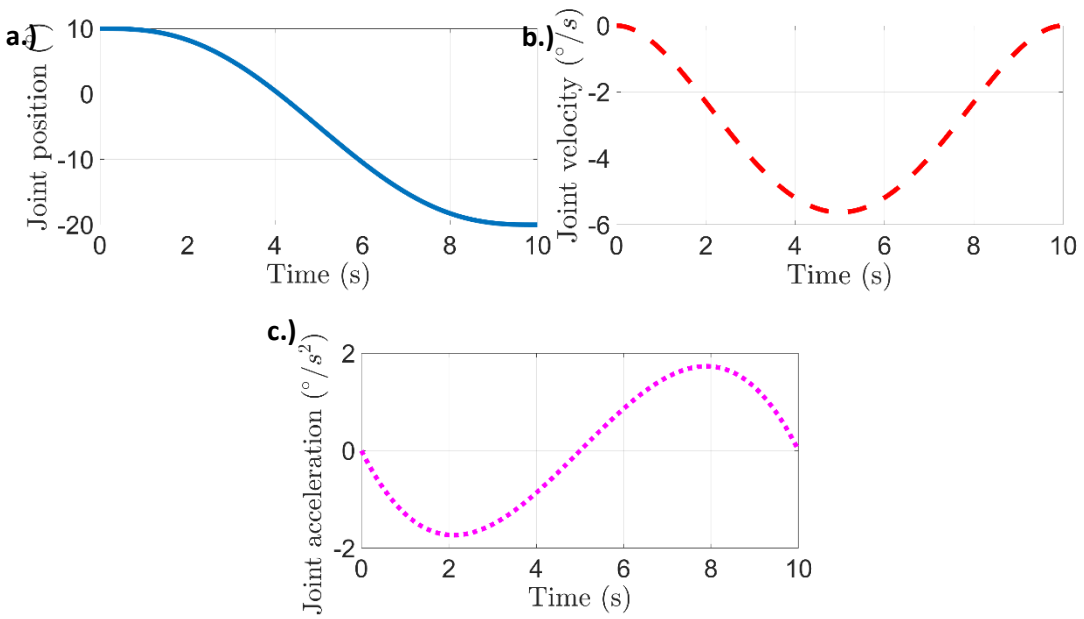

Figure B-3: (a) Joint position, (b)Joint velocity and (c) Joint acceleration variations in time intervals for single quintic polynomial

In Figure B-3(a), joint position variation is obtained as function of time for quintic trajectory. Joint position is started from 10° and ending at -20° which are given as input parameters for positional variation and initial and terminal velocities are defined as zero. Maximum velocity reached -5.625°/s in the middle of the predefined time zone as expected and velocity development of the quintic profile is plotted in Figure B-3(b). Later, initial and terminal conditions for acceleration is defined as zero to observe acceleration variation within 10 s time interval. Maximum acceleration is reached -1.732°/s^2 and decreased to 0 where the velocity reached its maximum and deceleration with opposite acceleration started to reduce the angular velocity of the joint. Maximum acceleration for opposite is reached to 1.732°/s^2 to decrease velocity and it is followed by deceleration until zero. Thus, acceleration profile is obtained, and the acceleration development is plotted in Figure B-3(c). Next, multiple quintic polynomials are used to generate different trajectories between the different time intervals by using same formulation for quintic trajectories. In this manner, joint positions, velocities are plotted in Figure B-4.

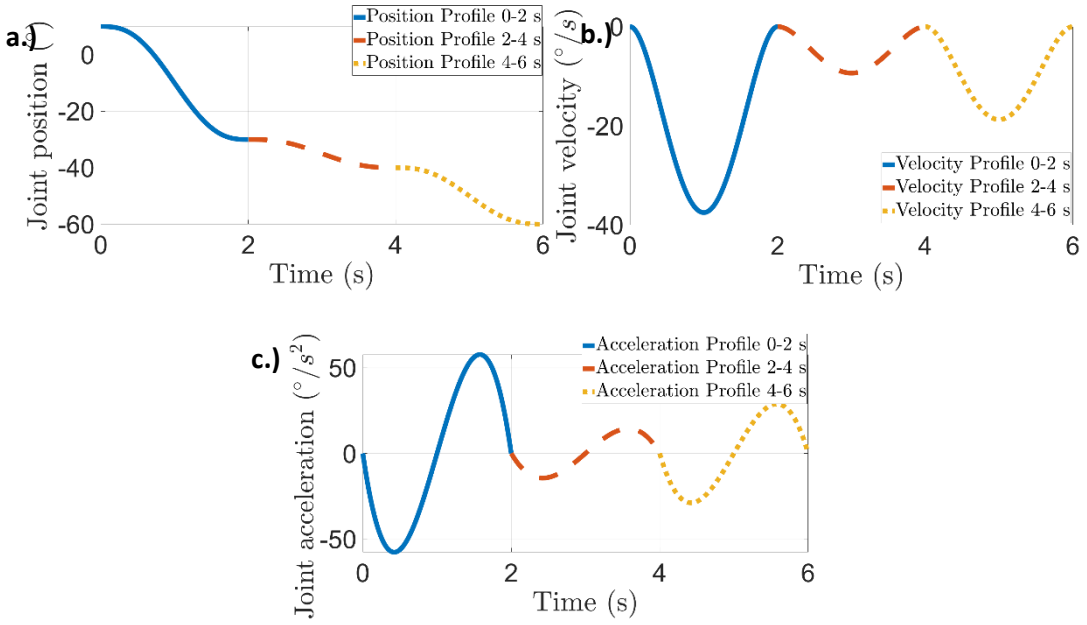

Figure B-4: (a) Joint position, (b)Joint velocity and (c) Joint acceleration variations in different time intervals for multiple quintic polynomial

In Figure B-4 (a), joint position is changed from the 10° to -30° in 0-2 second interval and position variation is set starting from the -30° and ending at -40° in 2-4 second interval, another position profile is created by changing the joint position from -40° to -60° in 4-6 second interval. The position profile variation is shown in Figure B-4(a). Then, velocities are set as zero in the starting and at the ending times for different time intervals. Velocity profile is obtained as derivative of the joint positions and it is plotted in Figure B-4(b). In first time interval, acceleration is started from zero which is given as initial condition and it reached -57.73°/s^2 at its peak to increase the velocity and deceleration with opposite acceleration started after 0.422 seconds and acceleration reached to 57.73°/s^2 its maximum at 1.578 seconds later. Then, it is reached to zero in the beginning of the second time interval as expected due to adjustments made based on initial and terminal conditions of input parameters as joint position, velocity and acceleration. In second time interval, acceleration changed from -14.43°/s^2 to 14.43°/s^2 in their peaks after 0.422 seconds and 1.578 seconds, respectively. In the third and last interval same acceleration profile is observed, and it is varied between -28.87°/s^2 to 28.87°/s^2, then it reached zero at the ending of the predetermined time as shown in Figure B-4.Single cubic, multiple cubic, single quintic and multiple quintic trajectories are generated based on equations (100)-(109), respectively. Generated trajectories are used to simulate joint torques in section 2.2.3.

Appendix C Derivations for Coriolis and Centrifugal terms

Derivation for the transformation matrices are presented to create mass matrix and Coriolis and centrifugal matrix. Based on transformation derivation, necessary equations are obtained to build matrix elements of the mass matrix. Then, U_{jkm} elements of the symbolic representation of the equations of the coriolis and centrifugal matrix. First, partial derivation is completed with respect to first joint which describes the interaction between first joint and subsequent joints, and it is given in the equation (110).

$$\begin{aligned} U_{111} &= \frac{\partial U_{11}}{\partial \theta_1} \\ U_{211} &= \frac{\partial U_{21}}{\partial \theta_1} \\ U_{311} &= \frac{\partial U_{31}}{\partial \theta_1} \\ U_{411} &= \frac{\partial U_{41}}{\partial \theta_1} \\ U_{511} &= \frac{\partial U_{51}}{\partial \theta_1} \\ U_{611} &= \frac{\partial U_{61}}{\partial \theta_1} \end{aligned} \tag{110}$$

Then, interactions for the second joint is given in the equation (111).

$$\begin{aligned} U_{212} &= \frac{\partial U_{21}}{\partial \theta_2}, U_{222} = \frac{\partial U_{22}}{\partial \theta_2} \\ U_{312} &= \frac{\partial U_{31}}{\partial \theta_2}, U_{322} = \frac{\partial U_{32}}{\partial \theta_2} \\ U_{412} &= \frac{\partial U_{41}}{\partial \theta_2}, U_{422} = \frac{\partial U_{42}}{\partial \theta_2} \\ U_{512} &= \frac{\partial U_{51}}{\partial \theta_2}, U_{522} = \frac{\partial U_{52}}{\partial \theta_2} \\ U_{612} &= \frac{\partial U_{61}}{\partial \theta_2}, U_{622} = \frac{\partial U_{62}}{\partial \theta_2} \end{aligned} \tag{111}$$

Next, interactions are represented for the third joint in terms of subsequent joints.

$$U_{313} = \frac{\partial U_{31}}{\partial \theta_3} \ , \ U_{323} = \frac{\partial U_{32}}{\partial \theta_3} \ , \ U_{333} = \frac{\partial U_{33}}{\partial \theta_3} U_{312} = \frac{\partial U_{31}}{\partial \theta_2} \ , U_{322} = \frac{\partial U_{32}}{\partial \theta_2}$$

$$U_{413} = \frac{\partial U_{41}}{\partial \theta_3} \ , U_{423} = \frac{\partial U_{42}}{\partial \theta_3} \ , U_{433} = \frac{\partial U_{43}}{\partial \theta_3} \quad U_{512} = \frac{\partial U_{51}}{\partial \theta_2} \ , U_{522} = \frac{\partial U_{52}}{\partial \theta_2} \tag{112}$$

$$U_{513} = \frac{\partial U_{51}}{\partial \theta_3} \ , U_{523} = \frac{\partial U_{52}}{\partial \theta_3} \ , U_{533} = \frac{\partial U_{53}}{\partial \theta_3}$$

$$U_{613} = \frac{\partial U_{61}}{\partial \theta_3} \ , U_{623} = \frac{\partial U_{62}}{\partial \theta_3} \ , U_{633} = \frac{\partial U_{63}}{\partial \theta_3}$$

After providing partial differential equations for the first three joints and with respect to first joint, second and the third one, equations are derived regarding to fourth joint. These representations are given in the equation (113).

$$U_{414} = \frac{\partial U_{41}}{\partial \theta_4} \ , U_{424} = \frac{\partial U_{42}}{\partial \theta_4} \ , U_{434} = \frac{\partial U_{43}}{\partial \theta_4} \ , U_{444} = \frac{\partial U_{44}}{\partial \theta_4}$$

$$U_{414} = \frac{\partial U_{41}}{\partial \theta_4} \ , U_{424} = \frac{\partial U_{42}}{\partial \theta_4} \ , U_{434} = \frac{\partial U_{43}}{\partial \theta_4} \ , U_{444} = \frac{\partial U_{44}}{\partial \theta_4} \tag{113}$$

$$U_{514} = \frac{\partial U_{51}}{\partial \theta_4} \ , U_{524} = \frac{\partial U_{52}}{\partial \theta_4} \ , U_{534} = \frac{\partial U_{53}}{\partial \theta_4} , U_{544} = \frac{\partial U_{54}}{\partial \theta_4}$$

$$U_{614} = \frac{\partial U_{61}}{\partial \theta_4} \ , U_{624} = \frac{\partial U_{62}}{\partial \theta_4} \ , U_{634} = \frac{\partial U_{63}}{\partial \theta_4} \ , U_{644} = \frac{\partial U_{64}}{\partial \theta_4}$$

Then, partial derivatives are taken with respect to fifth joint by considering subsequent joints. This symbolic representation is given in the equation (114).

$$U_{515} = \frac{\partial U_{51}}{\partial \theta_5} \ , U_{525} = \frac{\partial U_{52}}{\partial \theta_5} \ , U_{535} = \frac{\partial U_{53}}{\partial \theta_5} \ , U_{545} = \frac{\partial U_{54}}{\partial \theta_5} \ , U_{555} = \frac{\partial U_{55}}{\partial \theta_5} \tag{114}$$

$$U_{615} = \frac{\partial U_{61}}{\partial \theta_5} \ , U_{625} = \frac{\partial U_{62}}{\partial \theta_5} \ , U_{635} = \frac{\partial U_{63}}{\partial \theta_5} \ , U_{645} = \frac{\partial U_{64}}{\partial \theta_5} \ , U_{655} = \frac{\partial U_{65}}{\partial \theta_5}$$

Finally, derivatives are taken with respect to sixth joint regarding subsequent joints and it is given in the equation (115).

$$U_{616} = \frac{\partial U_{61}}{\partial \theta_6} \ , U_{626} = \frac{\partial U_{62}}{\partial \theta_6} \ , U_{636} = \frac{\partial U_{63}}{\partial \theta_6} \ , U_{646} = \frac{\partial U_{64}}{\partial \theta_6} \ , U_{656} = \frac{\partial U_{65}}{\partial \theta_6} , U_{666} = \frac{\partial U_{66}}{\partial \theta_6} \tag{115}$$

Necessary derivations are completed to find first multiplier of the coriolis and centrifugal terms in a form of matrix representation.

Appendix D Experimental Modal Analysis and CAD Data of The KUKA KR240 Robot

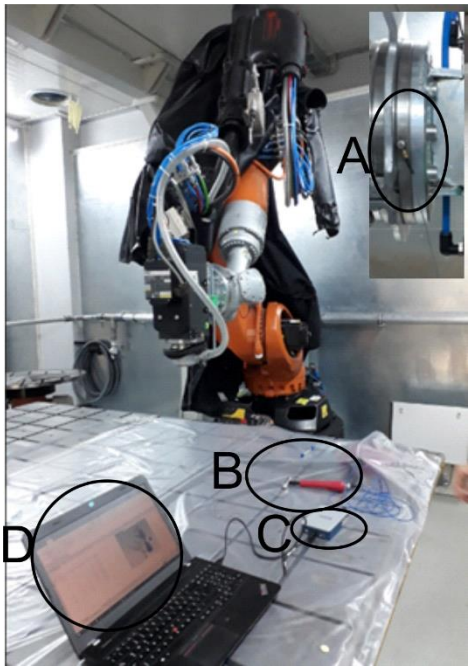

Figure D-1:Representative impact hammer test setup for robotic milling system A.) The uniaxial accelerometer B.) Modal Hammer C.) Data acquisition system D.) Computer and software

Impact hammer tests were performed on the KUKA KR 240 R2900. The Meggit 2302-50 impact hammer, Dytran 3035BG accelerometer, which is mounted on the end-effector, data acquisition system, and CutPro© simulation software were used in this experimental modal analysis test setup as shown in Figure D-1(B)-(A)-(C)-(D), respectively. The 11 measurement points were selected on the robot structure as shown in Figure D-2.

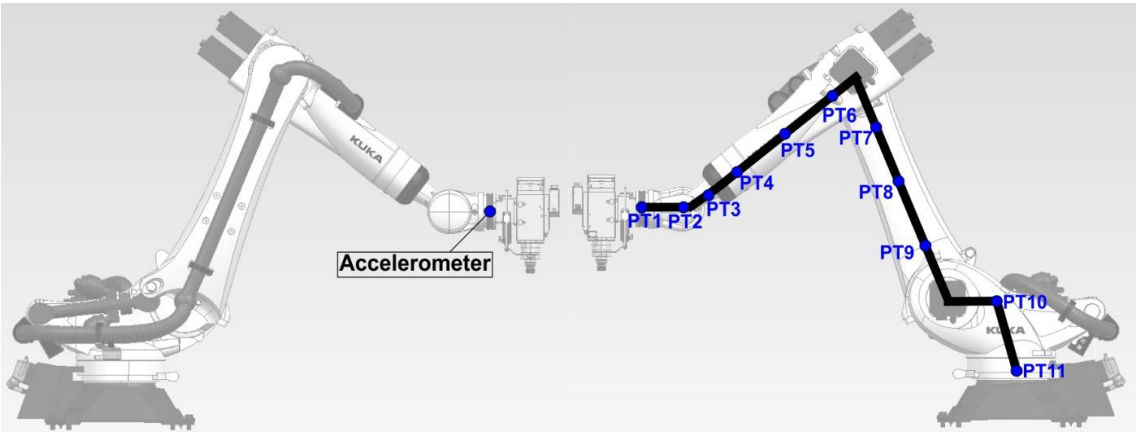

Figure D-2: FRF measurement points and accelerometer position representation

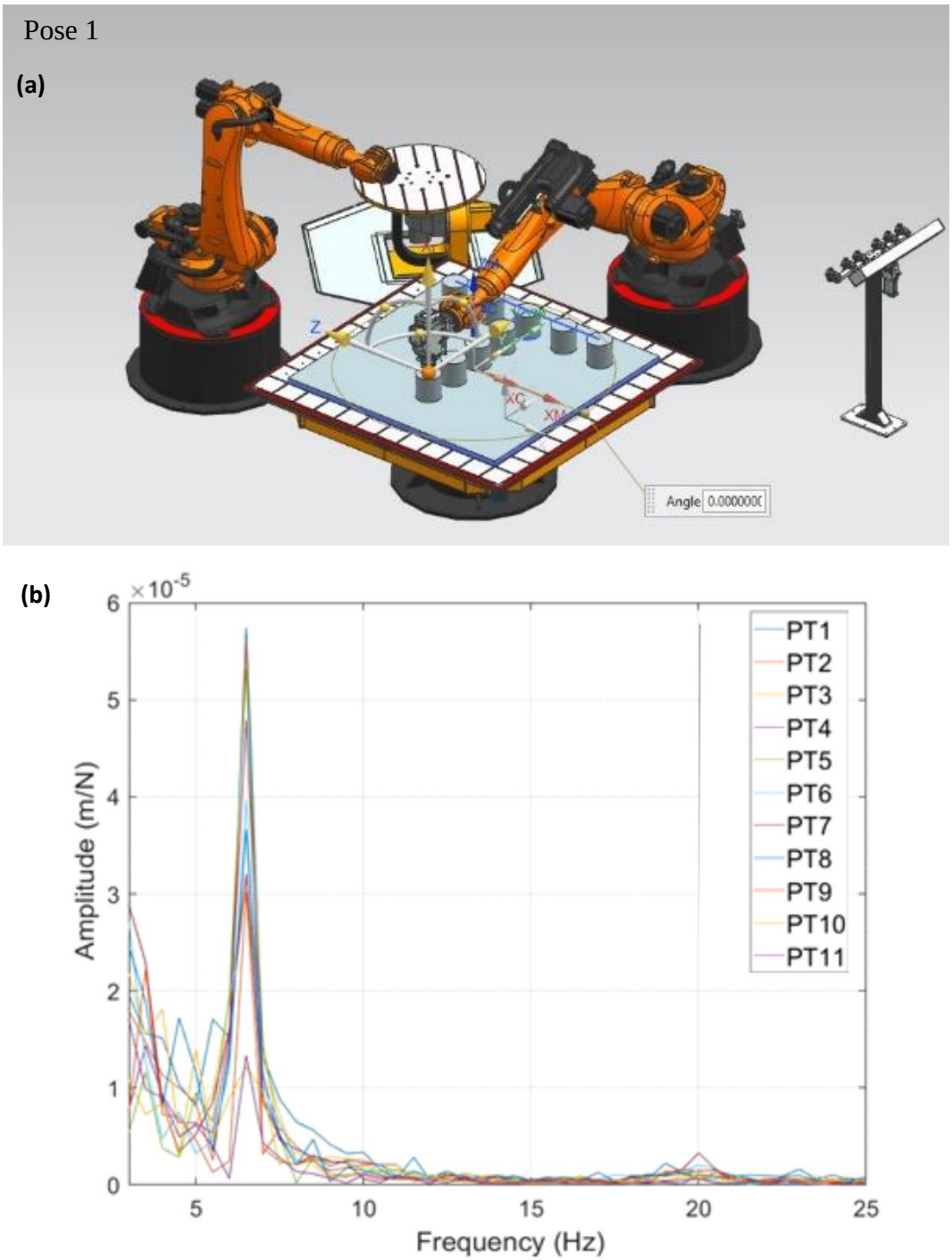

Figure D-3: (a) Pose 1 representation -NX© (b) Results of the impact hammer tests

Resonant Frequency (Hz)	Points
6.5	PT1-…-PT11
Resonant Frequency (Hz)	Points
11.5	PT1-…-PT11

Table D-1: Experimental natural frequencies of pose 1 (hammer impact test results)

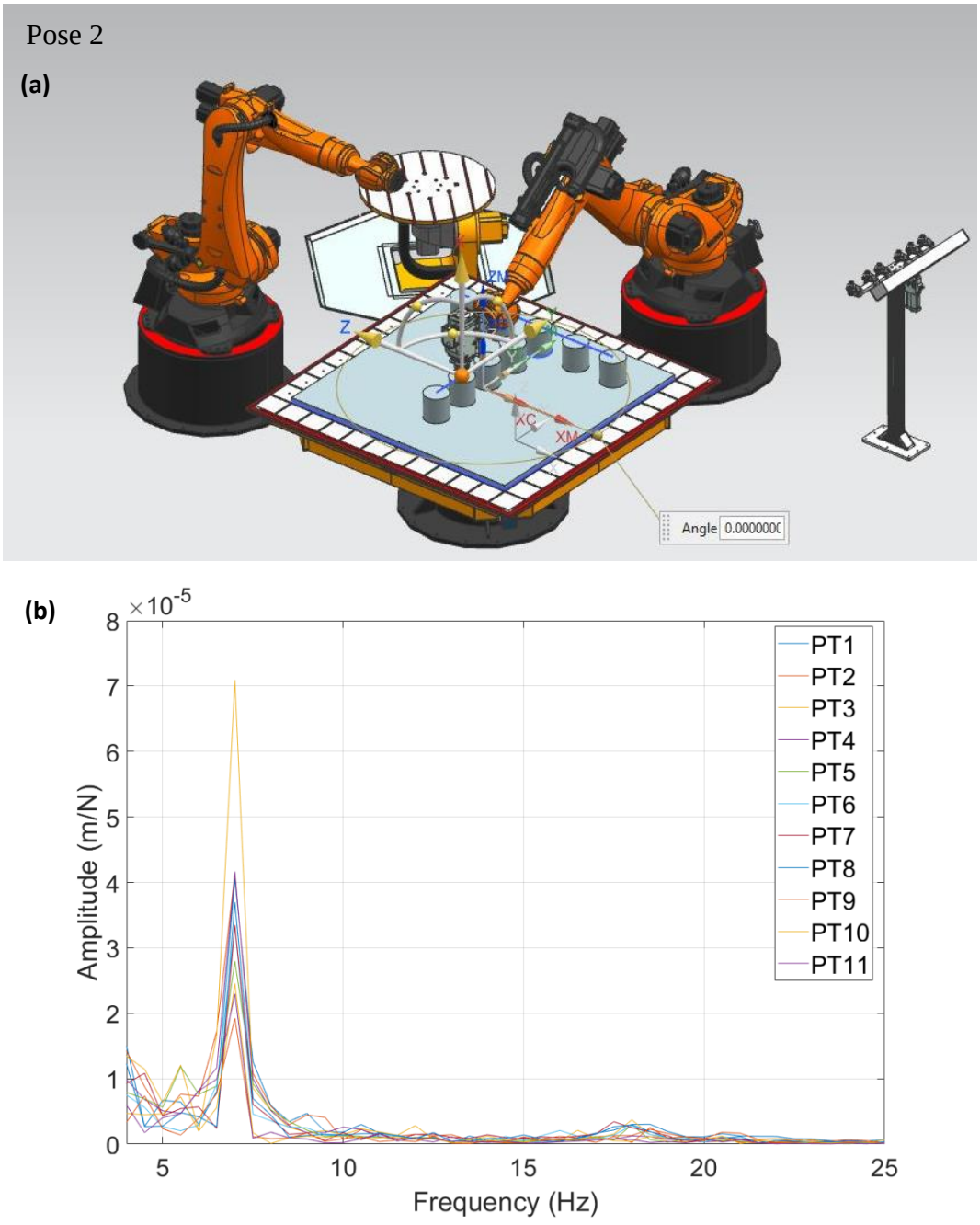

Figure D-4: (a) Pose 2 representation -NX© (b) Results of the impact hammer tests

Resonant Frequency (Hz)	Points
7	PT1-…-PT11
Resonant Frequency (Hz)	Points
18	PT1-…-PT11

Table D-2: Experimental natural frequencies of pose 2 (hammer impact test results)

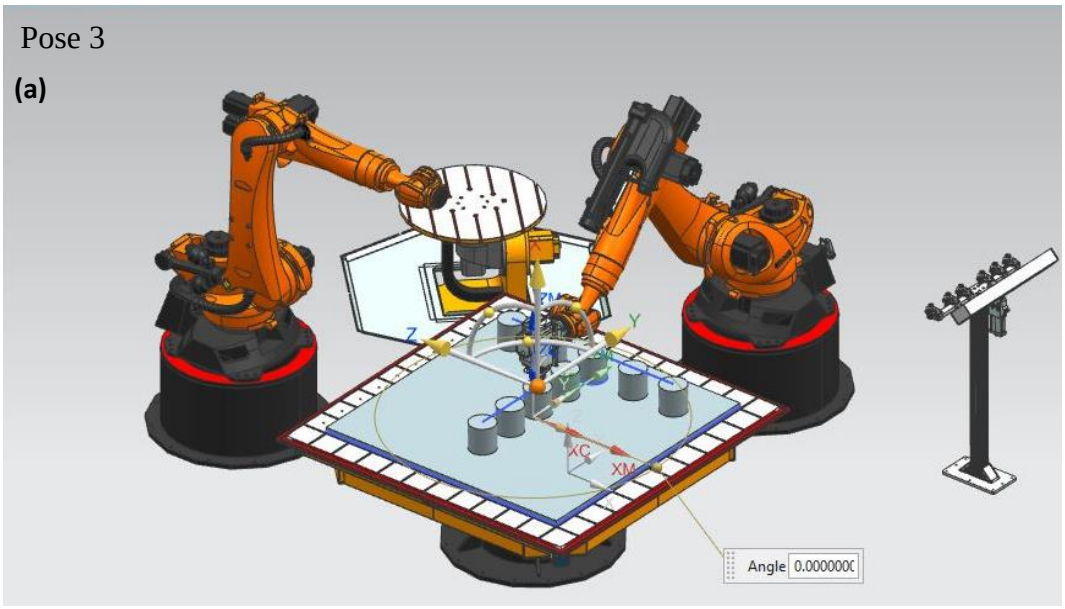

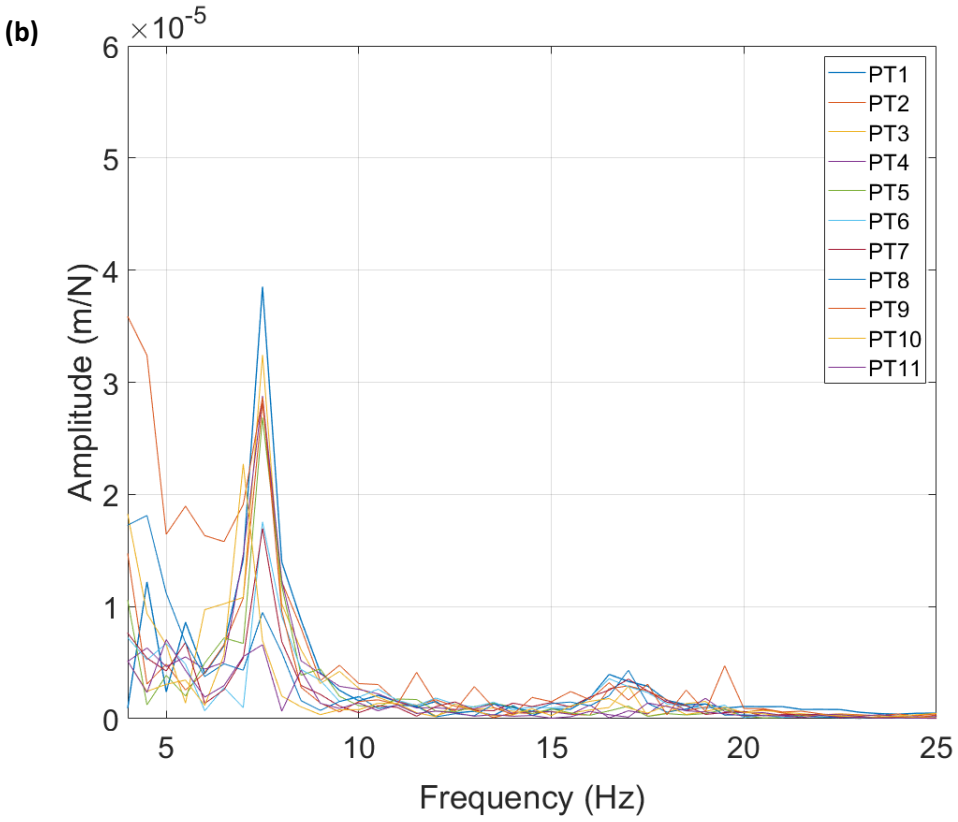

Figure D-5: (a) Pose 3 representation -NX© (b) Results of the impact hammer tests

Resonant Frequency (Hz)	Points
7.5	PT1-…-PT11
Resonant Frequency (Hz)	Points
17	PT1-…-PT11

Table D-3: Experimental natural frequencies of pose 3 (hammer impact test results)

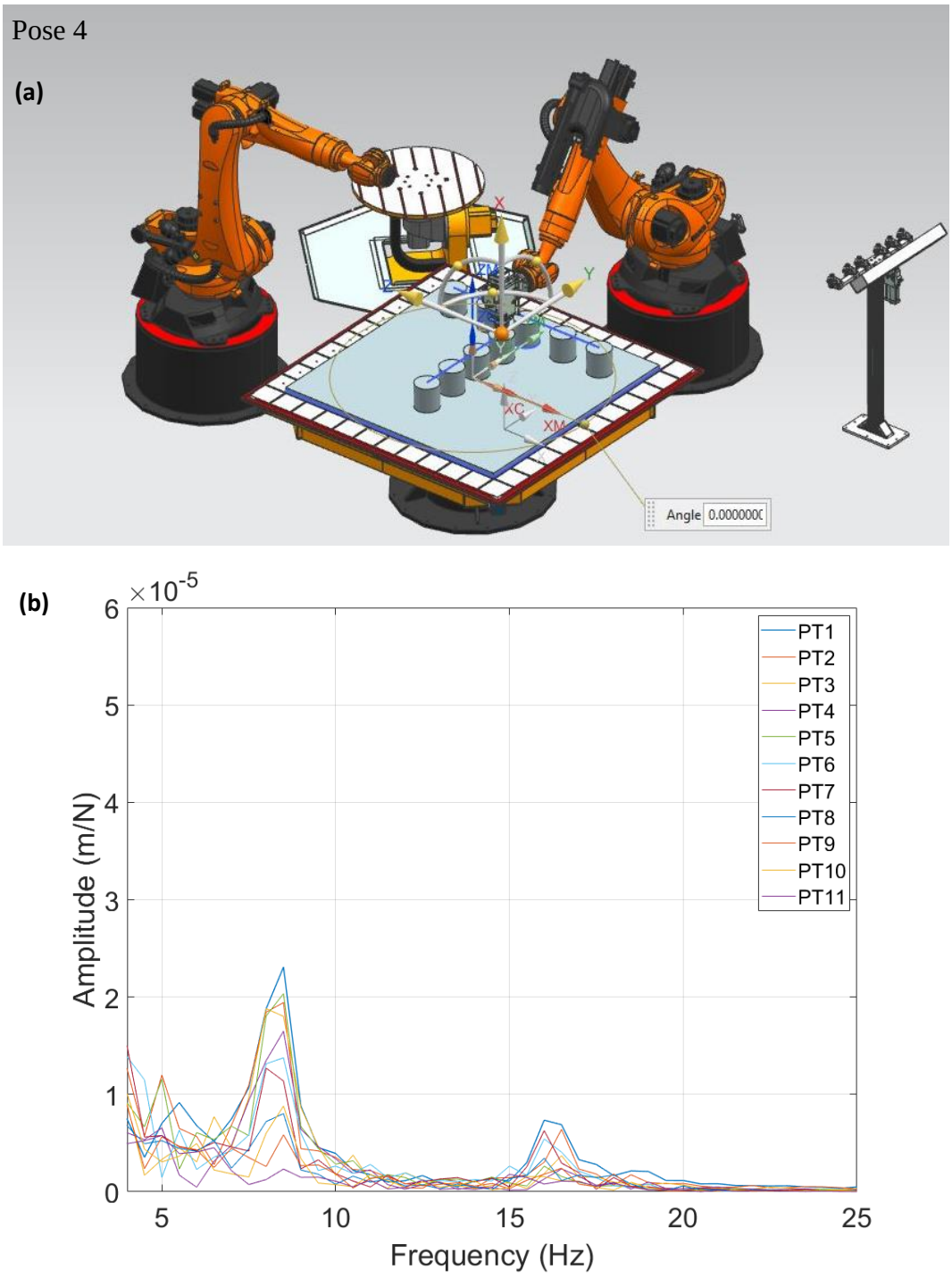

Figure D-6: (a) Pose 4 representation -NX© (b) Results of the impact hammer tests

Resonant Frequency (Hz)	Points
8.5	PT1-…-PT11
Resonant Frequency (Hz)	Points
16	PT1-…-PT11

Table D-4: Experimental natural frequencies of pose 4 (hammer impact test results)

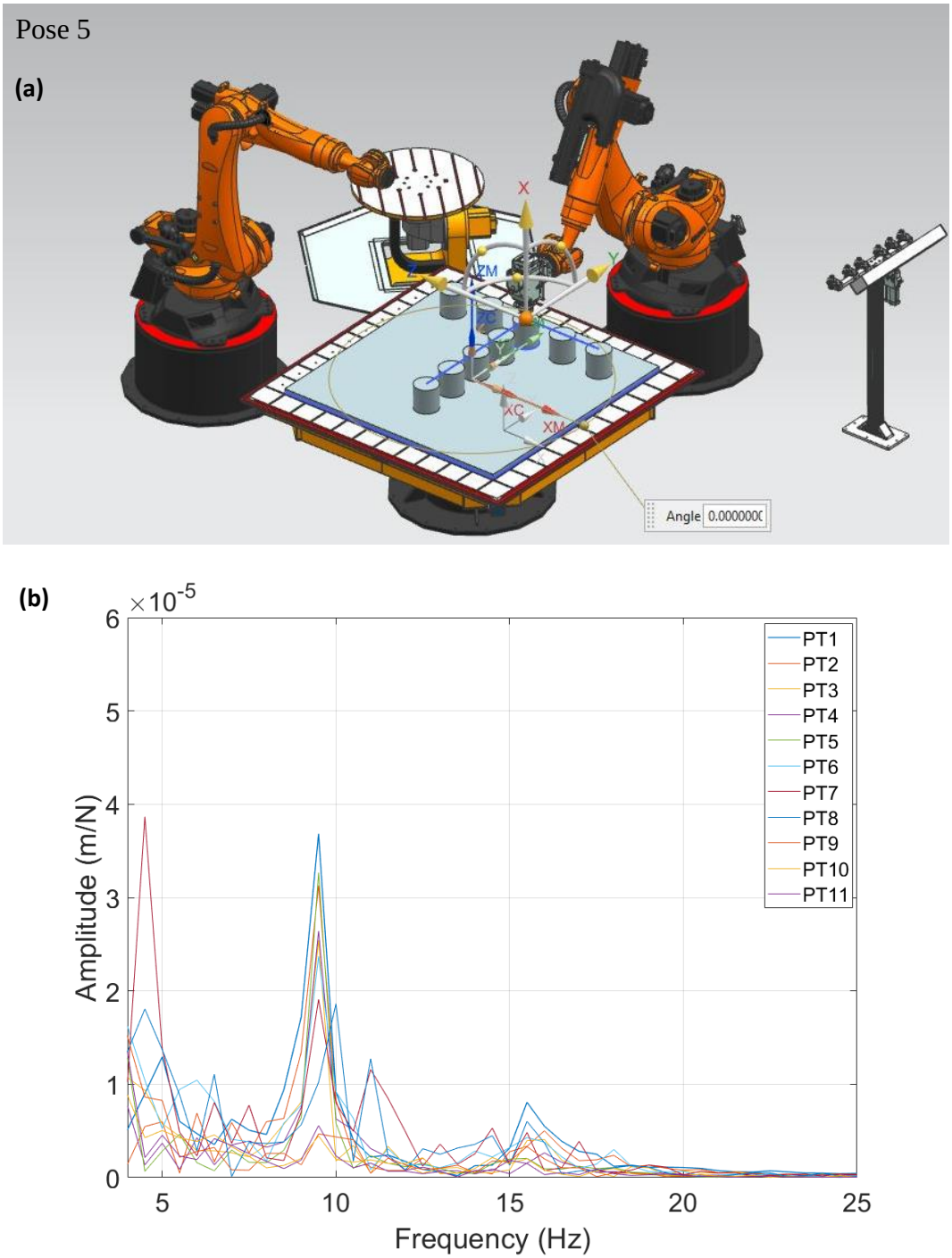

Figure D-7: (a) Pose 5 representation -NX© (b) Results of the impact hammer tests

Resonant Frequency (Hz)	Points
9.5	PT1-…-PT11
Resonant Frequency (Hz)	Points
15.5	PT1-…-PT11

Table D-5 :Experimental natural frequencies of pose 5 (hammer impact test results)

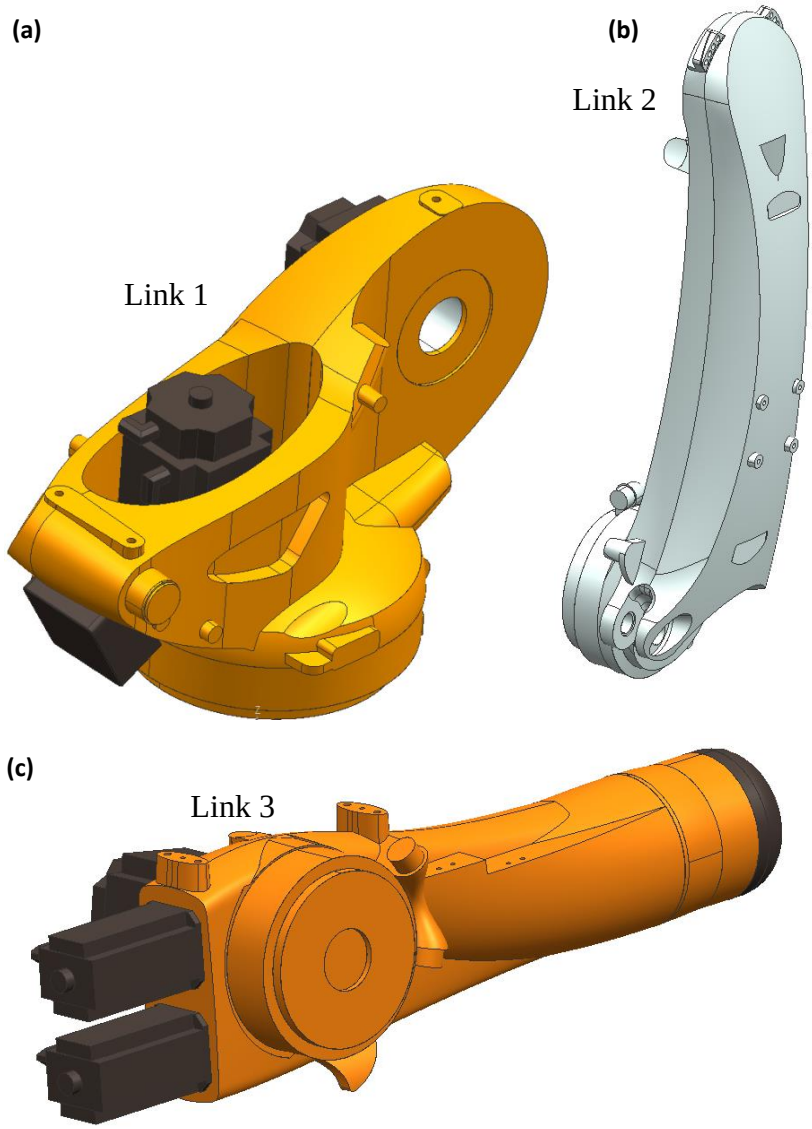

Figure D-8: Link representation and dynamic parameters from CAD data -NX© (a) Link 1, (b) Link 2, (c) Link 3

# Link numbers	1	2	3
Mass - kg	202	305	169
Center of mass (x)- mm	-365	6	-14
Center of mass(y) – mm	220	-525	-22
Center of mass (z) - mm	-11	-247	311
Inertia (Ixx) - kg.mm^2	6924809	5579409	19765236
Inertia (Iyy) - kg.mm^2	10712247	65582038	20163022
Inertia (Izz) - kg.mm^2	12703488	64902904	1818973
Inertia (Ixy) - kg.mm^2	-298740	93007	90651
Inertia (Ixz) - kg.mm^2	816535	6072031	613829
Inertia (Iyz) - kg.mm^2	-245506	33398	854718

Table D-6: Mass, center of mass and inertia properties of the links

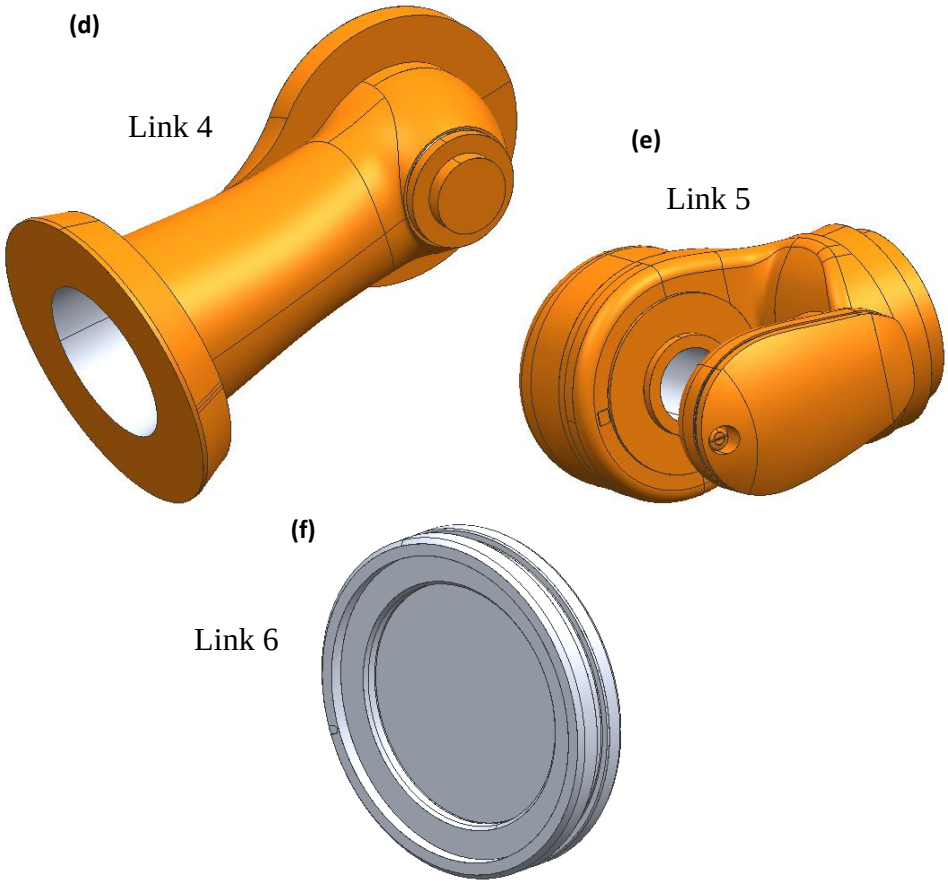

Figure D-9: Link representation and dynamic parameters from CAD data -NX© (a) Link 4, (b) Link 5, (c) Link 6

# Link numbers	4	5	6
Mass - kg	9	31	1.7
Center of mass (x)- mm	0	0	0
Center of mass(y) – mm	123	38	0
Center of mass (z) - mm	1.35	54.31	-13.8
Inertia (Ixx) - kg.mm^2	99987	477019	5331
Inertia (Iyy) - kg.mm^2	23164	321957	5337
Inertia (Izz) - kg.mm^2	101297	324135	10424
Inertia (Ixy) - kg.mm^2	0	39.2	0
Inertia (Ixz) - kg.mm^2	0	51	0
Inertia (Iyz) - kg.mm^2	-2175	-73587	0

Table D-7:Mass, center of mass and inertia properties of the links

Dynamics parameters are taken from the CAD data with respect to the assigned coordinate frames by D-H convention.